Kap-Centric Control of Nuclear Pores Based on Promiscuous Binding to FG Nucleoporins

Inauguraldissertation
zur
Erlangung der Würde eines Doktors der Philosophie
vorgelegt der
Philosophisch-Naturwissenschaftlichen Fakultät
der Universität Basel

von

Raphael S. Wagner

aus Reigoldswil (Basel-Land)

Basel, 2016

Genehmigt von der Philosophisch-Naturwissenschaftlichen Fakultät

auf Antrag von

Prof. Dr. Roderick Y. H. Lim

Prof. Dr. Birthe Fahrenkrog

Basel, den 09.12.2014

Prof. Dr. Jörg Schibler

Dekan

Abstract

Kap-Centric Control of Nuclear Pores Based on Promiscuous Binding to FG Nucleoporins

by Raphael S. WAGNER

Nuclear pore complexes (NPCs) are remarkable molecular machines that perforate the nuclear envelope (NE) in eukaryotic cells and mediate the rapid bidirectional traffic of hundreds of proteins, ribonucleoproteins, and metabolites across the nuclear envelope. Their enormous structure is composed of multiple copies of 30 different proteins (Nups) that add up to 60 – 120 MDa of mass depending on the organism. Each NPC contains a 50 nm-diameter central channel through which only molecules smaller than ~40 kDa or ~5 nm in size can diffuse passively. The movement of larger molecules is impaired by a permeability barrier generated by ~200 partly intrinsically disordered phenylalanine-glycine (FG)-rich nucleoporins (FG Nups) that are tethered to the NPC transport channel surface. These FG Nups interact promiscuously with nuclear transport receptors (NTRs), such as karyopherins (Kaps; e.g. Kapβ1) or NTF2, that mediate rapid trafficking of cargoes.

Given that the number of FG repeats per FG Nup also varies from 5 to ~50, NTR-FG Nup binding involves highly multivalent interactions, which are generally known to impart a strong avidity that enhances stability and specificity. However, this is paradoxical in the context of the NPC, because the high submicromolar Kapβ1-FG domain binding affinities predict slow off rates (given a diffusion-limited on rate) that contradict the rapid (~5 ms) *in vivo* dwell time. As this implies, Kap-FG binding ought to be sufficiently strong to ensure selectivity but also weak enough to promote fast translocation through the NPC. Nonetheless, an explanation as to how promiscuous binding of FG Nups to NTRs is balanced against the mechanistic control of the FG domain barrier is still lacking.

The purpose of my work was to investigate FG Nup-NTR binding promiscuity and multivalency by measuring the interaction kinetics, binding affinity and *in situ* associated conformational changes in Nsp1p FG domains when binding NTF2 and Kapβ1, both separately and together. Experimentally, this was achieved by using a novel surface plasmon resonance technique to correlate *in situ* mechanistic changes (molecular occupancy and conformational changes) with FG Nup-NTR binding.

The obtained results show that surface-tethered Nsp1p FG domains form molecular brushes at physiological conditions. Kapβ1 binding provokes brush extension while partitioning into a fast and slow kinetic phase, where the latter may form an integral part of the FG domain barrier. In contrast, NTF2 binding to pristine Nsp1p layers induced collapse, but not under competing interactions from Kapβ1. Therefore, promiscuous binding of NTF2 to Kapβ1-preloaded Nsp1p attenuates NTF2 towards higher off rates and more transient interactions.

My work demonstrates that promiscuous binding of NTRs to FG Nups ought to influence nucleocytoplasmic transport. This depends on the concentration, size and binding strength of each NTR. Indeed, some form of hierarchy may exist between different NTRs such that their relative concentrations may impact NPC barrier function. This interpretation departs from the conventional view that the FG Nups alone form the NPC permeability barrier. Rather I conclude that concentrating NTRs in the NPC transport channel also contributes to generating crowding-based selective barrier function of the pore.

Contents

List of Figures

List of Tables

Chapter 1

Introduction

Eukaryotic cells are subdivided into functionally and spatially distinct compartments that provide specialized environments for different tasks. This compartmentalization is achieved by intracellular membrane systems. The double lipid bilayer of the nuclear envelope, comprising the inner nuclear membrane and the outer nuclear membrane, separates the nucleoplasm containing the genetic material from the cytoplasm. This segregates the site of transcription and ribosome biogenesis in the nucleus from the protein synthesis machinery in the cytoplasm. Thus, the NE protects the structural and compositional integrity of the genome, and regulates how genetic information is transmitted to the proteome. Further, it protects the nucleus from pathogens such as viruses which act to alter the genetic information. Accordingly, eukaryotic cells employ numerous transport pathways, that allow for a staggering number of molecules to be shuttled between the nucleus and the cytoplasm. After transcription, mature mRNA has to overcome the NE in order to be translated into proteins in the cytoplasm. At the same time, numerous transcription factors have to enter the nucleus to initiate and regulate RNA transcription of proteins.

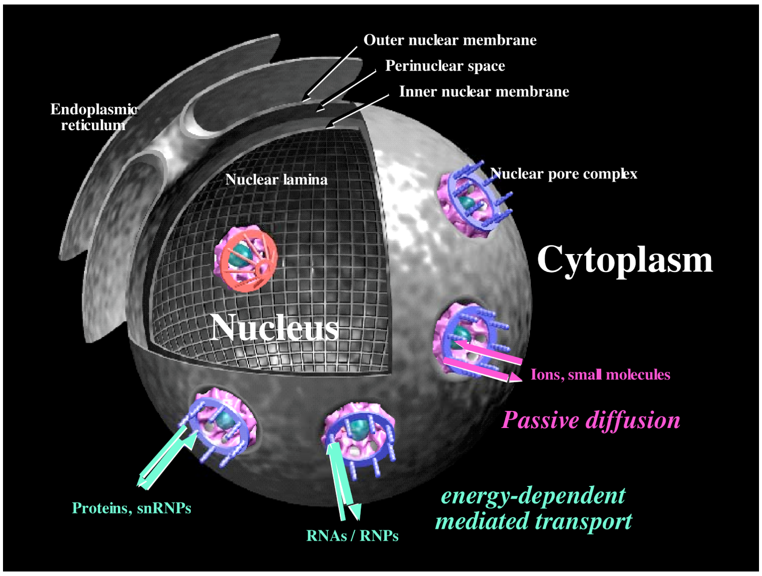

FIGURE 1.1: NPCs are huge molecular assemblies embedded in the NE of eukaryotes. They represent the sole gateway between the nucleus and cytoplasm and mediate all bidirectional traffic of molecules across the NE. Directed transport of molecules larger than ∼5 nm in size (e.g., ribonucleoporins; RNPs) require receptors while small molecules are able to cross the NPC by free diffusion. With permission from Daniel Stoffler and Ueli Aebi.

Bidirectional transport across the NE is mediated by huge multiprotein complexes embedded in aqueous pores that perforate the NE [1, 2]. These nuclear pore complexes (NPCs) constitute large transport channels and represent the sole gateways of macromolecular exchange (Figure 1.1).

The average pore density in vertebrates was shown to be 10 – 20 NPC/μm^2 (2000 – 5000 NPCs per nucleus) [3]. In the large nuclei of *Xenopus laevis* oocytes up to ∼50 NPC/μm^2 are found (∼5×10^7 NPCs per oocyte) [4]. Yeast cells appear to have an average pore density of ∼12 NPC/μm^2 (∼200 per nucleus) [5]. NPCs exhibit a number of remarkable properties. As a case in point, huge protein complexes up to ∼39 nm in diameter are able to cross the NPC with high efficiency while non-specific molecules are rejected from the pores [6, 7]. In fact, the number of proteins comprising the NPC represent only a fraction of all proteins that are translocated through the pore, which makes NPCs highly promiscuous. Moreover, multiple distinct protein complexes are ferried in parallel through the same pore at high rates of ∼1000 molecules per NPC per second [8–11]. In other words, NPCs act as transporters and molecular sorting machines at the same time. In order to overcome the NE, molecules which are larger than ∼5 nm in size need to exhibit specific interactions with the NPC [6]. Yet, rather counterintuitively, specific cargoes accumulate in their target compartments orders of magnitude faster than passively diffusing molecules, even at the same size [9, 12].

1.1 Structure and Function of the Nuclear Pore Complex

The NPC consists of approximately 30 different proteins [13], generally termed nucleoporins (Nups), which are broadly conserved among evolutionarily distant eukaryotes, i.e., from yeast to vertebrates and plants [13–16]. Each Nup appears in multiple copies of 8-, 16- or 32-fold in order to assemble into this multiprotein complex, resulting in a total of ∼500 – 1000 polypeptides forming a mature NPC [14]. These enormous molecular assemblies have molecular masses that range from ∼66 MDa in *Saccharomyces cerevisiae*, to ∼110 – 125 MDa in higher eukaryotes as observed for *Xenopus laevis* [2]. Using cryo-electron microscopy, the overall 3D architecture of NPCs from isolated Xenopus nuclei show linear dimensions of ∼120 nm outer diameter, ∼180 nm height [17] and ∼50 nm for the inner channel diameter. These dimensions closely resembles that of human NPCs as determined in human osteosarcoma U2OS cells [18]. *Dictyostelium discoideum* show a similar inner and outer diameter of ∼50 nm and ∼125 nm, but somewhat smaller height of ∼150 nm was measured [19, 20]. Although overall linear dimensions can vary, their overall architecture makes them probably the biggest molecular machines in the cell.

Nups can be classified into four different groups which represent the main building blocks of the pore (summarized in Figure 1.2):

1.) Transmembrane Nups: A set of three different membrane proteins, also known as "poms", build a membrane ring anchoring the NPC within the NE pore [21]. In addition, poms play a role in stabilizing the local curvature of the NE [22].

2.) Scaffold Nups: Defining roughly half of the total weight, scaffold proteins build the largest structural component of the NPC. Multiple copies of 13 different Nups form an interlaced structure shaping a symmetric core layer which stabilizes the NPC [21, 23]. This NPC core scaffold seems to be the main attachment site for central pore Nups [21].

3.) Cytoplasmic Filament Nups and Nuclear Basket: Located at the cytoplasmic side of the NPC, eight flexible filamentous structures extend from the outer ring by ∼35 – 50 nm [17, 19, 24]. These proteins are involved in specific interactions and can serve as docking sites for transport molecules [19, 25]. Cytoplasmic filaments are composed mainly of two Phenylalanin-Glycine rich nucleoporins (FG Nups), Nup42p (vertebrate Nlp1) and Nup159p (vertebrate Nup214) together with Nup82p. Yeast lack a homolog of the vertebrate Nup358, which is believed to give the cytoplasmic filaments more rigid structure in addition to its role in nucleocytoplasmic transport [26–28]. At the nuclear side of the NPC eight filamentous structures extend ∼50 – 100 nm nm into the nucleoplasm and finally merge into a distal ring, the nuclear basket comprising three FG Nups, Nup1p, Nup2p (vertebrate Nup50) and Nup60p (vertebrate Nup153) [20, 28–32].

4.) FG Barrier Nups: Attached to the core scaffold Nups, are multiple copies of FG Nups that collectively form a selective permeability barrier within the NPC transport channel. These barrier Nups represent a third of all nucleoporins and their inactivation impairs nuclear import [33]. In addition, their FG rich domains (FG domains) are intrinsically disordered [34–38], whereas small structured domains anchor FG Nups to the NPC scaffold [21].

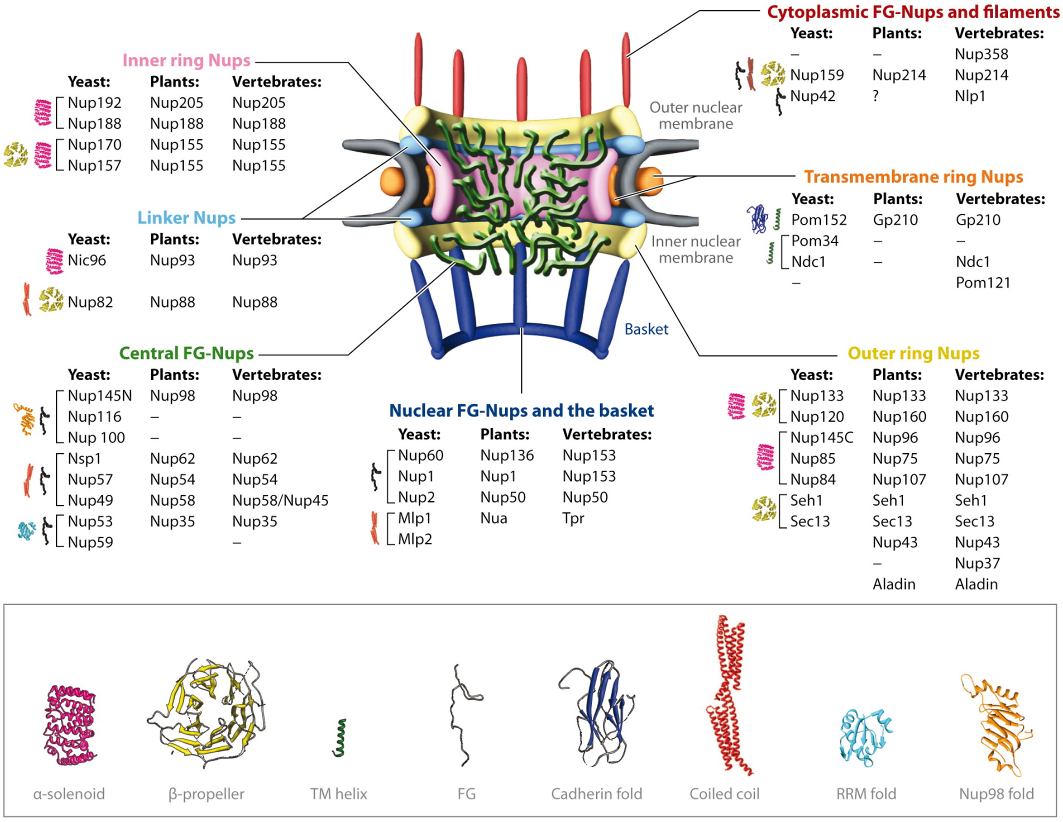

FIGURE 1.2: The structural components of the NPC. The symmetric core is composed of the outer ring Nups, the inner ring Nups and the linker Nups. Transmembrane ring Nups anchor the NPC framework in the NE. The NPC channel is filled with FG Nups which are flanked by asymmetric cytoplasmic and nuclear FG Nups which comprise the basket. The outer nuclear membrane and inner nuclear membrane are depicted in grey. The dominating protein folds of the proteins are described in the bottom [22]. Reproduced from Grossman, *et al.* [39].

1.2 Nucleocytoplasmic Transport

Bidirectional transport of cargoes across the NE is achieved by soluble transport factors that are typically members of the karyopherin-β superfamily (Kaps) and are either called “importers” or “exporters” according to the cargoes they recognize. Currently, 19 different Kaps in vertebrate and 14 Kaps in yeast were identified [40] of which 11 of the vertebrate and 10 of the yeast Kaps mediate nuclear transport.

1.3 GTP-dependent Transport

An overview of GTP-dependent nucleocytoplasmic transport is shown in Figure 1.3 and explained in more detail below.

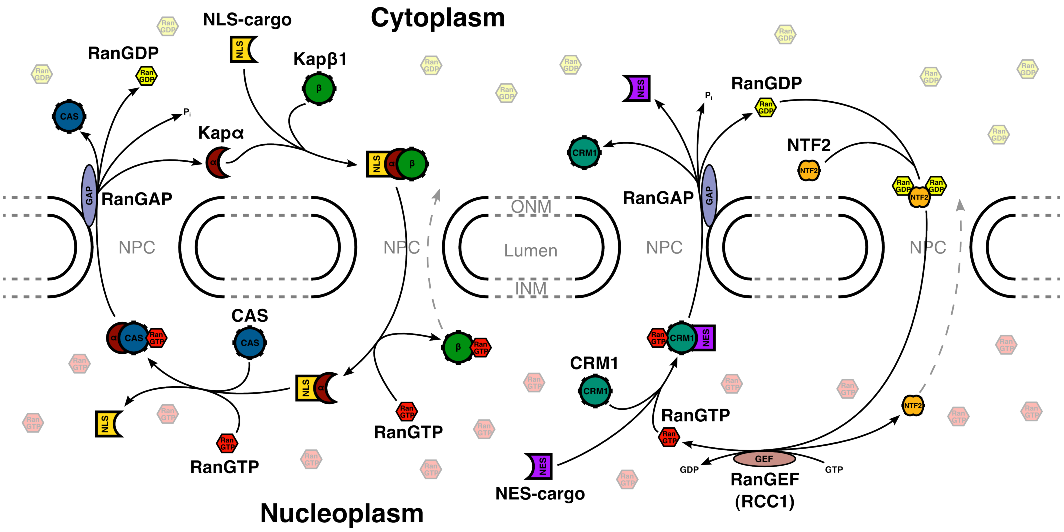

FIGURE 1.3: Overview of NCT and its dependency on GTP. Nuclear import of NLS-cargo is mediated by Kapβ1 via Kapα as adaptor protein. Upon assembly in the cytoplasm and subsequent translocation, cargo gets released in the nucleoplasm upon binding RanGTP. Kapα gets recycled by CAS in complex with RanGTP. Nuclear export of NES-cargo is mediated by CRM1 which is in its export competent state when in complex with RanGTP. Located at the cytoplasmic side, RanGAP catalyzed GTP hydrolysis which stimulates the disassembly of export complexes. RanGDP is recycled by the homodimer NTF2 and reloaded with GTP with the help of nuclear RanGEF which is bound to the chromatin. RanGTP is highly enriched in the nucleus whereas cytoplasmic Ran predominantly exists in its GDP bound form.

1.3.1 Import

One of the best characterized import pathway of NLS-cargo involves the heterodimeric complex karyopherinα/β (Kapα/β) consisting of Kapβ1 (Kap95p in yeast) and adapter protein Kapα (Kap60p in yeast). Kapα/β1 binds NLS-cargo via Kapα with nanomolar affinity while Kapβ1 binds the N-terminal importin-β (Kapβ) binding domain (IBB) of Kapα [41]. The NLS-cargo-Kapα-Kapβ1 import complex interacts with FG Nups via Kapβ1 [42] during translocation through the pore. Nuclear RanGTP (Ras-related nuclear protein, Gsp1p in yeast), a member of the RAS superfamily, binds to Kapβ1 and triggers the release of the NLS-cargo-Kapα complex into the nucleoplasm. Eventually, Kapβ1-RanGTP shuttles back to the cytoplasm, where GTP hydrolysis to GDP and subsequent dissociation of RanGDP frees Kapβ1 for another round of import. After Kapβ1 dissociation, the auto-inhibitory IBB domain weakens the affinity of Kapα towards NLS-cargo by competing with the NLS binding pocket. This results in a final release of NLS-cargo into the nucleus [31, 43, 44]. However, Kapα must be returned to the cytoplasmic side. CAS (cellular apoptosis susceptibility gene, Cse1p in yeast) was found to be the main mediator of Kapα export [45]. CAS affinity for Kapα is highly increased when in complex with RanGTP [45]. On the cytoplasmic side, hydrolysis of RanGTP catalized by RanGAP (Ran GTPase-activating protein) causes the Kapα-CAS-RanGTP complex to dissociate [27, 45, 46]. In addition to NLS, a different import signal (M9) promotes import of cargo by transportin (Kapβ2) which directly recognizes M9 without any adapter molecule, e.g. Kapα.

1.3.2 Export

Most of the nuclear export cargoes contain a nuclear export signal (NES). NES-cargoes are candidates for CRM1 (Xpo1p)-mediated export. Together with RanGTP, a stable NES-cargo-CRM1-RanGTP export complex forms which is able to translocate through NPCs [47]. NES-cargo gets released into the cytoplasm upon RanGAP mediated hydrolysis of RanGTP.

1.3.3 RanGDP/GTP Recycling

As there are no motors in the NPC, transport of specific molecules through the pore does not consume energy beyond $k_B T$ [48]. Thus, movement of molecules in the NPC is driven by Brownian motion which is non-directional. However, transport of cargo across the NE and its dissociation against a concentration gradient generally consumes RanGTP [49]. Release of cargo in the nucleus is driven by the free energy of RanGTP binding ($\Delta G \approx$ -51 kJ mol^{-1}). On the cytoplasmic side, the export complex must be disassembled which requires the hydrolysis of RanGTP ($\Delta G \approx$ -33 kJ mol^{-1}) catalysed by RanGAP [50]. This step is the only functionally irreversible process in the transport cycle. After hydrolysis of GTP in the cytoplasm, homodimeric NTF2 imports RanGDP back into the nucleus [51] where chromatin bound RanGEF (guanine exchange factor for Ran GTPase, RCC1) stimulates Ran to exchange GDP with free GTP. This finally replenishes the pool of RanGTP in the nucleus. Spatially separated RanGAP and RanGEF both increase the GTPase and nucleotide exchange activity by about 5×10^5-fold [50, 52]. This leads to a steep gradient of RanGTP across the NE and therefore implies directionality of nucleocytoplasmic transport.

1.4 FG Nups are Intrinsically Disordered Proteins

Approximately 40% of all eukaryotic proteins are predicted to have at least one long (>50 residues) disordered region and ~10% of proteins show a high propensity of being fully disordered [53]. When compared with ordered proteins, intrinsically disordered proteins (IDPs) are significantly depleted of order-promoting amino acids (i.e., Ile, Leu, Val, Trp, Tyr, Phe, Cys, Asn) and show substantial enrichment in disorder-promoting amino acids (i.e., Ala, Arg, Gly, Gln, Ser, Glu, Lys, Pro) [54]. Further, they combine low mean hydrophobicity with high net charge, which promotes disorder in proteins [55].

IDPs exhibit a number of exceptional functional advantages which allows them to interact with other proteins in a manner not achievable by ordered proteins [56, 57]. A key advantage is the combination of high specificity with low affinity in IDP-protein interactions. This is a useful property for reversible signal transduction which favours rapid association and dissociation of the partner without high binding strength [54]. Compared with ordered proteins interacting in the same affinity range, IDPs show enhanced association rates due to their flexibility which allows the encounter complex to evolve into the bound state faster than ordered proteins [58]. Given a diffusion limited association rate, a decrease in the dissociation rate generally increases the affinity. This is unfavourable for interactions which demand for high specificity but rapid dissociation at the same time. Intrinsic disorder provides a solution to this conflict. While ordered proteins have to break all interactions simultaneously for completed dissociation, IDPs can dissociate from their target in a stepwise manner. The resulting smaller energy barriers lead to much greater dissociation rates [58, 59]. In addition, the high flexibility of IDPs also enables them to bind multiple different partners by changing their conformation [59].

The ability to specifically bind different partners is commonly referred to as promiscuity (alternately referred to as multispecificity and in immunological literature as cross-reactivity or degeneracy [60]). Promiscuity is advantageous in signaling and regulation and could explain the high fraction of intrinsic disordered conformations involved in the "hubs" of protein-protein interaction networks. These central hub-proteins bind to a high number of different partners, often in a “one-to-many” and “many-to-one” fashion [61].

FG Nup	FG domain	FG Nup relative abundance	Number of FG repeats	Repeat motif(s)
Nup159p	(454 – 855)	8	25	**FG**, FxFG
Nup116p	(1 – 696)	8 – 32	47	**FG**, GLFG
Nup42p	(1 – 374)	8	30	**FG**, FxFG
Nup100p	(1 – 884)	8 – 32	46	**FG**, GLFG
Nup59p	(1 – 206)	32	4	FG
Nup49p	(1 – 417)	16	19	**FG**, GLFG, FxFG
Nsp1p	(3 – 601)	32	35	**FxFG**, FG
Nup53p	(41 – 267)	32	4	FG
Nup57p	(1 – 365)	16, 32 – 48 [62]	20	**GLFG**, **FG**, FxFG
Nup145p	(1 – 367)	16 – 32	13	**GLFG**, FxFG, FG
Nup60p	(387 – 521)	8	1	FxFG
Nup1p	(325 – 1049)	8	19	**FxFG**, FG
Nup2p	(206 – 562)	8, 32 [62]	11	**FxFG**

TABLE 1.1: Relative abundance, FG domain size and number of repeat motifs of yeast FG Nups. If not stated otherwise, all values are from Peleg, *et al.* [63]. A complete list can be found in Cronshaw, *et al.* [14]. In the case of multiple FG motifs, the most abundant is marked in bold.

One third of Nups contain repeating linear FG motifs (i.e., FxFG, GLFG, FG; see Section 1.1). First described in yeast NPCs [64–66], FG Nups were soon identified to hold a key role in the NPC gating mechanism. Inactivation of FG Nups by RNA interference directly impaired nuclear transport function in *Drosophila melanogaster*, demonstrating the selective requirement for FG Nups [33]. Further, the shared ability to directly interact with ∼15 (∼20 in humans) distinct nuclear transport factors (e.g., Kaps, NTF2) emphasizes FG Nups essential function as promiscuous "hubs" in nucleocytoplasmic transport [42, 62, 67–70].

FG Nups contain 150 – 700 amino acid long domains which exhibit intrinsic disorder at physiological conditions [34–36, 71]. In total, 13 different yeast (11 in vertebrates) FG Nups are known to line the central channel [39, 63] (listed in Table 1.1). They exist in multiple copies of 8, 16 and 32 [14, 62] and are either symmetrically distributed or biased to the nuclear or cytoplasmic side of the NPC [21] (Figure 1.4). Therefore, a total number of ∼200 FG Nup molecules is estimated to populate the NPC central channel [22]. Together, they contribute about 3500 FG repeats per NPC [72] which provide the promiscuity needed to interact with multiple distinct transport factors (e.g. CRM1, CAS, Kapβ1 or NTF2) [73].

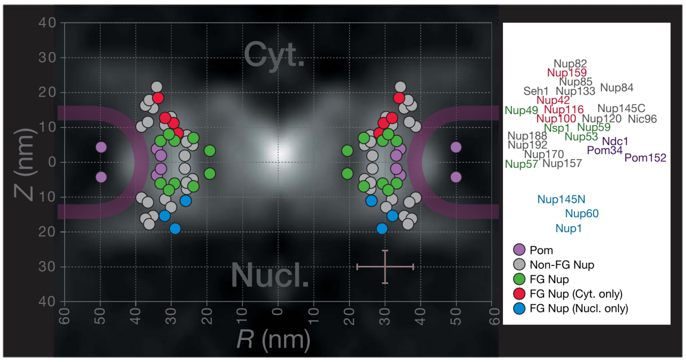

FIGURE 1.4: Localization of Nups in the NPC estimated by immunogold electron microscopy. The relative position of the C-terminus of each protein is superimposed on the cryo-EM obtained protein density map of a cross-section of the yeast NPC. The coordinate system with 10 nm intervals has its origin in the center of the transport channel (central Z-axis (R) and equatorial plane (Z)). Brown bars indicate average allowed position ranges (± 8 nm and ± 4.5 nm). Reproduced from Alber, *et al.* [74].

1.5 Multivalency in Nucleocytoplasmic Transport

Karyopherins in yeast and humans share similar molecular weights (90 – 150 kDa) and they all have their isoelectric point (pI) between 4 and 5. In spite of their low sequence identity of only 10 – 20%, they all contain tandem series of helical HEAT repeats [75, 76]. Extensive structural studies and simulations revealed up to 10 different binding pockets on Kapβ1 that recognize FG repeats [77] (Section 1.5.1). Although completely different in structure, up to 6 FG binding spots were determined on NTF2 by NMR and computational studies [78–80] (Section 1.5.2). Therefore, multivalency likely plays an important role in nucleocytoplasmic transport.

In general, interactions between an m-valent receptor and an n-valent ligand is considered to be multivalent if the number of binding sites of both m and n are larger than one [81]. Otherwise the interaction is typically monovalent in nature. The most notable feature of a multivalent interaction is that the collective binding affinity, also known as avidity, could be collectively much stronger than its monovalent counterparts [82]. This is frequently used by nature to accomplish tight binding [82].

1.5.1 Kapβ1 Crystal Structure and Multivalent Interactions with FG Nups

Kapβ1 has an overall snail-shaped structure forming a flexible alpha-solenoid as shown in Figure 1.5A. The all-helical snail-shaped transport factor forms a flexible alpha-solenoid composed of 19 HEAT repeats. Each repeat consists of two helices which are located anti-parallel to each other and are connected by short turn residues, and as such are comprising the concave inner and the convex outer surface of the molecule. Kapβ1 binds the IBB domain of Kapα in the inner groove while potential binding sites for FG repeats are exposed throughout the solvent accessible surface from the N-terminal HEAT repeat 3 to the C-terminal HEAT repeat 17. Figure 1.5B shows the structure of an N-terminal Kapβ1 fragment in complex with two FSFG peptides. Figure 1.6 lists FG binding sites as predicted by simulations (MD) or sequence alignment. Seven of these binding sites are experimentally confirmed [42, 45, 69, 77, 83–85]. Altogether, 10 different potential binding pockets for FG repeats were determined on the outer surface of Kapβ1. This demonstrates the potential for multivalent interactions with FG Nups inside the NPC. As predicted, only a small number of 4 residues is needed to form a FG repeat specific binding site [77]. Anticipated for the multivalent binding nature of Kapβ1, high affinities towards FG Nups were classically determined to be in the range of KD $\sim 1-200$nM [83, 86]. Mutations in HEAT repeats 5 – 7 significantly reduced the interaction by more than 5 fold and thus verifies the affinity-enhancing effect of multivalency [83].

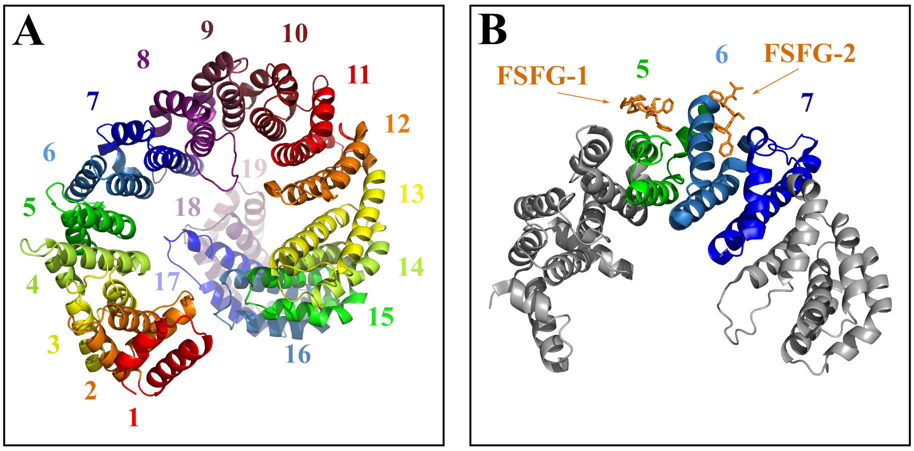

FIGURE 1.5: **(A)** Crystal structure of Kapβ1 bound to the IBB domain of Kapα (not shown; PDB code: 1QGK). The structural hallmark of Kapβ1 are the 19 HEAT repeats denoted with numbers starting at the N-terminus. Structure and HEAT repeat definition are adapted from Cingolani *et al.* [41]. **(B)** Crystal structure of a N-terminal Kapβ1 fragment (residues 1-442) in complex with Nsp1p-5FF (residues 497-608; PDB code: 1F59). Bound FSFG repeats are shown between HEAT repeat 5 & 6 (FSFG-1) and 6 & 7 (FSFG-2) as determined by Bayliss *et al.* [42].

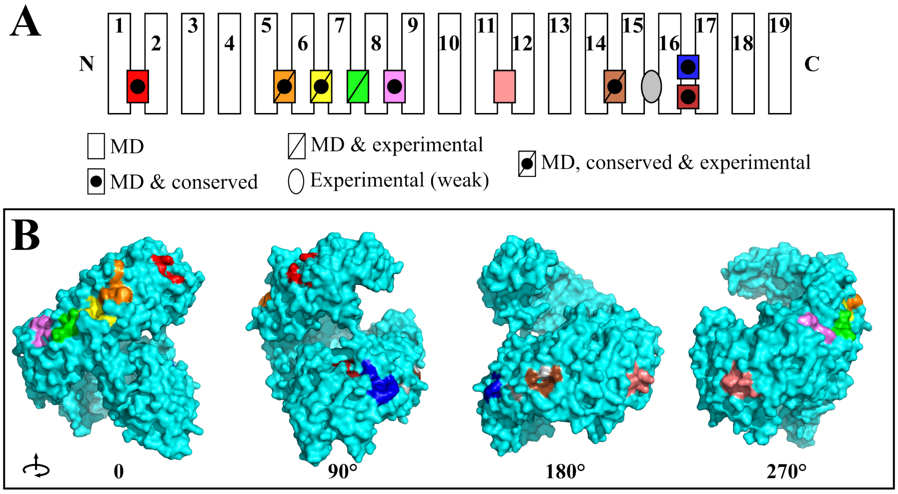

FIGURE 1.6: Multiple computed and experimentally determined FG repeat binding sites of Kapβ1. **(A)** 10 different binding spots are distributed along HEAT repeat 1 – 19. **(B)** Localization of the FG repeat binding sites 1 – 10 in the context of the whole molecule (PDB code: 1QGK)[41]. Binding spots which were determined by MD are labeled with a rectangular. Conserved binding spots are depicted with a black dot, while experimentally known binding sites are marked with a black slash. Only weak experimental confirmation exists for the binding spot labeled with an oval between HEAT repeat 15 & 16.

1.5.2 NTF2 Crystal Structure and Multivalent Interactions with FG Nups

Although the molecular mass predicted from its sequence is 14 kDa, NTF2 has been reported to have an apparent mass of 28 kDa in solution, consistent with its existence as a homodimer at physiological concentrations [87–90]. The individual polypeptide chains form an α- and β-barrel where the bent β-sheet is backed by one longer and two shorter α-helices. The two flat faces of the β-sheet form a extensive contact zone between two individual monomers (Figure 1.7A) [91]. The C-terminus together with the hydrophobic residues in the upper portion of NTF2 allows the binding of two RanGDP molecules simultaneously [92].

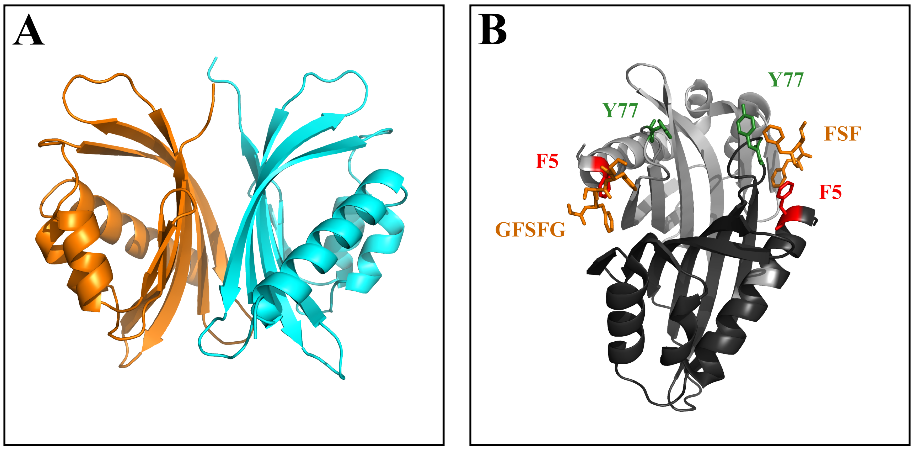

FIGURE 1.7: Crystal structure of homodimeric rat NTF2 and yeast NTF2 N77Y mutant in complex with FSFG repeat peptides. **(A)** NTF2 primarily forms a homodimer in solution. The crystal structure of the individual chains are shown in different colors (PDB code: 1OUN) [93]. The interface is built by the two joining β-sheets. **(B)** Crystal structure of two FSFG repeats (orange) in complex with yeast NTF2 N77Y mutant (PDB code: 1GYB) [70]. The hydrophobic binding pockets are located around Phe5 (Trp7 in rat NTF2; labeled in red).

Centered around Trp7 in rat NTF2 (Phe5 in yeast NTF2) a hydrophobic patch was identified that interacts with FG repeats [68, 94]. The importance of this residue in the interaction with FG Nups was demonstrated *in vitro* and *in vivo* using site-directed mutagenesis, protein-protein interaction studies and functional assays [9, 68, 94]. Structural studies of yeast NTF2 in complex with FSFG peptides confirmed two binding sites for FG repeats around Phe5 (Figure 1.7B). Interestingly, the hydrophobic patch includes residues from both chains and extends over the interface of the two monomers (“Binding spot #1” in Figure 1.8A). Including binding spot #1, up to 6 FG repeat binding pockets were determined experimentally or were predicted by simulation [79]. Listed in Figure 1.8B, binding spots #1,#2 and #4 confirm direct experimental evidence [70, 78, 80], whereas spot #3 was described by lower resolution experimental data [80]. Binding spots #5 and #6 have yet not been verified experimentally. Nevertheless, this indicates that NTF2 exerts multivalent interactions with FG Nups.

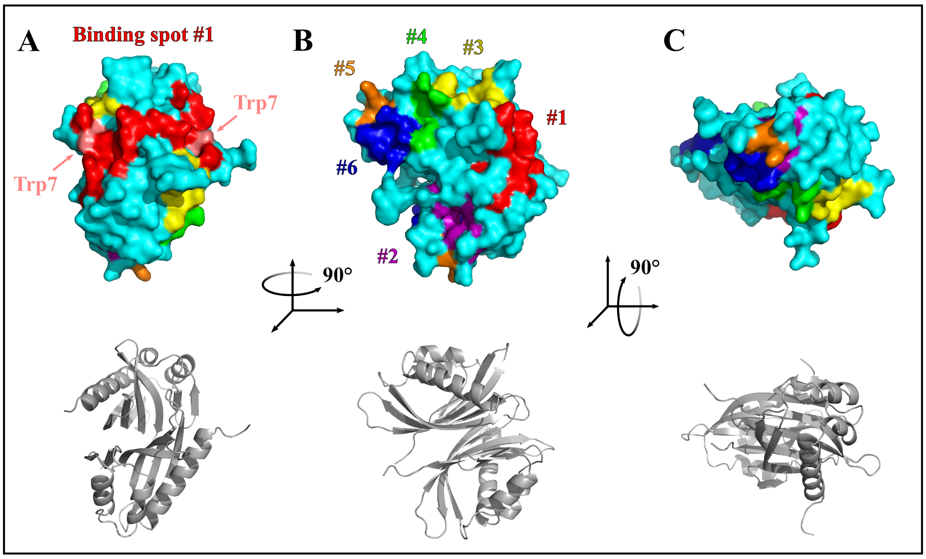

FIGURE 1.8: FG repeat binding spot positions on NTF2 as identified by simulation (MD) [79]. In the top row, a surface representation of the NTF2 dimer is shown with the corresponding cartoon of secondary structure below. **(A)** NTF2 dimer derived from rat NTF2 crystal structure (PDB code: 1OUN) [93]. Only the main binding spots around Trp7 involves residues from both monomers. **(B)** Binding spots #1 - #6 are each indicated on the view from (A) rotated 90° around the vertical axis. **(C)** The view from (B) rotated by 90° around the horizontal axis.

1.6 Transport Models

NPCs contain about 2500 – 3500 FG motifs within their transport channel that follows from the high abundance of FG domains which is estimated to be in the order of 10 mM [72, 95]. Still, transport efficiency through the pore is remarkably high. About 100 – 500 parallel translocation events per second add up to an estimated molecular flux of ~20 – 80 MDa·NPC^{-1}s^{-1} [9, 10, 96]. In other words, it takes a little more than 1 s to transport the equivalent mass of a single NPC through an NPC [9].

How such high transport rates are accomplished through a pore which is filled with FG domains remains a central question in the field. The challenge lies in understanding the precise mechanism of how the FG Nups overall conformation correlates with function which, to date, is still not fully understood.

This is because it remains a formidable problem to resolve FG Nup structure inside the pore. For instance, cryo-electron tomographic reconstructions fail to capture the FG Nups based on their high flexibility which causes low electron density readouts [20]. Based on *in vitro* studies of FG domain organization, several models exist which describe nuclear transport. Although they differ in details, they agree that FG Nups form a collective barrier that blocks translocation of inert molecules and can be overcome with the help of nuclear transport receptors (NTRs; e.g, Kapβ1) [8].

1.6.1 The Selective Phase Model

A "selective phase" consisting of a sieve-like meshwork of FG domains in the NPC was first proposed by Ribbeck, *et al.* [9]. The underlying mechanism is based on hydrophobic interactions between neighboring FG repeats. Subsequent work showed that mild apolar solvents (e.g., cyclohexane-1,3-diol) could cause a reversible collapse of the FG domain barrier in cells by perturbing inter-FG repeat interactions [97]. Indeed, Frey, *et al.* successfully showed macroscopic (up to a few millimeters in size) hydrogel formation of highly concentrated (∼1 – 100 mM) FG/FxFG (Nsp1p residues 2 – 601) , GLFG domains (Nup49p residues 1 – 246 and Nup57p residues 1 – 233) and mixtures thereof [98, 99]. Gelation was performed under non-physiological conditions by dissolving lyophilised FG domains (∼200 mg/ml) in 0.2% TFA [99]. Such FG domain hydrogels were shown to reproduce the permeability barrier of the NPC when fully saturated (i.e., every FG repeat is crosslinked) [99, 100].

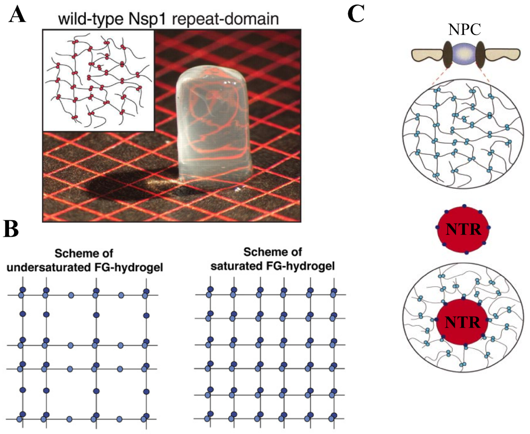

FIGURE 1.9: The selective phase model. **(A)** Macroscopic hydrogels form under non-physiological conditions at high FG domain concentration of ∼1 – 100 mM [98, 99, 101, 102]. **(B)** Untersaturated (left) and saturated (right) FG hydrogel. FG repeats are depicted in blue. **(C)** The selective phase model proposes that FG domains crosslink to form a three-dimensional meshwork within the NPC. Multivalent NTRs are thought to melt through the gel during translocation. **A** reproduced from Frey, *et al.* [98], **B** reproduced from Frey *et al.* [100] and **C** modified from Ribbeck, *et al.* [9].

The model predicts that each mesh in the gel (between 3 – 6 nm) defines the upper size of molecules which can freely diffuse through the meshwork [99, 100]. By binding FG repeats, Kaps are thought to locally open the FG-FG bonds [98] and thereby “dissolve” into the meshwork which otherwise poses a physical barrier to non-specific molecules (Figure 1.9) [9]. However, it remains less clear how such gels retain their functional properties at the nanoscopic environment in the NPC transport channel when compared to the non-physiological conditions used for their assembly *in vitro* [98]. FG domains which successfully formed hydrogels did not exhibit any interaction with itself or other FG domains under physiological conditions [38, 103]. In contrast to the selective phase model were Kap binding locally dissolves the meshwork, multivalent proteins are generally thought to stabilize the gel formation in such self-assembly processes [104]. Indeed, the presence of Kaps prevent hydrogel formation of Nup153 FG domains [101].

1.6.2 The Virtual Gating Model

Molecules which enter a confined volume suffer from a decrease in motional freedom which costs them energy in form of entropy. This general fact builds the basis of the "virtual gating" or "Brownian affinity gating" model [13, 105]. Accordingly, an entropic price has to be paid to place a molecule into the NPC central channel. With increasing size of the molecule, the entropic penalty rises to pass through the central channel. Above a certain size, the probability of a molecule to diffuse through the central channel is negligible, which makes the NPC effectively impermeable for larger molecules. Densely packed FG Nups add to the entropic cost, since they occupy additional space in and around the channel volume. Disordered FG domains are thought to act as "entropic bristles" [105] - they randomly dither around due to thermal forces which allows them to explore a large volume around their anchoring point [106]. Molecules which move on the same timescale are likely to be expelled of this volume. The entropic barrier can be overcome by binding to FG repeats [13, 105]. In terms of the Gibbs's free energy the enthalpy gain from binding lowers the barrier energy (ΔG) by counteracting to the decrease in entropy (Figure 1.10). For a sufficient low energy barrier ($\sim k_B T$), diffusion of macromolecules is possible. This accounts for observation that nuclear accumulation of nuclear transport receptors is orders of magnitude faster than that of similarly sized and passively traversing molecules [9, 12].

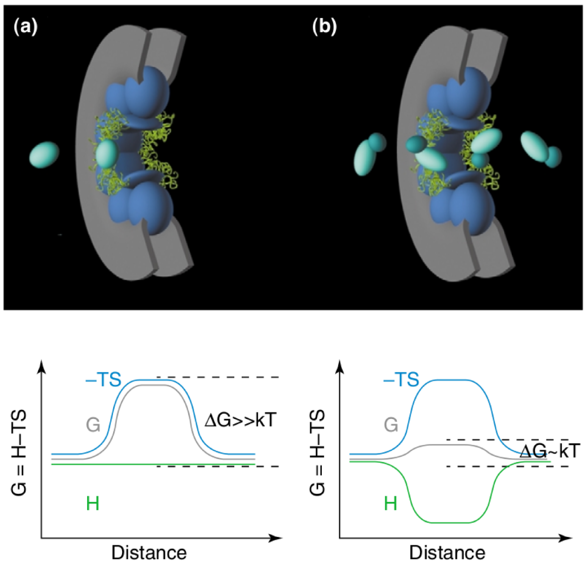

FIGURE 1.10: The virtual gating model. The model suggests that stochastic movements of FG domains (green) at the pores periphery act as an entropic barrier ($\Delta G \gg k_B T$) against non-specific molecules (light turquoise). Binding of NTRs (dark turquoise) lowers the barrier energy ($\Delta G \sim k_B T$) due to enthalpy gain and transport of cargo (light turquoise) through the NPC (blue) is possible. Reproduced from Rout, *et al.* [105].

1.6.3 The Polymer Brush Model

End-on surface grafted polymers generally tend to stretch away from their anchoring point when densely packet next to each other [107]. Based on the close proximity of FG Nups anchored onto the NPC channel wall [13], the polymer brush model emanates from the notion that such close-packing causes the FG Nups to stretch their intrinsically disordered FG domain away from their anchoring point, which resembles a polymer brush.

Based on mechanical measurements in the nanoscale of surface-grafted Nup153 FG domains, Lim, *et al.* could show that close-packed FG domains display compression characteristics resembling those of molecular brushes, but not hydrogels [36, 71]. Reproducing the effect on the NPC barrier in cells, FG domain brush treatment with hexanediol led to a collapse that was fully reversed after restoring initial buffer conditions [71].

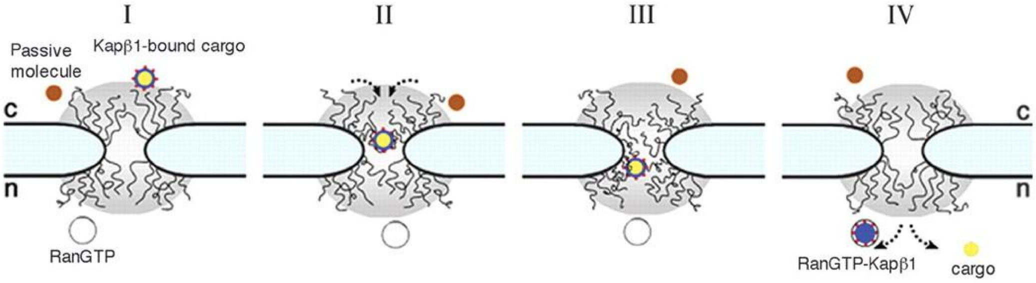

FIGURE 1.11: The polymer brush model. In absence of Kapβ1, FG domains form a corona-like barrier (I). NTR-FG binding induces a local collapse (II) where the NTR-cargo complex is drawn into the pore. After NTR-cargo translocation (III) the complex gets released upon binding of RanGTP in the nucleus (IV). Reproduced from Lim, *et al.* [36].

Binding of Kapβ1 to Nup153 brushes induces a conformational change in the FG domains which is indicated by a overall collapse of the brush [36]. Upon removal of bound Kapβ1 the collapse was reversed and the entropic barrier was re-established. Based on these results, the polymer brush model proposes that FG domains form a corona-like entropic barrier on both sides which repels non-specific molecules from entering the pore by exhibiting stochastic fluctuations (Figure 1.11). This barrier can only be overcome by NTRs that are able to bind FG domains. Binding leads to a collapse of FG domains which causes the NTRs to be drawn into the pore. By randomly moving from one FG domain to the next, each NTR binding event is accompanied by a local collapse inside the pore. In turn, each unbinding causes the

FG domains to re-extend and therefore restore the barrier function.

By using antibodies against the freely moving end of Nup153 [30], immunogold electron microscopy on *Xenopus laevis* NPCs revealed reversible collapse of Nup153 as a function of Kapβ1 binding [36]. At steady-state, Nup153 was predominantly found in the vicinity of the nuclear basket. Microinjection of 2 μM Kapβ1 produced a striking phenotype that localized at the distal ring. Subsequent injection of 8 μM RanGTP returned Nup153 to its steady-state distribution (Figure 1.12). This corroborates the polymer brush model which is based on the notion that binding of Kaps induces conformational changes in FG Nups.

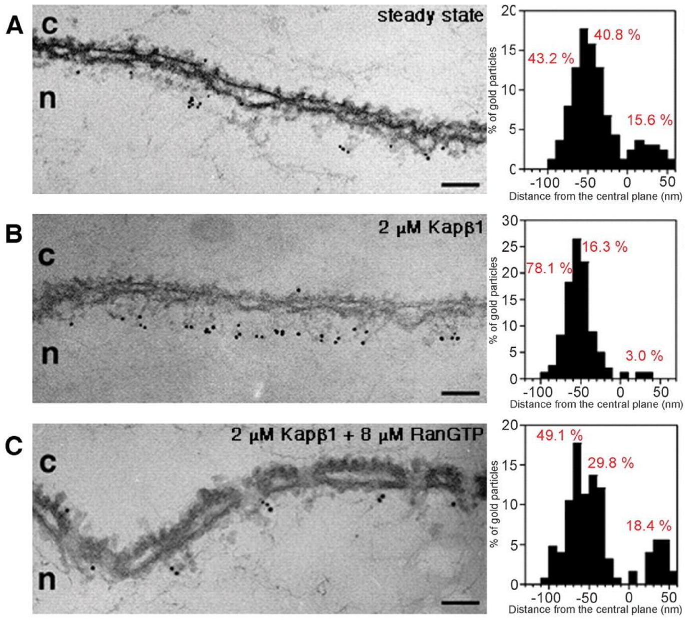

FIGURE 1.12: Reversible collapse of Nup153 in the NPC revealed by immunogold electron microscopy. Histograms show the position of Nup153 relative to the central plane of the NPC (0 nm on the x-axis). The distal ring, the nuclear ring and the cytoplasmic ring moieties are located between -100 nm and -50 nm, -50 nm and 0 nm, and 0 nm to 60 nm. **(A)** The free end of Nup153 diffuse in the periphery of the NPC at steady-state. **(B)** Upon injection of 2 μM Kapβ1, Nup153 is predominantly found at the distal ring, indicating a collapse of Nup153 to the anchoring point. **(C)** The presence of 8 μM RanGTP reverses collapse of Nup153 which returns to its initial steady-state distribution. Reproduced from Lim, *et al.* [36].

Relaxation times of a random peptide coil are in the range of microseconds which is orders of magnitudes faster than the millisecond transport rates in NCT [108]. This dynamic behavior allows for rapid translocation of NTRs while maintaining the barrier integrity towards non-specific molecules [36]. As a consequence of the molecular brush model, Kaps are moving close to the wall of the channel, which is in agreement with observations in cells [109]. Although collapse was measured at low, non-physiological concentrations in the nanomolar range [36], subsequent experiments on planar brushes revealed that after initial layer collapse, FG domains can incorporate large amounts of Kapβ1 and extend even further at physiological concentrations (Chapter 5) [110, 111]. This underlines the conformational sensitivity of close-packed FG domains on NTR occupancy.

1.6.4 Reduction of Dimensionality Model

Inside the cell, the time needed for a diffusing molecule to find its binding partner is strongly dependent on the molecules size and the space the search process has to cover during a three-dimensional random walk. This is significantly optimized when the search process is confined to one- or two-dimensions. This was first proposed by Adam and Delbrück as the principle of reduction of dimensionality (ROD) [112]. Such a process requires that one binding partner is localized on a large structure of lower dimensionality, e.g. the NPC channel wall (Figure 1.13). Based on ROD, Peters, *et al.* proposed a model of nucleocytoplasmic transport [95, 113, 114].

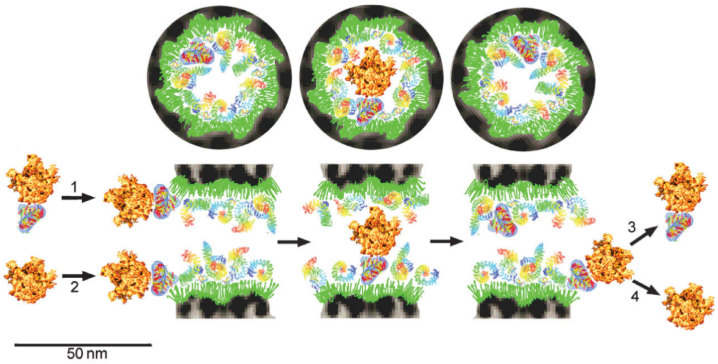

FIGURE 1.13: Reduction of Dimensionality Model. NTR-cargo complexes formed in the cytoplasm (1) or directly at the NPC periphery (2) exhibit a two-dimensional random walk along the hydrophobic FG domain surface (green). After successful translocation, cargo dissociates from the FG domains in complex with the NTR (3) or gets released directly at the periphery (4). A high number of NTRs is occupying the channel at steady-state, leaving a small central channel for passive diffusion. Reproduced from Peters, *et al.* [95].

The model suggests that the majority of all FG domains are collapsed *in vivo*, which extends on the notion that FG domains exhibit high conformational sensitivity to ligand binding [36]. Indeed, given the high cellular concentration of Kaps, it is likely that the FG domains are saturated at steady-state [95, 115]. The high density of FG domains in a collapsed state composes a coherent FG layer which resembles a “hydrophobic surface” [116]. Accordingly, Kaps are hypothesized to bind to this layer due to to their FG domain affinity. But at the same time, their multivalent nature allows them to retain substantial degree of lateral mobility. After binding, Kaps are thought to ferry cargo along the walls by random diffusion in two dimensions. As a consequence, diffusion of NTRs through the NPC is substantially shorter. Nuclear accumulation of FG domain binding NTRs is observed to be 10 – 100 times faster than that of passively diffusing molecules of similar size. This can be seen as a consequence of ROD [9, 12]. In agreement with the ROD model, single molecule tracking experiments revealed that Kap-facilitated transport occurs along the channel wall, while passive molecules are confined in the center of the pore [109]. Although many properties of NPC transport can be explained based on experimental evidence for ROD in artificial systems other than that of NPCs [117, 118], direct experimental evidence for ROD *in vivo* is still missing.

1.6.5 The Forest/Two-Gate Model

Patel, *et al.* and Yamada, *et al.* could show that FG Nups can be classified into two separate categories based on their structural and chemical heterogeneity [38, 119]. FG domains with low charge content adopt globular, collapsed coil configurations (e.g., “shrubs”), whereas others adopt more dynamic, "extended coil" conformations and are characterized by a high charge distribution. Several FG domains exhibit a bimodal distribution of compact and extended structures along their polypeptide chain and accordingly, are termed “trees”. Based on these three conformational classes, the “forest” model suggests that FG domain organization within the NPC channel generates distinct transport zones that differ in their physiochemical properties [119]. The central channel is dominated by sticky globular conformations located at the free end of FG Nups which form a cohesive meshwork through hydrophobic interactions (zone 1; Figure 1.14). These cohesive FG domains are linked to the NPC scaffold via non-cohesive domains which are in a relaxed or extended conformation reminiscent of a molecular brush (zone 2).

Simulations of an NPC exclusively filled with FG Nups (Nsp1p) of “tree” like conformation could reproduce a similar architecture, albeit under the assumption of

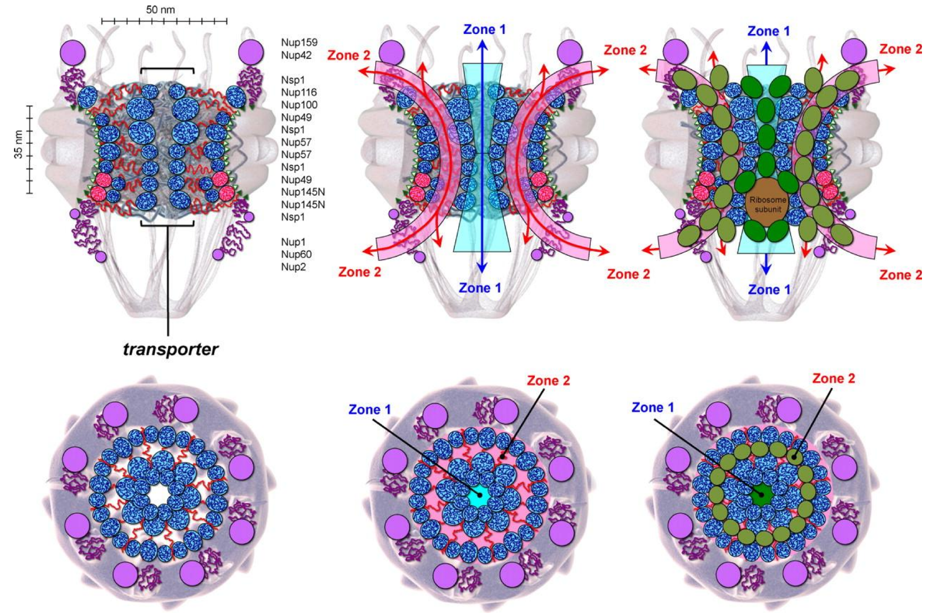

FIGURE 1.14: The Forest/two-gate model. Based on yeast FG Nups properties, the NPC channel exhibits distinct zones for traffic. Cohesive FG domains (blue) oriented towards the center of the channel form a cohesive meshwork in zone 1. More extended repulsive FG domains (red) form zone 2. NTR transit is depicted in dark green (zone 1) and light green (zone 2). Reproduced from Yamada, *et al.* [119].

minimal tethering effects [120]. In the forest model, transport of small cargo loaded Kaps or Kaps alone is limited to zone 2. To facilitate transport of larger cargo, e.g. ribosomal subunits or mRNA, the flexible domains are able to respond with expansion or contraction which allows transport through zone 1. Passive diffusion of small molecules takes place in both zones. As proposed in the virtual gate and polymer brush model, repulsive FG domains on both sides of the NPC form peripheral gates at the entrance to zone 2. This supports a two-gate model of NPC architecture where a central diffusion gate is formed by a meshwork of cohesive FG domains and the two peripheral gates are composed of repulsive FG domains that can function as entropic bristles. Therefore, this model combines both properties of the selective phase and the virtual gate/polymer brush model, respectively. The model is supported by immunogold electron microscopy localization of instantly trapped cargoes in cells, where small cargoes are preferentially found at the periphery of the channel and larger mRNA complexes predominantly localized in the central channel [121]. Spatial information obtained from single molecule trajectories in functional NPCs revealed that small passively diffusing molecules exhibit a high density in the central channel [109]. This findings are at odds with the proposed existence of a peripheral zone allowing passive diffusion.

1.7 Motivation and Aim of the Thesis

The fact that a number of models exist in parallel all trying to explain NCT is mostly based on the lack of experimental validation *in vivo*. To date, many of the results are at least partly based on data obtained from experiments *in vitro* and *in silico*. This allows for different interpretations and opens door for a multiplicity of models. Performing meaningful experiments on working NPCs in living cells is a challenging task. Especially since the spatial and temporal dimensions of the processes within NPCs are at the limits of todays technical possibilities. Other problems include the determination of structure-function relationship which arise from the disordered properties of FG domains.

Given the high cellular abundance of NTRs and their affinity to FG domains, it seems certain that NTR occupancy must be taken into account when studying barrier functionality in NCT, which is not the case for several models proposed (i.e., gel, brush and virtual gate). Short ms-dwell times of molecules in NCT require a low affinity which is a prerequisite for transient interactions. This is conflicting with NPC rejection of weakly binding molecules [42, 68]. At steady-state, a high number of NTRs occupy the NPC simultaneously [115]. This suggests, that FG domains exhibit promiscuous binding which is a general hallmark of IDPs [122]. How the barrier functionality is maintained under constant binding and unbinding of different NTRs and how the binding of one type of NTR affects the binding of the others is not known.

The object of this thesis was to

1.) reconcile the apparent paradox of high binding affinities of NTR-FG domain interactions measured *in vitro* and rapid transport rates measured *in vivo*.

2.) investigate the effect of promiscuous binding of FG Nups to multiple NTRs on the NPC barrier function and kinetics of other molecules.

In order to address these objectives experimentally, I used SPR to investigate Kapβ1 binding to surface-tethered FG domains of yeast Nsp1p. This was compared to the binding of NTF2 and NTF2-W7A. In addition, I extended the standard SPR approach with a novel technique developed by Schoch, *et al.*, which allows for an estimation of the ligand layer height using non-interacting BSA molecules *in situ* [111, 123]. After characterizing the binding of Kapβ1 and NTF2 to FG domain layers individually, I utilized the property of long-lived Kapβ1 interactions to examine the binding of NTF2 while FG domains were preloaded with Kapβ1. This was compared to competitive Kapβ1 binding to pristine FG domain layers in a physiological background of NTF2.

My results show that a slowly exchanging Kapβ1 phase coexists with a fast phase, which dominates transport kinetics due to limited binding with pre-occupied FG Nups at physiological Kapβ1 concentrations. Similarly, NTF2 binding to Kapβ1-preloaded FG domains is dominated by weak short-lived interactions. These novel observations suggest that binding promiscuity confers kinetic advantages to NTF2 and reinforces the proposal that Kapβ1 contributes to the integral barrier function of the NPC.

1.8 Thesis Layout

Chapter 1 introduces the functional architecture of the NPC. The current understanding of nucleocytoplasmic transport and its functional components is summarized and followed by a synopsis of prevailing models describing NPC function. Protein purification and characterization is presented in Chapter 2 together with Materials and Methods and a succinct derivation of surface plasmon polaritons and its resonance conditions. Structural characterization of surface-tethered Nsp1p FG domains are presented in Chapter 3, followed by detailed morphological, equilibrium binding and kinetic analysis of Kapβ1 and NTF2 binding to pristine Nsp1p FG domain brushes in Chapter 4. The impact of promiscuous binding of yeast Nsp1p on the kinetics of NTF2 is presented in Chapter 5. Finally the thesis is concluded in Chapter 6.

Chapter 2

Materials and Methods

2.1 Expression and Purification of Proteins

In this Chapter the cloning, expression and purification of the proteins used in the thesis is specified. All in all, five different proteins were used in this work: Kapβ1, NTF2, NTF2-W7A and yeast FG domains Nsp1p-5FF and Nsp1p-12FF, respectively. Except for NTF2-W7A, all proteins were purified on an Äkta protein purification system (Äkta Purifier 100/10 system, GE Healthcare).

2.1.1 Expression and Purification of Kapβ1

The 876 residues long full-length human Kapβ1 was amplified by PCR and cloned into a NcoI-BamHI digested pETM-11 expression vector [124]. In addition to the full-length sequence an N-terminal His_6-tag and following TEV-cleaveage site (MKHHHHHHPMSDYDIPTTENLYFQGA) was added. His-tagged Kapβ1 was grown at

37 °C to OD_{600} 0.6 in *E. coli* BL21 (DE3) cells and expressed overnight at 30 °C induced by 0.5 mM IPTG. Collected cells were lysed by incubation with lysozyme (30 min, 10 mg/400 ml bacterial culture) in buffer (10 mM Tris, pH 7.5/100 mM NaCl/1 mM DTT) which additionally contained Dnase, Pefabloc and protein inhibitors. The resulting lysates were spun down at 40000 x g for 30 min and the supernatant was applied onto a Ni column (cOmplete His-tag purification column, Roche) in buffer (10 mM Tris, pH 7.5/100mM NaCl/1 mM DTT) where recombinant Kapβ1 was eluted using an Imidazole gradient from 10 mM to 500 mM. Fractions containing high concentrations of Kapβ1 were pooled and further purified using size exclusion (HiPrep 16/60 Sephacryl S-200, GE Healthcare) in buffer (10 mM Tris, pH 7.5/100mM NaCL/1 mM DTT). In cases where the protein concentration was too low (i.e., < 5 µM) the pooled fractions were further concentrated by 2800 x g (10k, Amicron ultra-4, Merck Millipore, Inc.). Purified protein was shock-frozen using liquid nitrogen and stored at −80 °C. Typical stock concentrations of Kapβ1 were 10 – 15 µM.

2.1.2 Expression and Purification of NTF2

The 127 residues long full-length rat NTF2 coding sequence [91] was cloned into the NdeI and XhoI sites of the T7 expression vector pET15b which adds an N-terminal His_6-tag (MGSSHHHHHHSSGLVPRGSHM) to the wild-type sequence. The construct was transformed into *E. coli* strain BL21 (DE3) CodonPlus RIL, grown at 37 °C to OD_{600} 0.6 and expressed over night at 30 °C induced by 0.5 mM IPTG. Collected cells were lysed by incubation with lysozyme (1h at 4 °C) in buffer (10 mM Tris, pH 7.5/100 mM NaCl/1 mM DTT/10mM Imidazole) which additionally contained Dnase, Pefabloc and protein inhibitors. Lysate was spun down at 40000 x g for 1 h at 4 °C. The supernatant was applied onto a Ni column (cOmplete His-tag purification column, Roche) in buffer (10 mM Tris, pH 7.5/100mM NaCl/1 mM DTT) where recombinant NTF2 was eluted using an Imidazole gradient from 10 mM to 500 mM. Fractions containing high concentrations of NTF2 were pooled and ran through size a exclusion column (HiLoad 16/60 Superdex S-75, GE Healthcare) in phosphate buffered saline (GIBCO PBS, Lifetechnologies). Purified protein was shock-frozen using liquid nitrogen and stored at $-80\,°C$. Typical stock concentrations of NTF2 were ~250 – 300 μM.

2.1.3 Expression and Purification of W7A-NTF2

Mutant NTF2 where Trp7 was exchanged by Ala was obtained by PCR-based site-specific mutagenesis as described [125, 126]. The sequence was cloned into the T7 expression vector pET15b, expressed in *E. coli* BL21 (DE3) and purified using ion-exchange chromatography and gel filtration as described[1] [127].

2.1.4 Expression and Purification of FG domains Nsp1p-5FF and Nsp1p-12FF

Two different fragments of the yeast Nsp1p FG domain, Nsp1p-5FF (residues 262 – 359; 1 x FG, 4 x FSFG) and Nsp1p-12FF (residues 262 – 492; 1 x FG, 11 x FSFG) were

---

[1] Proteins were expressed and purified by Neil J. Marshall in the lab of Murray Stewart, Cambridge.

cloned via NcoI and HindIII sites into a modified pET30a vector (Novagen) that had its thrombin protease recognition site changed for TEV protease and Cys-Cys-Trp added after its initiator Met codon. Both final constructs contained N-terminal 2 x Cys –, His_6 – and S – tags (MCCWHHHHHHSSGLVPRGSGMKETAAAKFERQHMDSPDLGTGSENLYFQGA)[2]. Proteins were expressed in *E. coli* BL21(DE3) CodonPlus RIL cells by growing at 37 °C to OD_{600} 0.6 and inducing with 0.5 mM IPTG overnight at 25 °C. Cells were lysed in buffer (50 mM NaPi, pH 7.5/200 mM NaCl/10mM Imidazole/1% Tween 20/2 mM β-mercaptoethanol) for 1 h at 4 °C. Lysate was spun down at 40000 x g for 1 h at 4 °C and was applied onto a Ni column (cOmplete His-tag purification column, Roche) in buffer (10 mM Tris, pH 7.5/100mM NaCl/1 mM DTT) and recombinant fragments of Nsp1p were eluted using an Imidazole gradient from 10 mM to 500 mM. Fractions containing high concentrations of Nsp1p fragment were pooled and ran through size a exclusion column (HiLoad 16/60 Superdex S-75, GE Healthcare) in PBS. Purified protein was shock-frozen using liquid nitrogen and stored at −80 °C. Typical stock concentrations were ∼100 µM.

2.2 Protein Characterization

2.2.1 Protein Quality

In all cases, the protein quality was assessed by PAGE at 0.1% sodium dodecyl sulfate (SDS) and concentrations were measured by the absorption at 280 nm (Nanodrop 2000c, Thermo Scientific). Protein extinction coefficients were obtained using the

---

[2] Plasmids were a kind gift of Murray Stewart, Cambridge.

ProtParam program available from the SIB Bioinformatics Resource Portal ExPASy (http://web.expasy.org/protparam/).

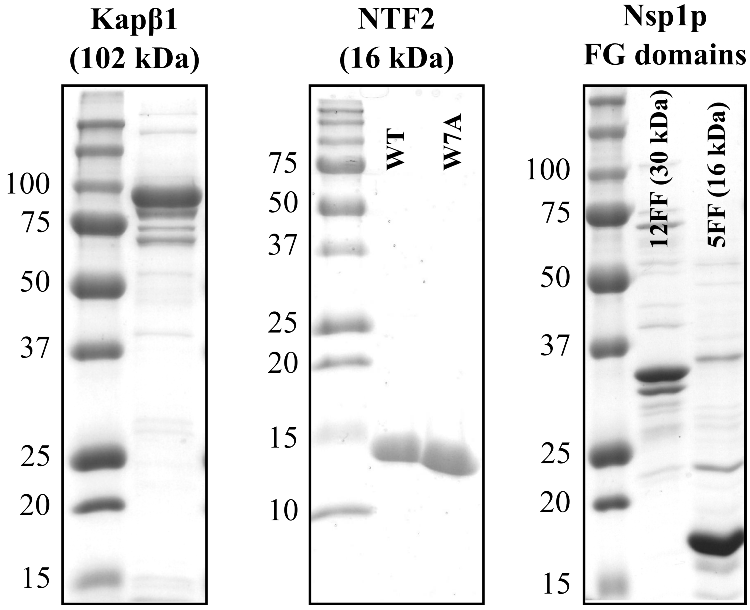

FIGURE 2.1: 12% PAGE (0.1% SDS) of Kapβ1 and 15% PAGE (0.1% SDS) of NTF2, NTF2-W7A, Nsp1p-12FF and Nsp1p-5FF. Note that NTF2 runs at ~14 kDa which is close to the calculated monomer weight of 16.7 kDa. In physiological buffer (e.g., PBS), NTF2 forms a homodimer with a molecular weight of 33.5 kDa [87].

2.2.2 Dynamic Light Scattering

Dynamic light scattering (DLS) measurements (Zetasizer Nano, Malvern Instruments Ltd, Worcestershire, United Kingdom) were performed with all proteins used in this work. Proteins were prepared in buffer (PBS/1mM DTT) at a concentration of ~0.5 – 1 mg/ml. Prior to DLS measurements, the protein solutions were centrifuged at 16000 x g for 15 min to degas them and precipitate possible dust or aggregate particles. Each measurement was done at 25 °C. As input parameters the refractive index for the proteins was $n_p = 1.45$ and for the dispersant (i.e., water)

$n_d = 1.330$. The corresponding viscosity was 0.8872 cP (1P = 0.1 Pa·s). The hydrodynamic size was then calculated using the manufacturer's software (Zetasizer Software 7.02, Malvern) by fitting the intensity distribution to the correlation curves. The measured hydrodynamic diameters of the proteins used in this work are given in Table 2.1.

Protein	Hydrodynamic Diameter d_h (nm), ±SD	Polydispersity Index[a]
Kapβ1	10.2 ± 1.6	0.3
Nsp1p-5FF	8.7 ± 2.5	0.3
Nsp1p-12FF	8.6 ± 2.7	0.1
NTF2	5.6 ± 1.6	0.05

[a] The polydispersity index ranges from 0 to 1, e.g., fully monodisperse to maximal polydispersity of the sample.

TABLE 2.1: Dynamic light scattering measurements of Kapβ1, NTF2, Nsp1p-5FF and Nsp1p-12FF.

The DLS results show that the hydrodynamic diameter d_h of NTF2 is only half of that from Kapβ1. By simply calculating the "protein volume" as d_h^3, Kapβ1 is about 8 times bigger with ∼1000 nm^3 when compared with the volume of ∼125 nm^3 of NTF2. Although the Nsp1p-5FF is 133 residues shorter than Nsp1p-12FF the measured hydrodynamic diameters are indistinguishable. This could be due to the high polydispersity in the sample of Nsp1p-5FF. Fits and DLS measurement quality of Kapβ1, NTF2 and both Nsp1p fragments are shown in Figure 2.2.

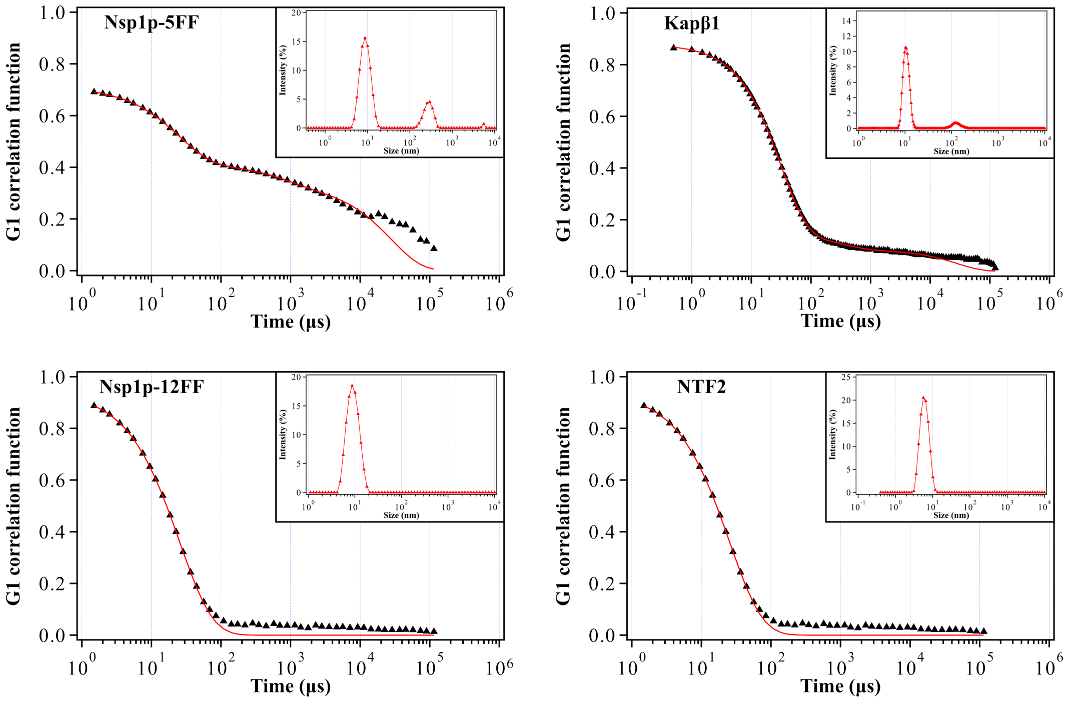

FIGURE 2.2: Dynamic light scattering measurements of Kapβ1, both Nsp1p FG-domain fragments and NTF2. The first-order correlation function and fit (red solid line) together with the resulting intensity distribution (inset) are shown.

2.3 SPR Theory

Plasmon resonances were first observed in 1902 by Wood [128] when he illuminated a metallic diffraction grating with polymorphic light and observed a pattern of unusual dark bands in the spectrum of the diffracted light. Although he speculated about the nature of this anomaly, a clear answer to the phenomenon was not provided. In 1958 Turbadar measured a sudden drop in the reflectance near the critical angle of total reflection for p-polarized light on non-opaque aluminum films [129], but the effect was not linked to surface plasmons at this time. Turbadar's results were explained by Otto in 1968, who demonstrated that the drop of reflectivity in the attenuated total reflection (ATR) method is linked to excitations of surface plasmons [130]. In the same year, by using another configuration of ATR, Kretschmann and Raether successfully excited surface plasmons [131]. The pioneering work of Otto, Kretschmann and Raether led to the development of convenient methods for the excitation of surface plasmons and their integration into modern optics.

2.3.1 Surface Plasmon Polaritons

Electromagnetic excitations in the infrared or visible-frequency range that propagate along an interface between a conductor and a dielectric medium, are generally known as surface plasmon polaritons (SPPs) [132]. They represent bound modes along the interface in much the same way than that of light guided by an optical fiber, with a particular characteristic of subwavelength-scale evanescent confinement perpendicular to the interface. The physical properties of SPPs can be deduced from the Maxwell's equations applied to the interface of a conductor and a dielectric.

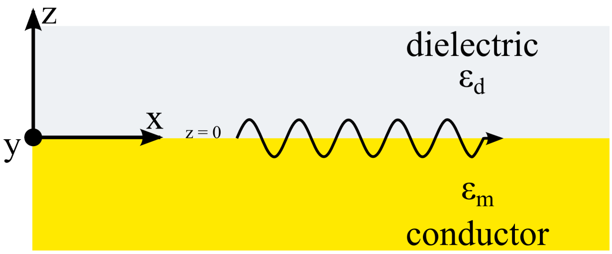

FIGURE 2.3: The most basic geometry which is able to sustain SPPs at the interface composed of a metal and a dielectric (conductor) media.

The most basic geometry which is able to sustain SPPs is that of a single flat interface formed between a dielectric (e.g. aqueous buffer or air) on top of a metal (e.g. gold) as illustrated in Figure 2.3. The upper half space ($z > 0$) is characterized by a positive real dielectric constant ε_d, whereas the lower half space ($z < 0$) is described by a dielectric function, which in the case for metals following the Drude free-electron model is [133]

$$\varepsilon_m(\omega) = \varepsilon_0 \left(1 - \frac{\omega_p^2}{\omega^2 - \mathrm{i}\omega\nu} \right) \tag{2.1}$$

where ε_0 is the free-space permittivity, ν is the collision frequency and ω_p is the well-known plasma frequency

$$\omega_p = \sqrt{\frac{Ne^2}{\varepsilon_0 m_e}} \tag{2.2}$$

with N being the concentration of free electrons, and e and m_e are the electron charge and mass, respectively. In order to have metallic character, it is required that the real part of ε_m, $\mathrm{Re}[\varepsilon_m(\omega)] < 0$. This requirement is fulfilled for metals when $\omega < \omega_p$. Assuming translational invariance along the direction of propagation, linear isotropic and non-magnetic media, which commonly constitute optical waveguides, a propagating electric wave at the interface, as defined in Figure 2.3, can be described as

$$\mathbf{E}(x, y, z) = \mathbf{E}(z) e^{\mathrm{i}\beta x} \tag{2.3}$$

where the complex parameter β is called the *propagation constant* of the traveling wave resembling the component of the local wave in the direction of propagation. Based on the *Helmholtz equation* ($\nabla^2 \mathbf{E} + k_0^2 \varepsilon \mathbf{E} = 0$) the wave equation for the system can be written as

$$\frac{\partial \mathrm{E}(z)}{\partial z^2} + (k_0 \varepsilon - \beta^2)\mathrm{E} = 0 \tag{2.4}$$

where $k_0 = \omega / c$ is the wave vector of the propagating wave in free space. Naturally, a similar equation describes the magnetic field $\mathbf{H}$. Equation 2.4 is the basis for the general analysis of guided electromagnetic modes in waveguides [134]. Solving Eq. 2.4 for $\mathbf{E}$ and $\mathbf{H}$, and for harmonic time dependence ($d/dt = -\mathrm{i}\omega$; described in detail in, e.g., [135]) one obtains two set of self-consistent solutions with different polarization of the propagating waves. The first set are transverse magnetic (TM or p) modes, where the only non-zero components are E_x, E_z and H_y. The second set are the transverse electric (TE or s) modes, where only H_x,H_z and E_y are non-zero components. For TM modes, the system of equations is

$$\mathrm{E}_x = -\mathrm{i}\frac{1}{\omega \varepsilon_0 \varepsilon}\frac{\partial \mathrm{H}_y}{\partial z} \tag{2.5a}$$

$$\mathrm{E}_z = -\frac{\beta}{\omega \varepsilon_0 \varepsilon}\mathrm{H}_y \tag{2.5b}$$

with the TM mode wave equation

$$\frac{\partial^2 \mathrm{H}_y}{\partial z^2} + (k_0^2 \varepsilon - \beta^2)\mathrm{H}_y = 0. \tag{2.6}$$

For TE modes, the equivalent set of equations is

$$\mathrm{H}_x = \mathrm{i}\frac{1}{\omega\mu_0}\frac{\partial \mathrm{E}_y}{\partial z} \tag{2.7a}$$

$$\mathrm{H}_z = \frac{\beta}{\omega\mu_0}\mathrm{E}_y \tag{2.7b}$$

with the corresponding equation for TE modes

$$\frac{\partial^2 \mathrm{E}_y}{\partial z^2} + (k_0^2 \varepsilon - \beta^2)\mathrm{E}_y = 0. \tag{2.8}$$

For the geometry given in Figure 2.3, the solutions for TM propagating waves confined to the interface are for $z > 0$ (i.e., dielectric)

$$\mathrm{H}_y(z) = \mathrm{A}_d e^{\mathrm{i}\beta x} e^{-k_d z} \tag{2.9a}$$

$$\mathrm{E}_x(z) = \mathrm{i}\mathrm{A}_d \frac{1}{\omega\varepsilon_0\varepsilon_d} k_d e^{\mathrm{i}\beta x} e^{-k_d z} \tag{2.9b}$$

$$\mathrm{E}_z(z) = -\mathrm{A}_d \frac{\beta}{\omega\varepsilon_0\varepsilon_d} e^{\mathrm{i}\beta x} e^{-k_d z} \tag{2.9c}$$

and for $z < 0$ (i.e., metal)

$$\mathrm{H}_y(z) = \mathrm{A}_m e^{\mathrm{i}\beta x} e^{k_m z} \tag{2.10a}$$

$$\mathrm{E}_x(z) = -\mathrm{i}\mathrm{A}_m \frac{1}{\omega \varepsilon_0 \varepsilon_m} k_m e^{\mathrm{i}\beta x} e^{k_m z} \tag{2.10b}$$

$$\mathrm{E}_z(z) = -\mathrm{A}_m \frac{\beta}{\omega \varepsilon_0 \varepsilon_m} e^{\mathrm{i}\beta x} e^{k_m z} \tag{2.10c}$$

where

$$\beta = \frac{\omega}{c}\sqrt{\frac{\varepsilon_d \varepsilon_m}{\varepsilon_d + \varepsilon_m}} \tag{2.11a}$$

$$k_d = \frac{\omega}{c}\frac{\varepsilon_d}{\sqrt{\varepsilon_m + \varepsilon_d}} \tag{2.11b}$$

$$k_m = \frac{\omega}{c}\frac{\varepsilon_m}{\sqrt{\varepsilon_m + \varepsilon_d}}. \tag{2.11c}$$

with k_i and A_i ($i = d$ or m for dielectric or metal) describing the components for the wave vectors perpendicular to the interface and the related modal field amplitude, respectively. $\omega/c = k_0 = 2\pi/\lambda$ is the wave vector for light with a free-space wavelength λ. Additionally, the requirement for continuity at the interface makes it impossible for TM polarized surface modes to exist [135].

As follows from equations 2.9 and 2.10, the electromagnetic field of a SPP reaches its maximum at the metal-dielectric interface and exhibits an exponential decay into both media. Such a decay can be characterized by its characteristic penetration

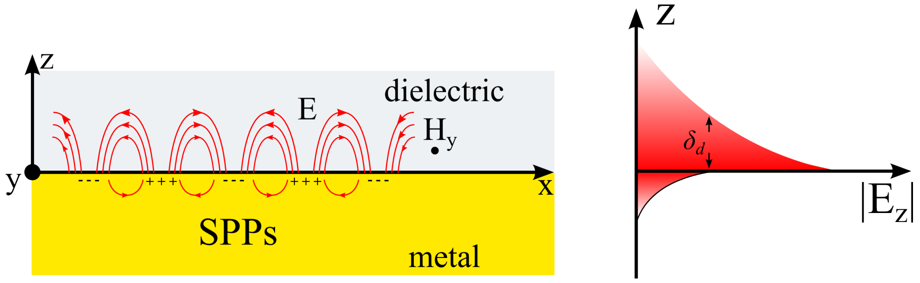

FIGURE 2.4: SPPs at the interface between a metal and dielectric material are a combination of surface charge and electromagnetic wave. Left: Transverse magnetic character (the magnetic field H is in y-direction) and generation of surface charges requires an electric field, E, normal to the interface. Right: The electric field is enhanced near the surface and is decaying exponentially with distance. The decay length of the electric field in the dielectric medium, δ_d, is approximately half of the wavelength of the light involved [136].

depth (or decay length) δ_i, which is defined as the distance from the surface where the field amplitude decreases by a factor of $1/e$:

$$\delta_i = \mathrm{Re}[k_i]^{-1}. \tag{2.12}$$

Therefore, for a SPP confined at the interface, the characteristic penetration depth into the dielectric medium is given by

$$\delta_d = \frac{\lambda}{2\pi}\left(\frac{\varepsilon_d^2}{\varepsilon_m' + \varepsilon_d}\right)^{-\frac{1}{2}} \tag{2.13}$$

where ϵ_m' is the real part of the dielectric constant of the metal. As an approximation, the penetration depth into the dielectric is in the range of half the wavelength λ, which is about ten times larger than the corresponding penetration depth into the metal. However, in real metals, oscillating electrons always experience damping which is described by a non-zero imaginary part of the permittivity $\varepsilon_m = \varepsilon_m' + i\varepsilon_m''$. As a consequence, the propagation constant of SPPs contains a non-zero imaginary part, $\beta = \beta' + i\beta''$, and therefore, the traveling SPPs are damped with a characteristic attenuation length given by

$$\delta_{SPP} = \frac{1}{2\mathrm{Im}[\beta]} \tag{2.14}$$

Typically, the propagation length of SPPs along the metal-dielectric interface ranges between a few micrometers in the visible range and up to 100 µm in the infrared (e.g. the $1/e$ propagation length of gold at a wavelength of $\lambda = 760$ nm is about 10 µm).

2.3.2 Excitation of Surface Plasmon Polaritons

As derived before, SPPs are quasi two-dimensional electromagnetic waves at a metal-dielectric interface with an asymmetric evanescent decay on both sides of the interface. However, excitation of SPPs by three-dimensional light beams is not possible since the SPP dispersion relation curve always lies below the light line of a dielectric or below that of an electromagnetic wave in free-space, which have a linear dispersion relation of $\omega = c\,k_0$ (Figure 2.5).

Therefore, SPP excitation can only be achieved by applying special phase-matching techniques. One of the most frequently used technique to excite SPPs is the so-called Kretschmann configuration in the ATR method [131]. This approach includes a high-refractive index prism with refractive index n_p attached to a metal-dielectric waveguide comprising a thin metal layer with permittivity ε_m and a semi-infinite dielectric with refractive index n_d, where $n_d < n_p$ (Figure 2.6). In the ATR

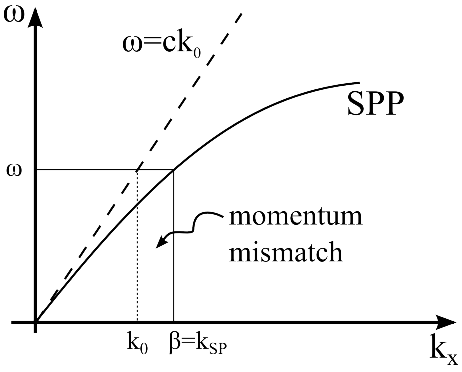

FIGURE 2.5: Dispersion relation of SPPs and electromagnetic waves in free-space. The momentum mismatch problem that has to be overcome for successful coupling of light and SPP modes is shown. SPP modes always have a greater momentum ($\hbar k_{SP}$) than that of free space photons ($\hbar k_0$).

regime, a part of an incident light beam gets reflected back into the prism at the metal / prism interface and a part propagates along the interface while decaying exponentially into the direction normal to the interface, and as such is constituting an evanescent wave. For sufficiently thin layers (< 100 nm for visible and near infrared light) the evanescent wave can penetrate the metal film and couple with SPPs bound at the low-refractive index / metal interface. The propagation constant β^{SPP_0} as defined in equation 2.11a of a SPP propagation along the thin metal film is influenced by the presence of the dielectric material, i.e., the prism on the other side. Therefore, the resulting propagation constant is altered as $\beta^{SPP} = \beta^{SPP_0} + \Delta\beta$, where $\Delta\beta$ accounts for the influence of the prism. For efficient coupling to occur, the propagation constant β^{SPP_0} has to match that of the evanescent wave β^{EW}. In terms of effective index, the coupling condition can be expressed as:

$$n_{ef}^{EW} = n_p \sin\Theta = n_{ef}^{SPP} = \mathrm{Re}\left\{\sqrt{\frac{\varepsilon_d \varepsilon_m}{\varepsilon_d + \varepsilon_m}}\right\} + \Delta n_{ef}^{SPP} \tag{2.15}$$

where n_{ef}^{EW} represents the effective index for the evanescent wave, n_{ef}^{SPP} is the effective index of the SPP and $\Delta n_{ef}^{SPP} = \mathrm{Re}[\Delta\beta\lambda/2\pi]$. Equation 2.15 shows, that only a single angle of incident for a given wavelength matches the criteria that satisfies coupling to surface plasmon polaritons (e.g. for light with $\lambda = 760$ nm and a BK7 glass prism, $\Theta \approx 66.5°$ [137]).

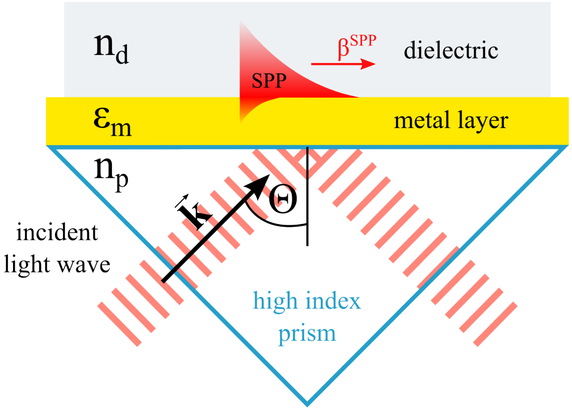

FIGURE 2.6: Kretschman geometry of the attenuated total reflection method for excitation of surface plasmon polaritons. A high refractive index prism (n_p) reflects incident light at the prism metal interface. A part of the light propagates along the interface while decaying exponentially perpendicular to the interface. For thin metal layers this evanescent wave can penetrate the layer and couple to SPPs bound at the metal-low-index dielectric interface. Only a single incident angle Θ for a given wavelength matches the criteria (Equation 2.15) that satisfies coupling.

2.4 Application of SPR

2.4.1 SPR Based Biosensors

Optical sensors are devices which, by optical means, convert a measured quantity of the object of interest to another quantity which is typically encoded into a property of a light wave. In SPR based sensors, SPPs excited at the interface between a metal film and a dielectric medium (superstrate) depend on the refractive index of the superstrate (see Eq. 2.15 in previous Section). A subsequent change in refractive index will change the coupling condition for SPP resonance to occur, which can be observed as a change in characteristics of the optical wave interacting with the SPP. In prism based coupling (e.g. Kretschman configuration; Figure 2.6) incident light gets totally reflected at the high-index prism / metal interface. SPP excitation manifests itself in a minimum of the reflected light intensity which is associated with the transfer of energy from the incident light wave into a surface plasmon and its subsequent dissipation into the metal film. This "dip" in the reflected intensity can be observed at a given angle which is dependent on the refractive index of the low-index dielectric media (e.g., air or water; Figure 2.7).

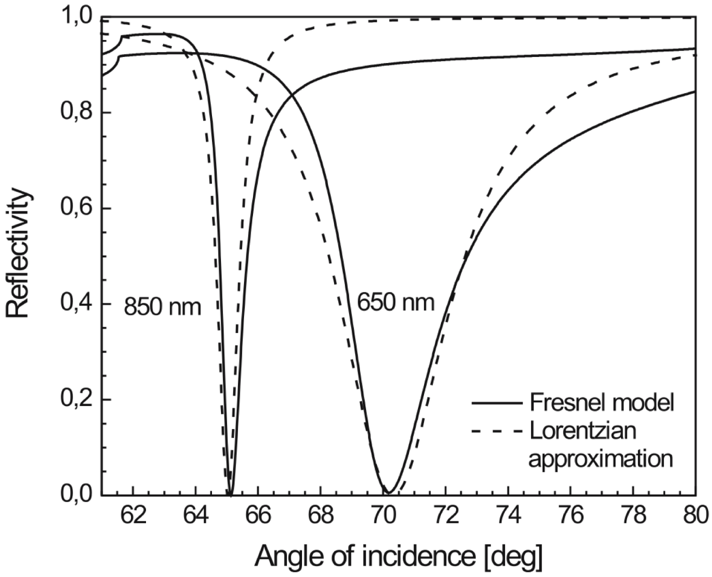

FIGURE 2.7: Polarized reflectivity as a function of angle of incidence calculated for two differnet wavelengths. The Fresnel model (solid line) and its Lorentzian approximation (dashed line) describe the reflectivity on a BK7 glass, gold film, water configuration (gold film thickness of 48 nm for wavelength 650 nm, and 50 nm for wavelength of 850 nm). Reproduced from [137].

Therefore, refractive index changes in a dielectric media within the penetration depth of the evanescent SPP field perpendicular to the interface can be detected by optical means. For example, optical tracking of the typical angle where the minimum of reflected light intensity occurs. Such a device can be utilized for affinity biosensing where SPR based sensing devices incorporate biorecognition elements (e.g. antibody) that are able to interact with single or multiple selected analytes. These SPPs based optical sensors will only be sensitive to molecular processes (binding, adsorption, etc.) within the decay length of the evanescent field (e.g. 350 nm). In other words, binding of proteins onto the metal surface or changes in the sensing volume above the metal surface (e.g., buffer or protein solutions) can be detected as a function of time.

A typical SPR setup and experiment is depicted in Figure 2.8 and Figure 2.9, respectively. Here, the refractive index change is monitored over time. A glass slide with a thin gold layer of ~50 nm thickness (sensor chip) is interfaced with a high-index prism on the sensor glass side. A flow-cell (FC) is used to change the solutions which are in contact with the gold surface of the sensor chip. This system allows for constant flow or quick changes of protein solutions (e.g., injections).

Subsequent changes on the gold surface (e.g. binding of analytes) is detected by a shift of the intensity minimum of the reflected light as a function of time. A typical SPR experiment consists of four steps: i) immobilization of the ligand (e.g. antibodies) onto the sensor surface, ii) injection of analytes (association) which bind to the ligand until they reach steady-state equilibrium (iii), and subsequent washing with buffer that causes the bound analytes to dissociate from the surface (see Figure 2.9). A final regeneration step can be applied to remove all bound analytes from the surface. From such an experiment, kinetic information (association, dissociation) and

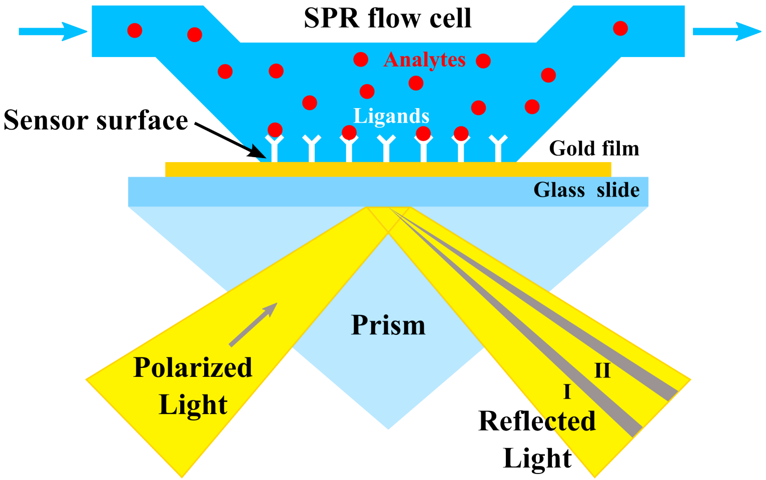

FIGURE 2.8: Basic components of an instrument for SPR biosensing. A glass slide with a thin gold coating is mounted on a high-index prism (Kretschman configuration). Polarized light passes through the prism and gets reflected at the prism/gold interface. Subsequent changes of the refractive index in the detection volume above the sensor surface cause a shift of the intensity minimum of the reflected light due to coupling to SPPs (e.g., I to II). The SPR signal (angle of intensity minimum shift) is proportional to the mass of bound ligand and analyte. A flow cell allows constant flow or rapid exchange of solutions above the gold surface. The SPR signal is recorded as a function of time.

thermodynamic information (equilibrium binding) about the ligand-analyte interaction can be obtained. Since the SPR signal is sensitive to changes not only on the sensor surface but also in the detection volume above the surface, a common way to correct for the bulk response is the use of a second SPR sensor separately addressed via a second FC. The analyte solution then is injected in both FCs simultaneously. While the analyte is binding to the ligand functionalized FC1, the second sensor surface in FC2 is passivated and rejects all analyte. By subtracting the signal of FC2 from FC1, a bulk-response corrected signal can be obtained. In this way the binding signal of analyte and ligand is isolated from the total response that includes bulk contributions.

In this work, SPR (Biacore T100, GEHealthcare) response is measured in response units (RU). The SPR response is proportional to the amount of molecules adsorbed onto the sensor surface. The relation was shown to be 0.10° ± 0.01° = 1 ng/mm^2 for proteins immobilized in a 100-nm dextran hydrogel layer, which is equivalent to 1000 RU = 1 ng/mm^2 [138, 139]. However, this relation has to be refined when small molecules are directly bound to the sensor surface. This is because the given mass-response relation overestimates the protein mass due to the higher evanescent field strength at the gold surface as compared to the dextran layer, which is considerably thicker. For an estimated evanescent field decay length of 350 nm, a more suitable relation of 1300 RU = 1ng/mm^2 can be derived for a typical adlayer of 20 nm height [111].

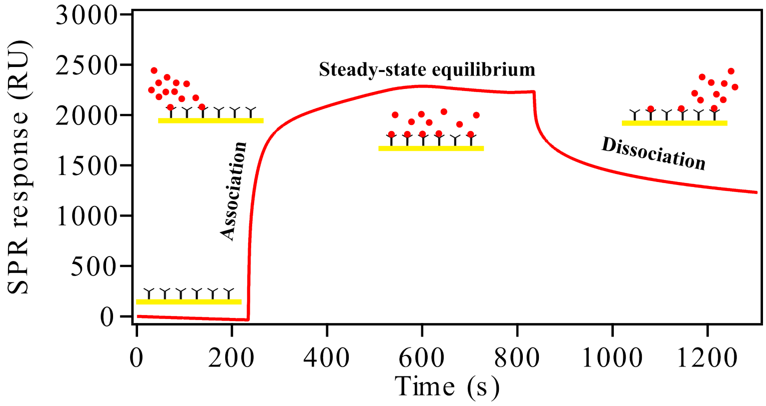

FIGURE 2.9: A typical SPR experiment, showing the relative optical response (RU) versus time. At the beginning, the surface is functionalized with a ligand and RU is set to zero. Upon start of analyte injection of constant bulk concentration at t = 250 s, the SPR signal increases due to analyte binding at the surface (association). At t = 600 s the system reaches equilibrium according to mass-action law. Dissociation of bound analyte is achieved by flushing the flow-cell with buffer starting at t = 850 s. To correct for bulk solution response, all solutions are simultaneously injected onto a passivated reference surface while monitoring both surfaces simultaneously.

2.4.2 Equilibrium Binding Analysis

The binding of two proteins A and B (e.g., ligand and analyte) in its most simple form is given by the bimolecular reaction

$$A + B \underset{k_{off}}{\overset{k_{on}}{\rightleftharpoons}} AB \tag{2.16}$$

where k_{on} is the association rate and k_{off} the dissociation rate constant. The reaction is in equilibrium when the concentrations do not change.

$$\frac{d[AB]}{dt} = k_{on}[A][B] - k_{off}[AB] = 0 \tag{2.17}$$

The association is a second order reaction (dependent on both concentrations [A] and [B]), whereas dissociation follows a first order reaction. Equilibrium is reached according to the mass action law [140] when

$$k_{on}[A][B] = k_{off}[AB] \tag{2.18}$$

Rearranging gives the well known definition of the equilibrium dissociation constant

$$KD = \frac{k_{off}}{k_{on}} = \frac{[A][B]}{[AB]} \tag{2.19}$$

Here, the concentration of analyte $B \gg A$ because of the constant flow above the sensor surface. Therefore the concentration of B does not change over time (d[B]/dt = 0) and is held constant at a given concentration c. Accordingly, Eq. 2.17 changes to

$$\frac{\mathrm{d[AB]}}{\mathrm{dt}} = \mathrm{k_{on}}\,([\mathrm{AB}]_{\mathrm{max}} - [\mathrm{AB}])\mathrm{c} - \mathrm{k_{off}}\,[\mathrm{AB}] \tag{2.20}$$

where $[\mathrm{AB}]_{\mathrm{max}} - [\mathrm{AB}]$ is the concentration of free ligands [A] and $[\mathrm{AB}]_{\mathrm{max}}$ is the concentration of [AB] when all ligands are saturated. This reduces the binding model to a so called pseudo first order reaction. By assigning the SPR response $\mathrm{R_{max}}$ to the concentration of $[\mathrm{AB}]_{\mathrm{max}}$ and $\mathrm{R_t}$ is the signal of [AB] complexes formed at time t, the SPR binding signal change over time is given by

$$\frac{\mathrm{d[R]}}{\mathrm{dt}} = \mathrm{k_{on}}\,(\mathrm{R_{max}} - \mathrm{R_t})\mathrm{c} - \mathrm{k_{off}}\,\mathrm{R_t} \tag{2.21}$$

for the association and

$$\frac{\mathrm{d[R]}}{\mathrm{dt}} = -\mathrm{k_{off}}\,\mathrm{R_t} \tag{2.22}$$

for the dissocation of ligand-analyte complexes on the surface. Accordingly, the equilibrium response $\mathrm{R_{eq}}$ ($\mathrm{dR/dt} = 0$) is given by the Langmuir absorption isotherm

$$\mathrm{R_{eq}(c)} = \frac{\mathrm{R_{max}} \times c}{\mathrm{KD} + c} \tag{2.23}$$

Note that at $\mathrm{R_{eq}/R_{max}} = 0.5$ half of the binding sites are occupied and $\mathrm{KD} = \mathrm{c}$.

Here, for the determination of the apparent equilibrium binding constants of different transport receptors (NTF2, NTF2-W7A and Kapβ1) the SPR response, $\mathrm{R_{eq,i}}$, at steady state as a function of bulk transport receptor concentration c was fitted with a Langmuir absorption isotherm of k components with $\mathrm{k} = 1$ or 2:

$$\mathrm{R_{eq}(c)} = \sum_{\mathrm{k}} \frac{\mathrm{R_{max,k}} \times \mathrm{c}}{\mathrm{KD_k} + \mathrm{c}} \tag{2.24}$$

where $\mathrm{R_{max,k}}$ represents the maximum surface binding capacity for binding species with $\mathrm{KD_k}$. In all cases of close-packed FG domains, the experimental data points for Kapβ1, NTF2 and NTF2-W7A binding were best fit by a two-component Langmuir isotherm.

2.4.3 Kinetic Analysis of Multivalent Interactions

The concept of surface heterogeneity introduced by Svitel, *et al.* [141] was used to estimate the binding kinetics of NTF2, W7A-NTF2 and Kapβ1 interacting with Nsp1p FG-domains. To do so, a discrete set $P_i(k_{on,i}, k_{off,i})$ of total $N = M_{k_{off}} \times M_{k_{on}}$ (i.e., 36 x 36) binding states was used to model the experimentally measured kinetic-binding curves as

$$s_{total}(c,t) = \sum_{i=1}^{N} P_i(k_{off,i}, k_{on,i}) s_i(k_{off,i}, k_{on,i}, c, t) \Delta k_{off} \Delta k_{on} \tag{2.25}$$

where c is the analyte bulk concentration and t is time. The factor $P_i(k_{off,i}, k_{on,i})$ describes the fractional abundance (i.e. “weight”) of the kinetic binding species i which has a theoretical binding response given by $s_i(k_{off,i}, k_{on,i}, c, t)$. The binding states can be represented on a grid of $(k_{off,i}, k_{on,i})$-pairs

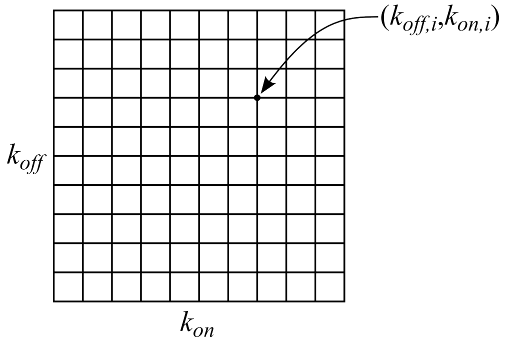

where each grid-point visualizes the weighting $P_i(k_{off,i}, k_{on,i})$ in the 3rd dimension using a contour plot of colors. In this case, for each grid point a full sensogram $s_i(k_{off,i}, k_{on,i}, c, t)$ was constructed according to the experimental parameters, e.g. $c = 0$ for the dissociation phase. To do so, a kinetic model for NTF2 (and W7A-NTF2) binding was used to calculate a sensogram for each pair of $(k_{off,i}, k_{on,i})$ assuming pseudo first order kinetics.

$$\mathrm{L}+\mathrm{D_s} \underset{\mathrm{k_{off,i}}}{\overset{\mathrm{k_{on,i}}}{\rightleftharpoons}} \mathrm{LD_s} \tag{2.26}$$

Here, L are the free binding sites, $\mathrm{D_s}$ is the NTF2 dimer concentration in solution and LD are binding sites occupied with dimeric NTF2 molecules. For the binding of Kapβ1, the model was further extended to mimic the experimentally observed multilayer formation

$$\mathrm{L}+\mathrm{A_s} \underset{\mathrm{k_{off,i}}}{\overset{\mathrm{k_{on,i}}}{\rightleftharpoons}} \mathrm{LA_1} + \mathrm{A_s} \underset{\mathrm{k_{off,i}}}{\overset{\mathrm{k_{on,i}}}{\rightleftharpoons}} \mathrm{LA_2} + \mathrm{A_s} \underset{\mathrm{k_{off,i}}}{\overset{\mathrm{k_{on,i}}}{\rightleftharpoons}} \cdots \underset{\mathrm{k_{off,i}}}{\overset{\mathrm{k_{on,i}}}{\rightleftharpoons}} \mathrm{LA_n} \tag{2.27}$$

with L representing the free binding sites, $\mathrm{A_s}$ is the Kapβ1 concentration in solution and $\mathrm{LA_n}$ are the binding sites occupied by n Kapβ1 molecules. In both cases, the free ligand concentration, L, was modeled as binding sites per surface area given by the size of the transport factor (e.g. 5 x 5 nm^2 for NTF2/W7A-NTF2 and 10 x 10 nm^2 for Kapβ1) because, in this case, the actual distance between FG repeats binding sites was much smaller than the dimension of an individual transport factor. This gave a total number of 4×10^{10} surface sites per mm^2 for NTF2/W7A-NTF2 and 1×10^{10} surface sites per mm^2 for Kapβ1. For the latter, each binding site can accommodate up to 3 Kapβ1 molecules, corresponding to the formation of multilayers. A set of ordinary differential equations describing the kinetic models were solved using the Matlab function ode15s. For Kapβ1, the sensogram was calculated by linearly superimposing $\mathrm{LA}_1 + 2 \times \mathrm{LA}_2 + 3 \times \mathrm{LA}_3$. The concentration of occupied sites LA_n as a fraction of the total binding sites L was compared to the number of layers obtained by dividing the experimental sensogram by 2897 RU for NTF2/W7A-NTF2 and 2223 RU for Kapβ1 [111]. An optimal parsimonious distribution of k_off and k_on describing the experimentally obtained sensogram was obtained by solving the following minimization problem, which was stabilized using Tikhonov regularization in the standard-form:

$$\mathbf{p}_\lambda = \operatorname{argmin}\left\{\| \mathbf{Ap} - \mathbf{b} \|_2^2 + \lambda^2 \| \mathbf{I}(\mathbf{p} - \mathbf{p}^*) \|_2^2\right\} \tag{2.28}$$

where $\mathbf{A} = [\mathbf{s_1}, \mathbf{s_1}, ...\mathbf{s_i}, ...\mathbf{s_N}]$ is a matrix of $N_{dat} \times N$ elements (with $N = M_{k_{off}} \times M_{k_{on}}$ and N_{dat} the number of experimental data points) which contains all calculated sensograms $s_i(k_{off,i}, k_{on,i}, c, t)$, $\mathbf{p}$ is a vector with N elements and contains the set of discrete binding states and $\mathbf{b}$ is a vector of N_{dat} experimental data points. The regularized Tikhonov solution $\mathbf{p}_\lambda$ was computed using the Matlab package Regularization Tools by Per Christian Hansen [142] where $\mathbf{I}$ stands for the identity matrix and $\mathbf{p}^*$ for a null vector. To stabilize the solution in a KD range of applied concentrations the $\mathbf{I}$ diagonal elements were modified by setting KD/c_{max} for $c_{max} >$ KD and c_{min}/KD for KD $< c_{min}$, where c_{max} is the highest and c_{min} the lowest applied bulk concentration in the experimental data set $b(c,t)$. An active set method introduced by Landi and Zama [143] was applied to the Tikhonov regularized solution $\mathbf{p}_\lambda$ in order to obtain nonnegative solutions using the conjugate gradient algorithm in the Matlab package Regularization Tools [142].

2.4.4 Mass Transport Limitation

Mass transport effects will influence the kinetics of binding when the reaction rate is fast compared to the rate of transport [144]

$$\frac{\mathrm{k_{on}R_T}}{\mathrm{k_m}} \geq 1 \tag{2.29}$$

where $\mathrm{R_T}$ is the immobilized receptor concentration in $\mathrm{M \cdot m}$ and $\mathrm{k_m}$ is the mass transport coefficient and $\mathrm{k_{on}}$ is the on-rate of the reaction. Since in my case, the ligand is smaller than the analyte, and so it is the packing of the analyte that actually limits its surface concentration. In the laminar flow conditions that apply in Biacore experiments, $\mathrm{k_m}$ can be calculated as [145]

$$\mathrm{k_m} = 0.98\left(\frac{\mathrm{D}}{\mathrm{h}}\right)^{\frac{2}{3}}\left(\frac{\mathrm{f}}{0.3\mathrm{A}}\right)^{\frac{1}{3}} = 10.22\ \mathrm{\mu m/s} \tag{2.30}$$

where D is the analyses' diffusion coefficient of 70 $\mu m^2 s^{-1}$ (i.e., Kapβ1) [115], f is the volumetric flow rate through the flow cell of 10 µl/min, h and A are the flow-cells' height and area of 40 µ and 1.5 mm^2, respectively. For $k_{on} = 10^4\ M^{-1}s^{-1}$ and $R_T = 1.66 \times 10^{-11}\ M \cdot m$ at maximum Kapβ1 grafting density g = 10 nm (i.e. one monolayer) we arrive at a ratio of $0.016 < 1$. Hence, mass effects should not be limiting in the association under these conditions. Accordingly, a k_{on} of $10^5\ M^{-1}s^{-1}$ results in a ratio of $0.16 < 1$. For $k_{on} = 10^6\ M^{-1}s^{-1}$, mass transport effects might start to influence the kinetics measure as the ratio is $1.6 > 1$. NTF2 even has a higher diffusion coefficient than that given for Kapβ1 [115]. This considerations support the notion that the effect of mass transport limitation for both, NTF2 and Kapβ1, may start to affect kinetic results for $k_{on} \geq 10^6\ M^{-1}s^{-1}$.

2.4.5 Definition of Grafting Distance and NTR Layers

The estimation of the next-neighbor distance, g, between surface bound molecules is straight forward once the mass adsorbed per unit area (for a square lattice) is known for a given molecular weight M_w:

$$g(nm) = \sqrt{\frac{1300 \cdot M_w \cdot 10^{21}}{N_A \cdot \Delta RU}} \tag{2.31}$$

where M_w is the molecular weight of the protein (e.g. Kapβ1), N_A is Avogadro's constant and ΔRU is the SPR response shift upon binding of the protein. This distance, g, can be smaller than the average diameter, d_h, of a single Kapβ1 (ca. 10 nm) or NTF2(-W7A) (ca. 5 nm) molecule because Eq. 2.31 projects all bound molecules to a single plane. The number of layers is calculated using

$$\text{Number of layers} = \frac{{d_h}^2}{g^2} \tag{2.32}$$

In this case, 1 layer of Kapβ1 corresponds to ~1000 Da/nm^2 and 1 layer of NTF2 or W7A-NTF2 corresponds to ~1340 Da/nm^2. Dimensionless SPR response units (RUs) are converted using the relation of 1300 RU = 1 ng/mm^2 [123].

2.4.6 Definition of Stoichiometric Ratio

From the definition of grafting distance, g, as described before in Section 2.4.5, it follows that the number of proteins (e.g. NTF2) per unit area is given by $1/g^2$. Accordingly, a stoichiometric ratio based on mass coverage between NTRs binding to surface grafted FG domains is given by

$$\text{Stoichiometric ratio} = \frac{{g_{\mathrm{NTR}}}^2}{{g_{\mathrm{Nup}}}^2} \tag{2.33}$$

where g_{NTR} stands for the grafting distance of Kapβ1, NTF2 or W7A-NTF2 and g_{Nup} for the grafting distance of the FG domain (e.g. Nsp1p-12FF). For example, a grafting distance g_{NTF2}=5 nm corresponds to a mass of 4 NTF2 molecules per 100 nm^2. On the same area, a mass of 16 Nups with g_{Nup} = 2.5 nm can be bound. This gives a ratio of 0.25 or a mass based stoichiometry of 1 NTF2 per 4 FG Nups. The

NTRs grafting distance can be smaller than its hydrodynamic diameter, which according to Eq. 2.31 in Section 2.4.5 accounts for multi-layer formation. SPR response units (RUs) are converted using the relation of 1300 RU = 1 ng/mm^2 [123].

2.4.7 Determination of the FG Domain Layer Height

As described in Schoch, *et al.* [123], the SPR response of non-interacting BSA molecules injected simultaneously into a passivated reference- and nucleoporin-functionalized flow-cell allows estimation of the layer-height of the nucleoporins grafted on the sensor surface (Figure 2.10).

In this case, densely grafted PUT ($HS{-}(CH_2)_{11}{-}(OCH_2CH_2)_3{-}OH$, Nanoscience) was used to passivate the gold sensor surface, which results in a small passivation layer with known height of 2 nm as measured by ellipsometry [146]. Here, 1% (w/v) BSA was injected and the SPR response (RU) was recorded which was used to estimate a layer-height h as

$$h = \frac{l_d}{2} \ln\left(\frac{R_{ref} m_{BSA}}{R_{BSA} m_{ref}}\right) + d_{ref} \tag{2.34}$$

where $l_d = 350$ nm is the specific decay length of the evanescent field, R_{BSA} and R_{ref} stand for the SPR response of BSA injected into the FG domain functionalized SPR flow-cell and PUT-passivated reference flow-cell, respectively. m_{BSA} and m_{ref} are calibration constants accounting for differences in SPR sensitivity between the flow-cells and d_{ref} = 2nm is the corresponding thickness of the PUT passivation layer.

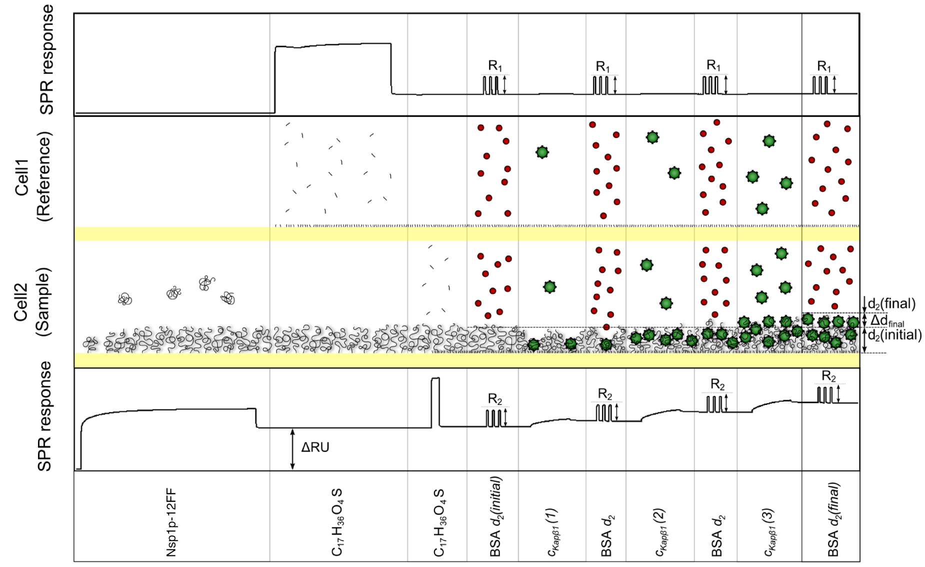

FIGURE 2.10: Measuring conformational changes of surface-tethered FG domains by SPR. R_1 (R_{ref} in Eq. 2.34) and R_2 (R_{BSA} in Eq. 2.34) derive from the presence of non-interacting BSA probes (red) in the PUT passivated cell 1 ($C_{17}H_{36}O_4S$) and FG domain functionalized cell 2 (Nsp1p-12FF), respecively, and are used to estimate the layer height d_2 (h in Eq. 2.34). Changes in layer height due to NTR binding (green) are obtained by subtracting the initial layer height from following height measurements. Reproduced from Schoch, *et al.* [111].

Chapter 3

Conformational Characterization of Surface-Tethered FG Domains

3.1 Introduction

Numerous studies about the molecular composition of NPCs show that the central channel wall provides anchoring points for a variety of multiple FG repeat containing proteins (FG Nups) [39, 67]. NPC transport mechanism is based on the interaction between soluble nuclear transport receptors (NTRs) and the FG repeat rich domains of FG Nups (FG domains) [42, 68, 70]. To understand nucleocytoplasmic transport in detail, knowledge about the conformational organization of FG Nups is essential. FG domains were shown to be intrinsically disordered at physiological conditions [119]. Because of their lack of secondary structure, it remains a challenge to reveal their conformational organization within the NPC environment [20]. To address this problem, fragments of yeast FG domains were grafted on a solid support and their collective conformational properties were investigated by means of SPR.

3.2 Materials and Methods

Two Nsp1p FG domain fragments of different length (Nsp1p-5FF and Nsp1p-12FF) were chosen for this experiment (see Figure 3.1). Nsp1p is predominantly anchored to the central channel framework of the NPC with a copy number of 32 [62, 74]. Both proteins have their N- or C-terminal end modified with 2 additional Cysteines. This allows to tether these proteins to a gold surface via gold-sulfur interactions forming a semi-covalent bond [147]. Because gold is not able to form stable bonds between other amino acid residues, surface tethered FG domains share the same overall orientation (i.e., N-terminal end attached to the surface and a freely moving C-terminus). This type of oriented surface grafting allows to create conditions which closely resemble the NPC transport channel interior, i.e., FG Nups are densely anchored to a surface while exposing an intrinsically disordered domain. For the determination of the overall conformational organization of surface grafted FG domains, the average layer height was measured at various grafting distances using SPR with non-interacting BSA molecules.

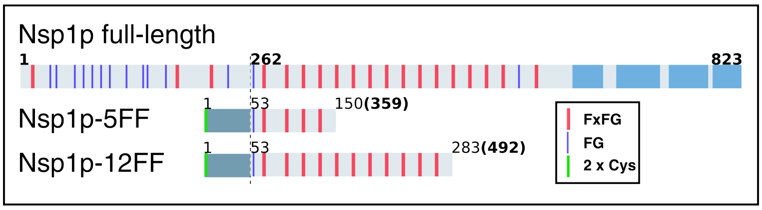

FIGURE 3.1: Both yeast FG domain fragments used in this study, Nsp1p-5FF and Nsp1p-12FF, contain regularly spaced FSFG repeats shown in red. FG repeats are depicted in blue. The linker regions between FG motifs have a length of typically 15 residues. Residue numbers in bold correspond to full-length Nsp1p. The fragments each contain a 52-residue 2xCys-/6xHis-/S-tag at their N-termini, shown in dark blue. The structured C-terminal domains of the full-length protein are depicted in light blue.

3.2.1 Preparation of SPR Gold Sensor Surfaces

SPR gold sensor surfaces (Biacore SIA Kit,GE Healthcare) were stored under low-pressure Argon atmosphere. Before they were used, a step-wise cleaning procedure made sure that the surface were of high quality without any contaminants. First, the sensors were immersed in Aceton (≥99.8%, Merck Millipore) and were subsequently sonicated for 15 min (35kHz/160W, Sonorex RK100, Bandelin Electronics, Berlin). This procedure was repeated with Isopropanol (≥99.8%, Merck Millipore) and Ethanol (≥99.8%, Fluka Analytical, Sigma Aldrich). At the end of the third sonication step, the sensors were carefully dried in an N_2 stream and put into an UV-ozone oven (Model 42A-220; Jelight, USA) for 30 min. In a last step, the sensors were again immersed in Ethanol and sonicated for 15 min. After cleaning, N_2 dried gold sensors were immediately mounted into the SPR system, following manufacturers guidelines.

3.2.2 Preparation and Immobilization of FG Domains

Nsp1p fragments were used immediately after thawing because they were already stored in PBS buffer. Solution trapped gas forms small bubbles which results in disadvantageous SPR signal changes. To prevent this, the protein solutions were centrifuged for 15 min at 16000 x g and room-temperature (RT) using a table-top centrifuge (Eppendorf). Running buffer (PBS) for the SPR experiment (Biacore T100, GE Healthcare) was filtered through a 0.22 µm membrane ("rapid"-filtermax, Techno Plastic Products AG) and degased for 1 h at RT. 1 mM PUT was diluted 1:10 in PBS from a 10 mM stock solution of PUT in ≥99.8% Ethanol. 1% (w/v) BSA (≥99.8%, Sigma Aldrich) was dissolved in PBS while gently stirring for at least 15 min. 0.2 M NaOH in PBS (pH ∼13) was filtered using a 200 nm filter (Filtropur S, Sarstedt). BSA, PUT and NaOH solutions were degased using a table-top centrifuge at 16000 x g and RT. Prior to the start of the protein injection sequence, the liquid handling system of the SPR machine was flushed with filtered and degased running buffer. The following immobilization procedure was applied on the SPR machine:

Cycle 0: Equilibration of the system with running buffer (PBS) at 25°C.

Cycle 1: Immobilization of the FG domains (e.g. Nsp1p-5FF) in flow-cells (FCs) 3 and 4.

Cycle 2: Passivation of FCs 1 and 2 with 1 mM PUT.

Cycle 3: A single short PUT injection in all four FCs to ensure that no gold is exposed.

Cycle 4: Injection of 0.2 M NaOH to remove all non-covalently bound molecules in all four FCs.

Cycle 5: Five subsequent injections of 1% (w/v) BSA in PBS for stabilization purpose followed by three injections of BSA to determine the layer height of the immobilized proteins.

Different FG domain grafting densities were achieved by varying the contact time and FG domain bulk concentration in cycle 1. The detailed immobilization procedure and subsequent height measurement are described in Figure 3.2.

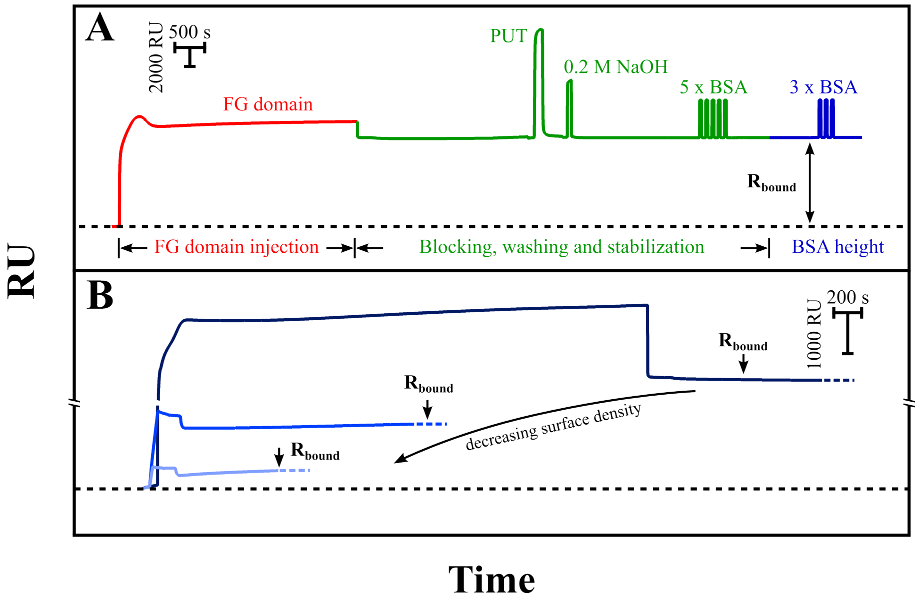

FIGURE 3.2: Immobilization procedure of FG domains. **(A)** After FG domain injection, the remaining exposed surface was blocked with PUT. The FG domain layer height was measured using BSA after subsequent washing and stabilization (see Section 2.4.7). To calculate a grafting distance, the SPR shift, R_{bound}, was determined as described in Section 2.4.5. **(B)** FG domain immobilization at different concentrations and injection times. Low concentrations gave smaller SPR responses (higher grafting distance).

3.2.3 Evaluation of Grafting Distance and Layer Height

The grafting distance and layer height were calculated as described in Chapter 2. Briefly, after FG domain injection, subsequent blocking with PUT and washing with

NaOH, the immobilized amount of FG domains was determined by the shift in SPR response (R_{bound}; Figure 3.2A). This was used to calculate the grafting distance, g (Section 2.4.5). Here, the used conversion of 1300 RU = 1 ng/mm^2 [123] relates the SPR shift with the surface adsorbed mass. R_{bound} was measured immediately before the triple injection of BSA which was used to determine the layer height (Section 2.4.7). This allows to directly relate the layer height with grafting distance as they are measured almost simultaneously.

3.3 FG Domains Form a Brush-Like Layer as a Function of Grafting Distance

FG domain grafting distances of ~2.5 – 25 nm could be achieved by varying protein concentration and contact time for immobilization. The typical grafting distance determined for 1mM PUT was measured to be ~0.5 nm. Figure 3.3 shows individual BSA injections on either FG domain functionalized or PUT passivated gold surfaces. After a single BSA injection, the SPR response quickly reaches the baseline again. This indicates, that innate non-interacting BSA molecules neither bind FG domains nor PUT, which is an important prerequisite for reliable height measurements [123].

The obtained results in Figure 3.4 show that for a decrease in the distance between neighbouring FG domains, the layer height shows a steep increase beyond a certain grafting distance. For convenience, the analysis considers two regimes based on the grafting distance: 1), close-packed, where $g < r_h$; and 2), sparse, where $g > r_h$. Here

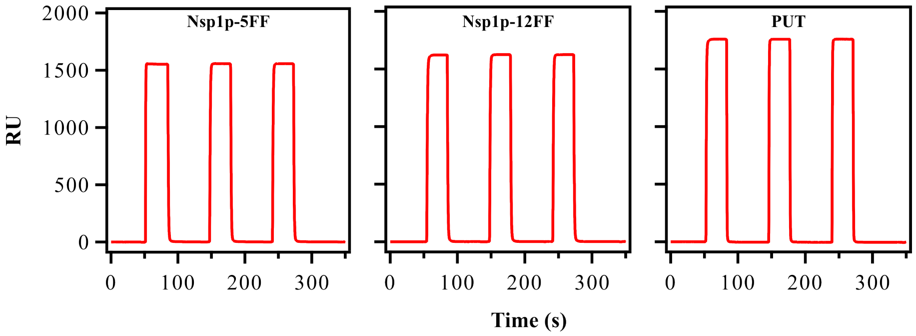

FIGURE 3.3: 1% (w/v) BSA injections on FG domain functionalized or PUT passivated surfaces. The SPR signal returns to baseline after injection on all different molecules grafted on the surface. This is an important prerequisite for reliable height measurements [123].

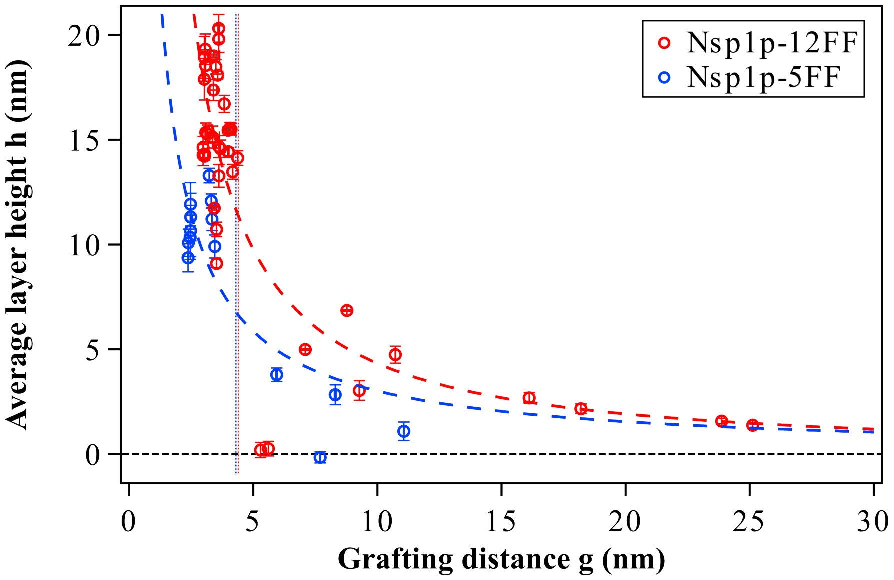

FIGURE 3.4: FG domain layer height, h, as a function of grafting distance, g, as obtained for FG domain fragments Nsp1p-5FF and Nsp1p-12FF. Color-coded dashed vertical lines correspond to the measured hydrodynamic radii (r_h) of the FG domains. Flory-Huggins fits (Equation 3.1) predict polyelectrolyte brush behavior (dashed lines).

r_h is the hydrodynamic radius of the FG domains as determined in in Section 2.2.2.

The scaling behavior of disordered polyelectrolytes at high surface densities can be described by Flory-Huggins and exclusion theory [148]:

$$h = A\left(\frac{1}{g^2}\right)^n \tag{3.1}$$

where h is the height of the polyelectrolyte layer with a grafting distance g. A and n are fitting parameters. The dashed lines in Figure 3.4 represent an adequate fit of the obtained data to Equation 3.1. Therefore, close-packing of FG domains results in molecular brush formation, consistent with the scaling behavior of intrinsically disordered proteins. By definition, surface-tethered polymeric chains tend to stretch away from their anchoring sites due to lateral crowding when $g < 2\,r_h$ as depicted in Figure 3.5 [107]. Nevertheless, this does not exclude the existence of intra- and inter FG domain interactions, which depend on the intrinsic physicochemical properties of each proteinaceous polymer (e.g., hydrophobicity and charge distribution; see Table 3.1).

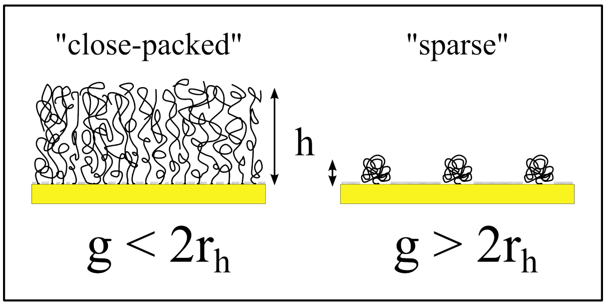

FIGURE 3.5: Cartoon of a "molecular brush" for $g < 2r_h$ ("close-packed") and "mushroom" for $g > 2r_h$ ("sparse") grafting.

Protein	**Net charge**	**% charged residues**^{a}	**Sub-fragment, residues**	**Charged/ Hydrophobic**	**% length FG domain**	**Conformation**^{b}
Nsp1p-5FF (150 aa) (pI = 8.51)	+3	27.6	262 – 359	1.08	16	repulsive
Nsp1p-12FF (283 aa) (pI = 8.75)	+5	32.5	262 – 492	1.27	38	repulsive

[a] Fraction of charged residues (i.e., R, K, D, E) at pH 7.2.

[b] Fragments are considered repulsive if the ratio of charged and hydrophobic residues is $\gg 0.5$.

TABLE 3.1: Intrinsic properties of FG domains used in this work.

For Nsp1p-5FF, the maximum layer height measured for a grafting distance $g < 4.5$ nm is ~14 nm, which is smaller than ~20 nm obtained for Nsp1p-12FF at similar density. This is consistent with their difference in number of residues. Table 3.2 summarises the measured layer height properties compared with the hydrodynamic radius and number of residues for both proteins. The results presented here are in agreement with previous experiments on close-packed vertebrate FxFG domains that report molecular brush-formation [110, 111].

Protein	Residues	r_h (nm)	g^a (nm)	h_{max} (nm)	ρ_{FG} (FG/ nm^3)
Nsp1p-5FF	150	4.4 ± 1.2	< 4	14	0.08 ± 0.01
Nsp1p-12FF	283	4.3 ± 1.3	< 4.5	20	0.08 ± 0.02

[a] Denotes the highest grafting distance where FG domain brushes were still observed.

TABLE 3.2: Hydrodynamic radius r_h, typical grafting distance g, maximum layer height h_{max} and FG volume density ρ_{FG} of surface-grafted Nsp1p-5FF and Nsp1p-12FF.

An average FG repeat volume density, ρ_{FG}, can be calculated using the measured grafting distance, g, and average layer height, h. Here, the FG volume density is defined as

$$\rho_{FG} = \frac{\#FG}{g^2 h} \tag{3.2}$$

where #FG is the total number of FG repeats of a single FG domain (i.e, 5 for Nsp1p-5FF and 12 for Nsp1p-12FF). Equation 3.2 assumes that the FG repeats are evenly distributed in the layer. FG volume densities are listed in Table 3.2.

The surface layers of Nsp1p-5FF and Nsp1p-12FF exhibit the same FG repeat volume density of 0.08 FGs/nm^3, which is equivalent to a FG repeat concentration of ∼130 mM inside the layer. These FG repeat densities are in agreement with the estimate of 0.08 FGs/nm^3 within the transport channel of yeast NPCs, that contain about 3500 FG repeats per NPC [149]. Similar FG repeat densities were reported for full-length Nsp1p FG domain brushes using QCM [150] as well as for macroscopic, *in vitro*-assembled FG domain hydrogels [100].

3.4 Discussion

An estimation of the anchoring distance between individual FG Nups in the NPC can be made using the dimensions of yeast NPCs derived by analysis of large proteomic datasets [74]. Accordingly, yeast NPCs resemble an hourglass shape with a typical peripheral diameter of ∼98 nm, a central diameter of ∼38 nm and ∼37 nm in height. Using these dimensions the NPC channel surface exposes an area of about 15000 nm^2. Based on their copy numbers, an estimated 200 – 350 FG Nups are filling the channel volume and therefore have to be anchored at the surface [63]. This results in an average grafting distance of 6.5 – 8.7 nm. When compared to the average hydrodynamic radius of FG domains of ∼6 nm [63], the criteria for brush formation ($g < 2\ r_h$) is fulfilled. Therefore, the FG domains overlapping exclusion volume cause them to stretch away from their anchoring point towards the central channel. By definition, the extended FG domains are now in a polymer-brush conformation [107]. In real NPCs however, distances between anchoring points are probably much smaller because the FG domain anchoring sites are not homogeneously distributed but rather concentrated at different regions.

The results presented here, demonstrate that close-packing of surface-grafted Nsp1p FG domains leads to the formation molecular brushes. This is in agreement with polymer-brush theory [107, 148] and earlier work on vertebrate FG Nups [36, 71, 110, 111]. A critical parameter identified here for brush-formation is grafting distance. For $g \gg r_h$, the measured layer heights do not resemble a brush-like layer but rather single chains which adopt "mushroom"-like conformations on the surface (Figure 3.5). Once a brush is formed, the average layer height increases as the grafting distance decreases. On planar gold surfaces, FG brushes occur at packing densities substantially lower than those present within NPC transport channels. However, it is unclear how the effect of confinement within a cylindrical geometry will influence the observed effects.

Closely anchored FG domains in the NPC interior display collective functional characteristics *in vivo* [151] which are in contrast to the in-solution properties of non-grafted FG domains. The data presented here supports the notion, that surface tethering and its implications on FG domain organization is an essential factor of NPC functionality [63]. It suggests that FG domains in brush-like conformation compose a cloud-like steric barrier in the NPC channel which is able to repel non-specific molecules [36, 71]. Figure 3.6 models an FG Nup crowded NPC which forms a barrier against non-specific molecules. Nevertheless, this model does not include any NTRs and therefore, may represent a "ground-state" of the FG domain barrier, if for instance, NTRs could be completely removed from the NPC.

In addition to the polymer-brush configuration, other models predict a different structural organization of FG domains. An model first proposed by Ribbeck and Görlich suggests that FG domains could form a sieve-like meshwork within the NPC [9]. As they stated, the driving force of such a self-assembly could be based on hydrophobic interactions between neighboring FG repeats. Further, it was shown that *in vitro* cross-linked FG-/FxFG (Nsp1p) and GLFG domains indeed can form macroscopic hydrogels [98]. It is not clear, however, how hydrogel formation can take place *in vivo* based on the requirements for gelation *in vitro* [98, 100].

Because of their intrinsic disordered nature, *in vivo* studies of FG domain organization within the NPC remains a challenge. Here, to investigate close-packed FG domains, they were grafted on a solid support and their conformation was observed by SPR. The obtained results show that

1. close-packed Nsp1p forms a molecular-brush on planar gold surfaces.
2. This brush exhibits a similar FG repeat volume density as estimated for the NPC transport channel *in vivo*, and
3. the grafting distance can be tuned to the same range as expected for FG Nups anchored in the NPC *in vivo*.

Therefore, this experimental setup has potential to act as a minimal model system which allows to study the interactions of soluble transport factors with densely grafted FG domains *in situ*.

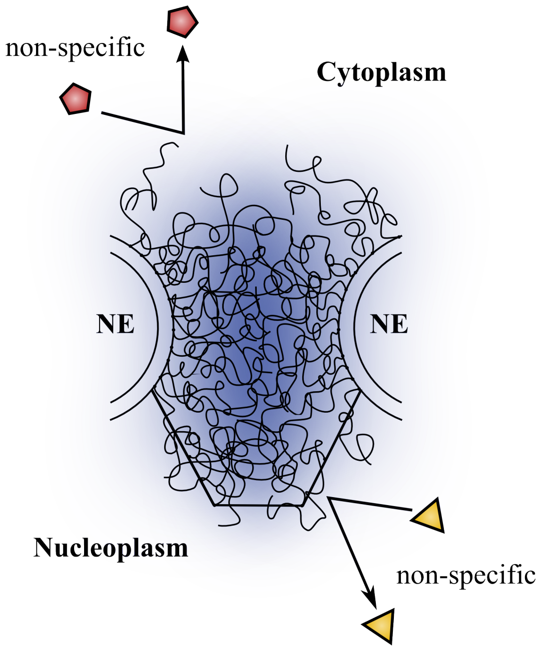

FIGURE 3.6: Model of FG domain organization within the NPC in its "ground-state" (i.e., no NTRs are in the pore). The FG Nups are anchored at the channel wall while disordered FG repeat rich domains stretch towards the central axis due to steric repulsion. This creates a barrier within the NPC channel which is able to repel non-specific molecules (red and yellow) [106]. NE: nuclear envelope.

Chapter 4

Karyopherin-centric Control of FG Nup Barrier Function

4.1 Introduction

FG Nups are considered to function as permeability barriers against non-specific cargoes based on their innate conformational flexibility and *in vitro* barrier forming properties that range from stimuli responsive molecular brushes [36, 71] to supramolecular hydrogel meshworks [98–101]. Based on these material characteristics classic FG-centric barrier models explain how non-specific macromolecules $\gtrsim$5 nm in diameter and lacking FG binding are rejected by the FG Nup barrier [6] (see Chapter 3). However, a satisfactory explanation as to how FG domain barriers can regulate selective Kap-cargo transport and reject non-specific cargoes at the same time remains unaccounted for. NPCs are crowded with ~100 Kapβ1 molecules at steady-state and Kap-FG binding involves highly multivalent interactions which are generally known to impact a strong avidity that leads to the formation of long-lived complexes [82]. This is paradoxical in the context of the NPC [152], because high submicromolar Kapβ1-FG domain binding affinities [83, 86, 153] predict slow off rates (given a diffusion-limited on rate) that contradict the rapid (∼5 ms) *in vivo* dwell time [154]. As this implies, Kap-FG binding ought to be sufficiently strong to ensure selectivity but also weak enough to promote fast translocation through the NPC. Nonetheless, an explanation as to how Kap-FG binding kinetics is balanced against the mechanistic control of the FG domain barrier is still lacking. Numerous Kapβ1 and NTF2 molecules interact with the FG Nups at steady state given their essential roles in maintaining import and Ran cycles, respectively [115, 155].

In Chapter 3 it was shown, that yeast Nsp1p exhibits characteristic behavior of intrinsically disordered proteins when densely grafted on a surface *in vitro*. Previous studies on surface grafted FxFG domains of Nup153 and Nup62 support this view [36, 110, 111]. These surface-tethered polypeptides start to stretch away from their anchoring site as a function of their grafting distance. At grafting distances smaller than their hydrodynamic diameter, these FG domains form molecular brushes [71, 111].

Here, SPR was used to resolve the multivalent interaction kinetics, equilibrium affinities and associated conformational changes in close-packed FG domain layers when binding to NTF2 or Kapβ1.

4.2 Materials and Methods

FG domain, BSA and PUT solutions were prepared as described in Chapter 3. Transport factors Kapβ1 and NTF2-W7A were dialysed against PBS using 3500 Da MWCO dialysis bags for 3 h at RT while stirring. Wild-type NTF2 was already stored in PBS and therefore was directly used after thawing. Absorbance at 280 nm was measured to determine the concentration of the proteins. Different concentration series of Kapβ1, NTF2 and NTF2-W7A were prepared by careful mixing with an appropriate amount of filtered (0.22 µm) PBS. The dilution series of NTF2 and NTF2-W7A were used in a concentration range between low nM up to ∼300 µM. For Kapβ1 the concentrations typically range from low nM up to ∼15 µM. All samples were degased using a table-top centrifuge at 16000 x g for 15 min at RT. The running buffer (PBS) was filtered through a 0.22 µm membrane and degased for 1 h at RT.

4.2.1 SPR Procedure

The SPR sensor surface was prepared and functionalized as described in Chapter 3. Briefly, FG domains were tethered in flow-cells (FCs) 3 and 4 while FCs 1 and 2 were passivated with PUT. All FCs were further blocked with PUT and washed with 0.2 M NaOH. After FG domain immobilization and PUT passivation, BSA was used to measure the initial layer height, h_0, before injection of either Kapβ1, NTF2 or NTF2-W7A. The measurement temperature was kept constant at 25°C. The sample compartment was cooled to 4°C. After successful functionalization of the SPR sensor surfaces (i.e., FCs 1 – 4), nuclear transport receptors (analytes) were simultaneously injected into all FCs in increasing concentration while the SPR signal change was constantly monitored with an acquisition rate of 10 Hz (Figure 4.1). A typical injection *i* consists of an association phase, were the surface is constantly in contact with a fixed concentration of analyte (e.g. Kapβ1 or NTF2). In all cases, SPR response levels at equilibrium response ($R_{eq,i}$) within 600 s of association. Subsequent injection of running buffer (PBS) starts the dissociation phase of bound analytes. The remaining fraction of bound analytes $R_{bound,i}$ was typically determined after 480 s of dissociation (i.e., analytes with $k_{off} > 1.5 \times 10^{-3}$ s^{-1} are completely washed from the surface). This is immediately followed by a triple injection of BSA to measure FG domain brush conformational changes induced by analyte binding. After the last NTR injection and subsequent BSA height measurement, the surfaces were regenerated with two short 0.2 M NaOH injections.

4.2.2 Data Export and Analysis

Raw data was extracted from the SPR manufacturers software (Biacore T100 Control Software, Version 2.0.2, GE Healthcare Bio-Sciences AB, Uppsala, Sweden) and prepared for further analysis. BSA height analysis as well as equilibrium and kinetic analysis was done in a semi-automated way using Igor Pro (WaveMetrics, Inc.; Version 6.35) and Matlab (MATLAB and Statistics Toolbox Release 2013b, The MathWorks, Inc., Natick, Massachusetts, United States).

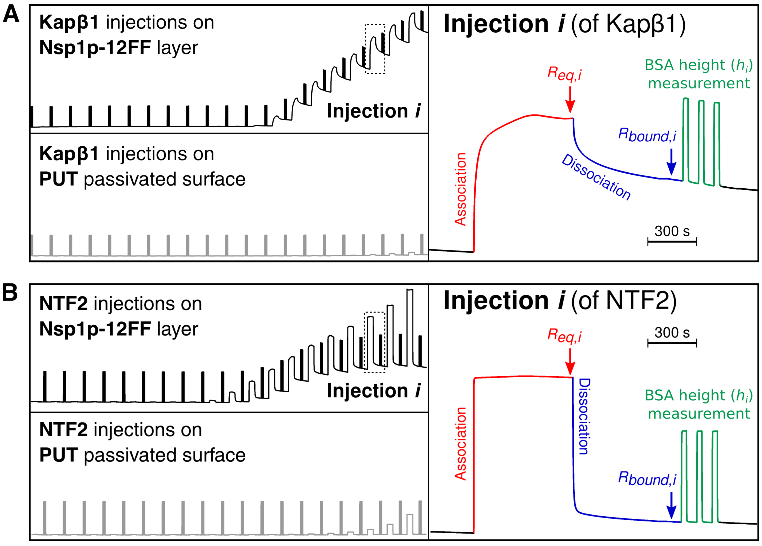

FIGURE 4.1: Kapβ1 **(A)** or NTF2/W7A-NTF2 **(B)** were injected on FG domain functionalized and PUT passivated reference surfaces (left top and bottom, respectively). A typical injection of analyte consisted of an association (red) and dissociation (blue) phase followed by BSA injections (green). $R_{eq,i}$ corresponds to the position where the SPR equilibrium binding response for analyte bulk concentration c_i was measured in respect to the baseline (i.e., response at $t = 0$ s). $R_{bound,i}$ represents the SPR response for bound analyte after 480 s of dissociation ($c_i = 0$). Three consecutive BSA injections were used to measure the average layer height at layer occupancy $R_{bound,i}$. The BSA signal (green) returns to baseline indicating a lack of binding Nsp1p FG-domains, which is a prerequisite for reliable height measurements.

4.3 NTR Binding to Surface Tethered FG Domains

4.3.1 FG Domain Layer Response upon NTR Binding

To investigate how different NTRs bind FG domains, the binding of Kapβ1 and NTF2 to Nsp1p FG domains was investigated. In addition, an NTF2 mutant (NTF2-W7A) was used as a control. In this mutant, the primary physiological interaction between NTF2 and FG repeats is impaired [68] (see Figure 1.8). The dependence of FG domain layer height on NTR binding was monitored by BSA injections that follow increasing titrates of Kapβ1, NTF2 or NTF2-W7A. The layer height was measured after a dissociation phase of 480 s and is related to the material bound given by $R_{\mathrm{bound,i}}$ (see Figure 4.1). Therefore, the BSA signal measured for $R_{\mathrm{bound,i}}$ generally underestimates the height at equilibrium binding $R_{\mathrm{eq,i}}$.

4.3.1.1 Close-Packed FG Domain Layer Response upon Binding of Kapβ1

Subsequent changes in the layer height of close-packed Nsp1p-12FF due to Kapβ1 binding was monitored. For this experiment, 20 Kapβ1 concentrations were prepared for titration by successively diluting a stock solution of Kapβ1 of 10 – 12 µM. Accordingly, the lowest applied Kapβ1 concentration was ∼10 pM.

Figure 4.2 summarizes the obtained results for Kapβ1 binding Nsp1p-12FF brushes. The results are described in four ways. First, the relative layer height, h_i/h_0, where h_0 stands for the initial layer height, is shown as a function of injected Kapβ1 bulk concentration (Figure 4.2A). Second, h_i/h_0 is shown as a function of surface density of bound Kapβ1 ($\rho_{\mathrm{Kap\beta1}}$), which is related to the estimated number of bound Kapβ1 layers (Figure 4.2B). Third, the relative layer height is shown as a function of an average quasi stoichiometry, given as bound Kapβ1 mass per bound FG domain mass projected onto a unit area (Figure 4.2C; see Section 2.4.6). And fourth, the change in the total protein mass density $\Delta\nu_{\mathrm{total}}$ as a function of relative layer height change $\Delta h_i/h_0$, where $\Delta h_i = h_i - h_0$ (Figure 4.2D). The total volume density includes both, FG domain and Kapβ1 mass, which occupy a volume defined by the layer height.

Based on the characterization of vertebrate FG domains binding Kapβ1 in Kapinos, et al. [110], brush response can be categorized into three different conformational responses: compaction (I), where $\Delta\nu_{\mathrm{total}}$ increases while $\Delta h_i/h_0$ decreases.

This describes a collapse of the layer during Kapβ1 binding. Compact extension (II) is characterized by an increasing $\Delta\nu_{\text{total}}$ and $\Delta h_i/h_0$. The layer responds in an extension, but it cannot compensate for the gain in mass due to successive Kapβ1 binding, and therefore the overall mass volume density increases. Porous extension (III) is defined by a decrease in $\Delta\nu_{\text{total}}$, while $\Delta h_i/h_0$ increases.

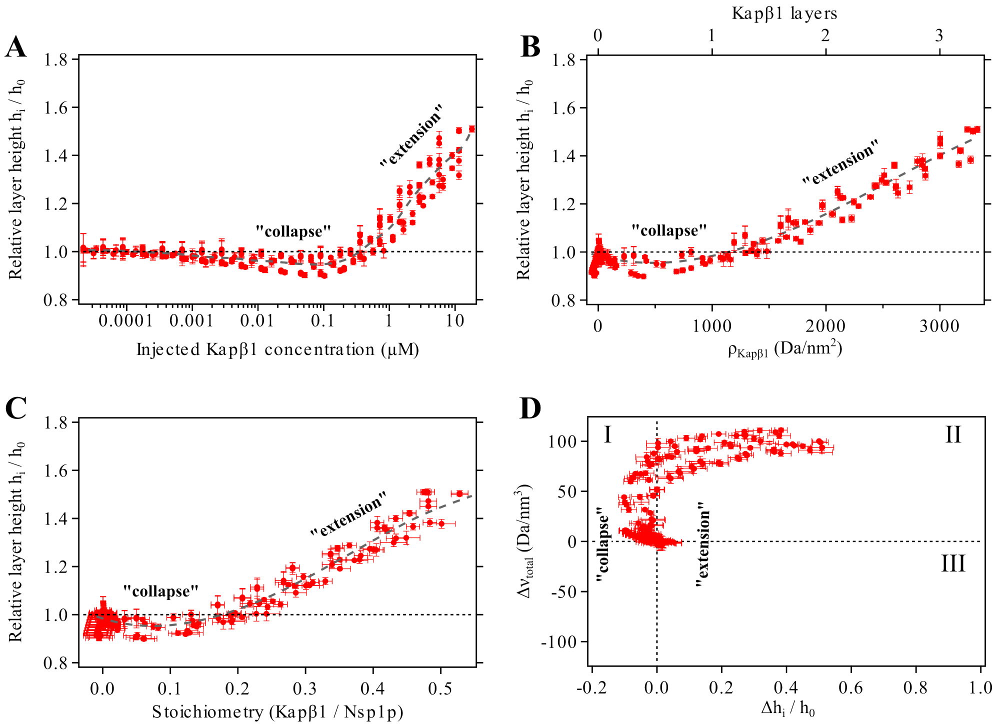

FIGURE 4.2: Non-monotonic response of Nsp1p-12FF FG domains to Kapβ1 binding. **(A)** The relative layer height, h_i/h_0, as a function of the bulk concentration of injected Kapβ1. Up to 50% layer-extension upon binding Kapβ1 was observed. **(B)** More than 3 layers of Kapβ1 occupy the Nsp1p FG-domain layer at ~15 µM Kapβ1 bulk concentration. 1 layer of Kapβ1 corresponds to a surface density of $\rho_{\text{Kap}\beta 1} = 1000\text{Da/nm}^2$. **(C)** A stoichiometric ratio describing the fraction of Kapβ1 mass coverage per Nsp1p mass coverage on a unit area. I.e., at highest concentration were the ratio ~0.5, the total mass of five Kapβ1 molecules is found on the same area covering the mass of 10 FG domains. **(D)** Corresponding changes in total protein density ($\rho_{\text{Kap}\beta 1}$ and FG domains; $\Delta\nu_{\text{total}}$) plotted as a function of the relative layer extension, $\Delta h_i/h_0$. The three characteristic responses are compaction (I), compact extension (II), and porous extension (III). A sliding average for **A**,**B** and **C** is shown as grey dashed line. Error bars are ±SD.

On close-packed Nsp1p-12FF, brush collapse was observed below 100 nM Kapβ1, followed by a layer extension, reaching about 150% of the initial height at the highest Kapβ1 occupancy. Thus, a Kapβ1-saturated layer of Nsp1p-12FF had a final height of 25 – 30 nm. The obtained height at saturation indicated that the Nsp1p brush was fully occupied by approximately 3 Kapβ1 layers (see Section 2.4.5) based on the ~10 nm hydrodynamic diameter of Kapβ1 and a bound surface density, $\rho_{\text{Kap}\beta 1}$, of 3330 Da/nm^2. This was comparable to how Kapβ1 binds FxFG domains of Nup214, Nup62 and Nup153 [110]. These proteins generally show a non-monotonic layer height response, which is represented by a early layer collapse at low Kapβ1 concentrations, followed by a recovery phase, where the initial height was reached again at low µM Kapβ1 concentrations (e.g., 1 µM for Nsp1p-12FF). For higher occupancy, the layer exhibits compact extension. Recalling that 480 s of dissociation time had elapsed before each height measurement, it was striking that the layer remained in an extended conformation with a high occupation of Kapβ1. Interestingly, the quasi stoichiometric ratio reveals an excess of FG domains even at highest applied Kapβ1 bulk concentrations, where Kapβ1/Nsp1p-12FF is about 0.5. Given the low grafting distance of close-packed Nsp1p-12FF and the high abundance of FG repeats, it is likely that several FG domains interact with a single Kapβ1 molecule and *vice versa*, a property inherent of intrinsically disordered proteins in protein-protein interaction networks [156].

4.3.1.2 Close-Packed FG Domain Layer Response upon Binding of NTF2 and NTF2-W7A

To compare the results obtained for Kapβ1 with other NTRs, the interaction of the RanGDP importer NTF2 with Nsp1p-12FF was investigated. To establish how NTF2 binds Nsp1p FG domains specifically, the binding of wild-type protein was compared with that of NTF2-W7A. Analogous to Kapβ1 FG domain interaction studies, the dependence of close-packed Nsp1p FG domain layer height on binding was monitored by BSA injections that follow increasing titrates of either wild-type or mutant NTF2. 20 consecutive NTF2 and NTF2-W7A concentrations were prepared as described before for Kapβ1. The maximum bulk concentration of NTF2 was ∼270 µM and ∼300 µM for NTF2-W7A, respectively.

Figure 4.3A shows that at low bulk concentrations of NTF2, any change in layer height is negligible. However, at approximately 1 µM of wild-type NTF2 in bulk solution, the layer height starts to decrease and reaches ∼85% of its initial value at the highest NTF2 concentration of ∼270 µM. Such a pronounced reduction was not observed with the W7A mutant. At physiological relevant concentrations (∼20 µM) [157], the relative change in the remaining layer height after 480 s of dissociation is about ∼10% (2 nm) for NTF2 binding Nsp1p-12FF, whereas the mutant does not produce any significant change. Previous studies showed that mutation of Trp7 in NTF2 to Ala reduces the affinity towards FG domains of Nsp1p substantially and impairs the nuclear import of NTF2 and RanGDP [68, 70]. Indeed, no change in layer height was observed even at high bulk concentrations of NTF2-W7A (up to ∼300 µM). Whereas up to 3000 RU of wild-type NTF2 was bound (corresponding to ∼ 1 layer, where 1 layer of NTF2 = 1340 Da/nm^2), NTF2-W7A only bound up to 100 Da/nm^2 or an equivalent of about 0.05 layers at the highest injected bulk concentration (Figure 4.3B). This results provide direct evidence that the observed collapse is a function of NTF2 binding. To obtain an estimate of the number of NTF2 molecules bound per Nsp1p FG domain, these data are re-plotted in Figure 4.3C in terms of the average ratio between NTF2 and Nsp1p-12FF mass per unit area. Although NTF2 and the W7A mutant were present in very high concentrations, each Nsp1p-12FF fragment bound only up to ~0.4 NTF2 molecules after 480 s of dissociation (may change for higher loading). Interestingly, an onset of layer height reduction is already observed for less than 0.1 NTF2 per grafted Nsp1p-12FF fragment. However, although the stoichiometric ratios between Kapβ1 and Nsp1p-12FF are comparable with those obtained for NTF2 binding Nsp1p-12FF, the layer height response is opposite and shows extension rather than collapse.

4.3.2 Equilibrium Binding Analysis

SPR binding equilibrium analysis was performed on Kapβ1, NTF2 and NTF2-W7A interacting with close-packed Nsp1p FG domains. To do so, the SPR equilibrium binding response, $R_{eq,i}$, was measured at the end of every consecutive analyte injection as defined in Figure 4.1. Equilibrium dissociation constants (KDs) were obtained by Langmuir isotherm analysis (see Section 2.4.2).

Equilibrium analysis of Kapβ1 binding to Nsp1p FG domains was only possible with a two-component Langmuir isotherm. A high affinity species with a $KD_1 = 336 \pm 63$ nM represents tight Kapβ1 binding at high FG repeat density in close-packed Nsp1p FG domain layers whereas moderately binding species at $KD_2 = 5.61 \pm 1.98$ μM is consistent with reduced binding due to pre-occupancy of Kapβ1 and a limited access to FG repeats within the layer (Figure 4.4A). A clear reduction in binding

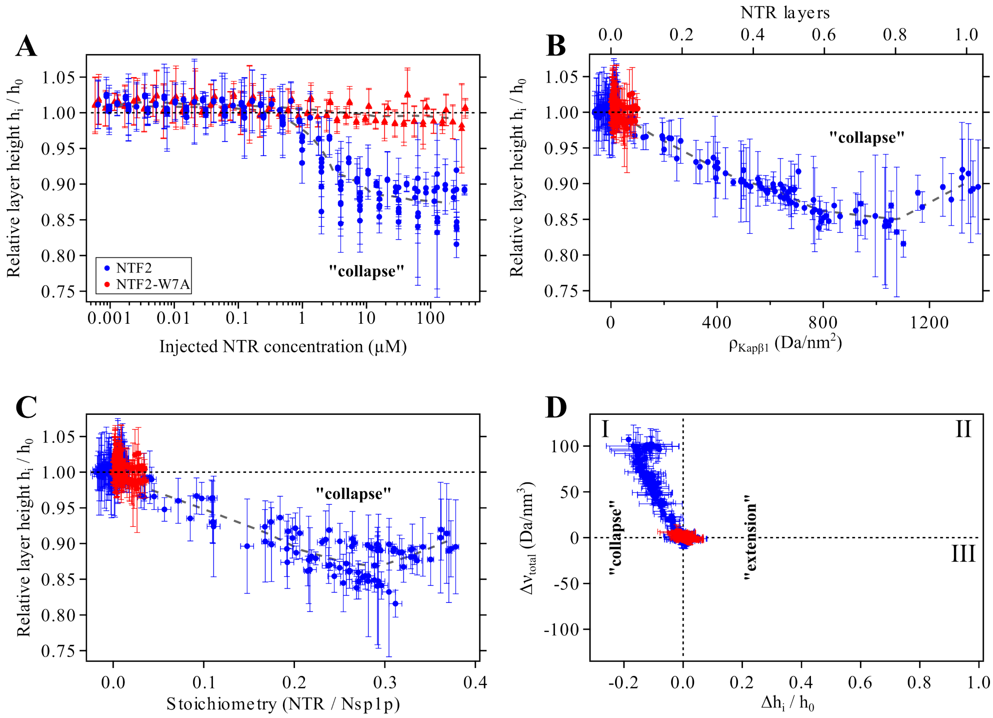

FIGURE 4.3: Conformational response of Nsp1p-12FF FG domains upon binding NTF2 and NTF2-W7A. **(A)** The relative layer height, h_i/h_0, as a function of the bulk concentration of injected NTF2/NTF2-W7A. NTF2 binding induces layer collapse of ~10% at physiological concentration (~20 μM)). In contrast, NTF2-W7A binding did not cause a layer collapse, even at highest injected concentration of ~300 μM). **(B)** About 1 layer of NTF2 is bound at highest injected concentration, were 1 layer of NTF2 corresponds to a surface density of $\rho_{NTF2} = 1340 \mathrm{Da/nm^2}$. NTF2-W7A bound only up to 100 Da/nm^2 (0.05 layers). **(C)** A stoichiometric ratio describing the fraction of NTF2 mass coverage per Nsp1p-12FF mass coverage on a unit area. I.e., at highest concentration at a the ratio of ~0.4, the total mass of four NTF2 molecules is found on the same area covering the mass of 10 FG domains. **(D)** Corresponding changes in total protein density ($\rho_{NTF2}/\rho_{NTF2-W7A}$ and FG domains; $\Delta\nu_{total}$) plotted as a function of the relative layer extension, $\Delta h_i/h_0$. The three characteristic responses are compaction (I),compact extension (II), and porous extension (III). A sliding average for **A**,**B** and **C** is shown as grey dashed line. Error bars correspond to ±SD.

of NTF2-W7A compared to wild-type NTF2 was measured (Figure 4.4B). Similar to Kapβ1, NTF2 binding could not properly be described by a single-component Langmuir isotherm of the equilibrium binding response $R_{eq,i}$ over the complete range of injected bulk concentrations. However, a two-component isotherm provides an appropriate fit, giving dissociation constants of $KD_1 = 2.1 \pm 0.5$ μM and $KD_2 = 114 \pm 23$ μM for wild-type binding and $KD_1 = 18.8 \pm 3.0$ μM and $KD_2 = 356 \pm 44$ μM for binding of NTF2-W7A. Being two orders of magnitude weaker, the second KD indicates that a non-negligible fraction of NTF2 binds to the Nsp1p FG domains much more weakly than the known primary physiological interaction [68, 157].

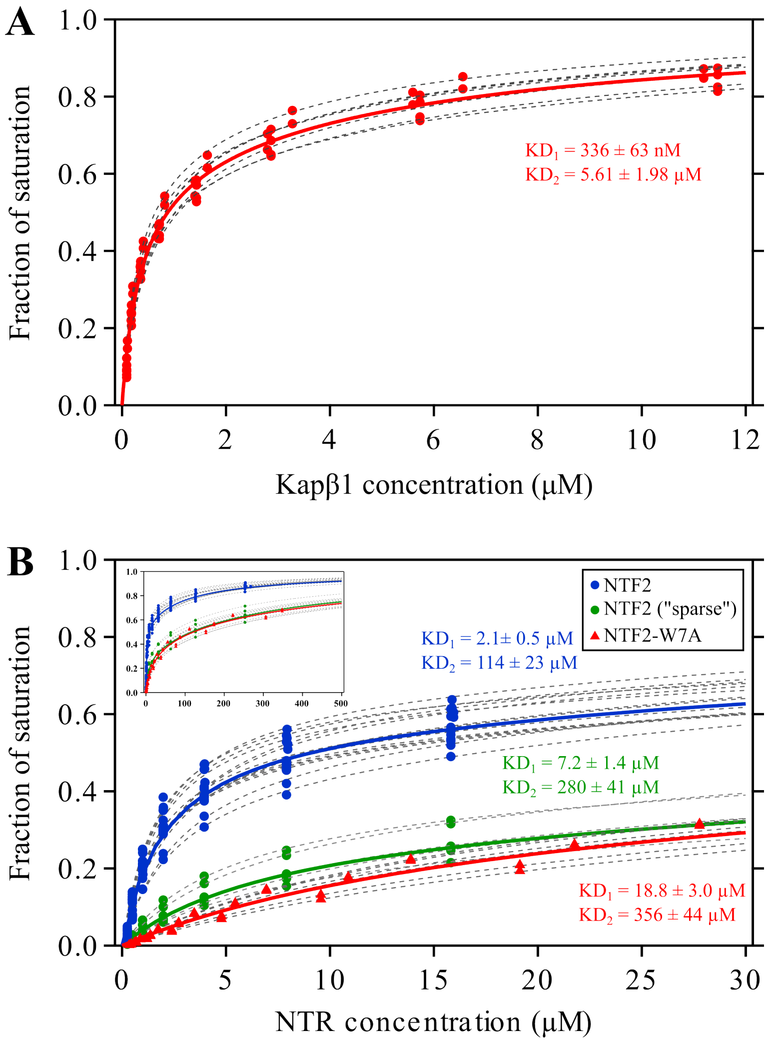

FIGURE 4.4: Equilibrium binding of Kapβ1 **(A)**, wild-type NTF2 and NTF2-W7A **(B)** to Nsp1p-12FF normalized by the maximum binding capacity (fraction of saturation) as a function of injected bulk concentration up to 30 μM (inset up to ~300 μM). NTF2 binding to sparse ($g_{NTF2} \gg r_{h,NTF2}$) Nsp1p-12FF is shown in **(B)**. Grey dashed lines represent individual two-component Langmuir isotherm fits. Solid lines represent the average isotherm for Kapβ1, NTF2 and NTF2-W7A, respectively.

In spite of KD$_1$ for mutant NTF2-W7A binding to Nsp1p-12FF being about an order of magnitude weaker than the corresponding value for the wild-type protein, the remaining low affinity species ($KD_2 = 356$ µM) indicates the existence of multiple and/or less specific binding spots of NTF2 to FG repeats that are consistent with NMR [80] and computational [78, 79] studies. For instance, electrostatic interactions between the positively charged Nsp1p-12FF (theoretical pI = 8.75) and negatively charged NTF2 (theoretical pI = 6.13) at pH 7.2 may attribute to species having such weak binding affinities.

Interestingly, the affinity of NTF2 binding to sparse Nsp1p-FF12 is reduced when compared to binding to brushes (Figure 4.4B; $KD_1 = 7.2 \pm 1.4$ µM; $KD_2 = 280 \pm 41$ µM). In the sparse regime, only a single FG Nup is able to bind to one or several NTF2 molecules. In order to saturate all binding pockets on NTF2, the FG Nup has to “wrap” around NTF2. This is unfavorable due to the loss in entropy. In the brush regime, several FG Nups can easily bind to a single NTF2 without losing much of their entropy. This could explain the difference in the obtained KDs.

Regardless, at least two KDs are needed to describe the equilibrium binding being consistent with the anticipated multivalent interactions between NTF2, NTF2-W7A and Kapβ1 and close-packed or sparse Nsp1p FG domains as summarized in Figure 4.5. Control experiments performed on shorter Nsp1p-5FF fragments resulted in dissociation constants for NTF2 binding to Nsp1p-5FF and Nsp1p-12FF being indistinguishable, which indicates that neither the number of FG repeats nor the additional FG-spacer regions in Nsp1p-12FF compared to Nsp1p-5FF influence the overall affinity (see Figure 4.5).

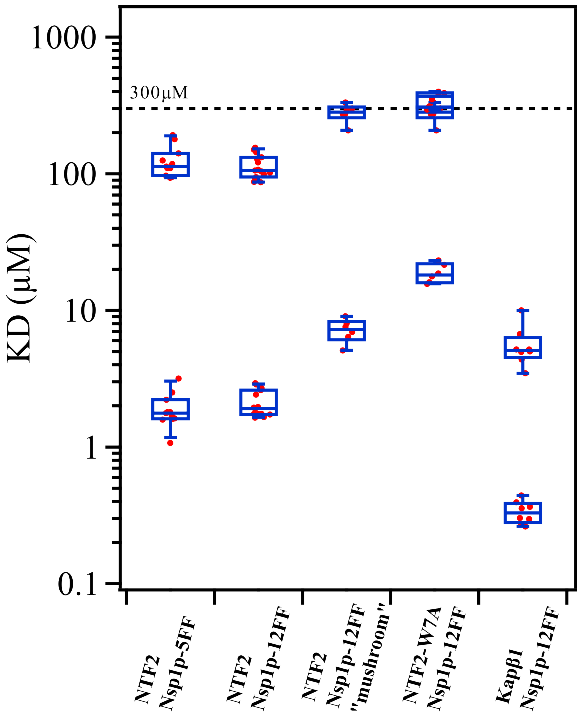

FIGURE 4.5: Overview of obtained equilibrium binding constants of NTF2, NTF2-W7A and Kapβ1 interacting with Nsp1p FG domain fragments. No significant difference is observed for NTF2 binding both Nsp1p fragments, Nsp1p-5FF and Nsp1p-12FF, respectively. Obtained KDs are shown in a boxplot representation where the box represents the first and third quartiles. The median is given by the band inside the box. Whiskers represent the 9th and the 91th percentile. Individual KDs are indicated as red dots.

4.3.3 Multivalent Kinetic Analysis

Although equilibrium binding analysis provides thermodynamic information (on the stability of the NTR-FG domain complex), the transition states between bound and unbound forms of NTRs depends on kinetics. However, this is not straightforward because the binding of Kapβ1 or NTF2 to FG domains involves multivalent interactions.

To obtain kinetic information, the SPR signal of each binding experiment was analyzed using the method of Svitel *et al.* [141, 158] to obtain a parsimonious distribution of association and dissociation constants (k_{on}, k_{off}) that describe the pseudo-first order kinetics of Kapβ1, NTF2 and NTF2-W7A binding Nsp1p FG domains. In general, this method circumvents difficulties associated with analyzing heterogeneous interfacial interactions that are often encountered in multivalent systems [81, 155, 159]. In the context of this study, NTR binding depends on the FG domain surface density and the number of NTR molecules already bound. Here, k_{on} describes how quickly a NTR molecule locates and binds to FG repeats within an FG domain layer, whereas k_{off} correlates to NTR-FG domain binding strength and stability. In context of nucleocytoplasmic transport, a high off-rate (low affinity) would be beneficial to achieve fast transport rates.

To avoid the necessity of modeling the interaction of every single possible FG binding site on the different NTRs (e.g., molecular dynamics simulations suggest 6 potential sites on NTF2 or 10 on Kapβ1 [77, 79]; Figure 1.8), this approach uses a simplified two-dimensional lattice of 10 x 10 nm^2 Kapβ1- and 5 x 5 nm^2 NTF2-"binding spots" describing the FG repeat containing surface based on the average size of a Kapβ1 molecule or NTF2-dimer with Stokes radius of 5 and 2.5 nm, respectively [9, 111].

4.3.3.1 Kapβ1 Binding Kinetics

The Kinetics of Kapβ1 binding to Nsp1p FG domains is modeled by

$$L + A_s \underset{k_{off,i}}{\overset{k_{on,i}}{\rightleftharpoons}} LA_1 + A_s \underset{k_{off,i}}{\overset{k_{on,i}}{\rightleftharpoons}} LA_2 + A_s \underset{k_{off,i}}{\overset{k_{on,i}}{\rightleftharpoons}} \cdots \underset{k_{off,i}}{\overset{k_{on,i}}{\rightleftharpoons}} LA_n \tag{4.1}$$

where L denotes the empty surface sites, A_s is the analyte concentration in solution, and LA_1 to LA_n correspond to surface sites where n represents the number of analytes that can bind per surface site. Here, $n = 3$ based on the measured number of layers Kapβ1. For $n > 1$, Equation 4.1 imposes a sequential binding constraint that mimics the multilayered Kapβ1-FG domain binding characteristics observed experimentally (Figure 4.2B).

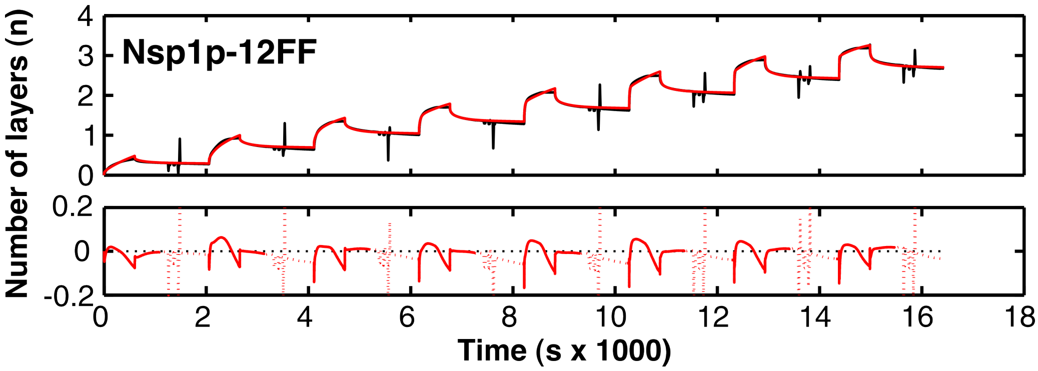

FIGURE 4.6: Kinetic analysis of Kapβ1-FG domain binding. Representative fit (red) to an SPR sensogram (black) for Kapβ1 binding to close-packed Nsp1p-12FF. NTR binding is converted into respective number of layers, n. The residual of the fit is included below the experimental sensogram. Note that fitting errors may arise from structural changes that occur in the FG-domain layer as NTR binding progresses (e.g., layer collapse or extension).

Fitting the SPR sensograms with this method (Figure 4.6), a distribution of k_{on} and k_{off} values is obtained for Kapβ1 binding Nsp1p-12FF (Figure 4.7A). At low Kapβ1 concentrations, a high avidity slow-phase (∗) commenced at $k_{on} = 1.2 \times 10^4$ $M^{-1}s^{-1}$, $k_{off} = 1.3 \times 10^{-5}$ s^{-1}, resulting from a long-lived half-life of $t_{1/2} \approx 15$ h (where $t_{1/2} = \ln(2)/k_{off}$). Increasing the concentration towards 10 μM Kapβ1 led to a steady reduction in k_{on} to ∼60 $M^{-1}s^{-1}$ (∘), giving rise to lower avidity interactions (increasing KD) that coincided with the emergence of a low avidity fast phase (▲) having a fast k_{on} ($\sim 1.6 \times 10^5$ $M^{-1}s^{-1}$) and a fast k_{off} (between 0.1 – 1.6 s^{-1}) where now $t_{1/2}$ = 430 ms – 7 s.

These results were consistent with Kapβ1-binding to human FG domains observed previously [110], and were indicative of an overall reduction in avidity resulting from: (i) a reduction of available FG-repeats, (ii) poor penetration due to Kapβ1 occupancy and crowding, (iii) a reduced mobility of flexible FG chains due to Kapβ1 binding [59], and (iv) steric repulsion due to FG chain extension. In this respect, the co-existence of both slow (low k_{off}) and fast phases (high k_{off}) at µM Kapβ1 concentrations indicated that the quantity and/or accessibility of FG repeats was reduced as Kapβ1 accumulated in the layer.

The distribution of k_{on} and k_{off} specifies a broad range of KD values. Except for the low KDs around ∼10 – 50 nM, the maxima in the distribution of the histograms on the top of each map correlate well with $KD_1 \sim 100 - 300$ nM from equilibrium analysis (Figure 4.7A; Figure 4.4A). In addition, distributions between 1 – 8 µM describe a low affinity fraction of Kapβ1 binding to FG domain layers and are in agreement with the second, low KD_2 from equilibrium analysis. Nevertheless, the observed high KD values have contributions from both slow and fast binding species with short or long half-lives, respectively. In kinetic terms, a high fraction of Kapβ1 interacting with an already saturated FG domain layer is in the fast phase (Figure 4.7B). This is because Kapβ1 can only bind a smaller number of free FG repeats (high

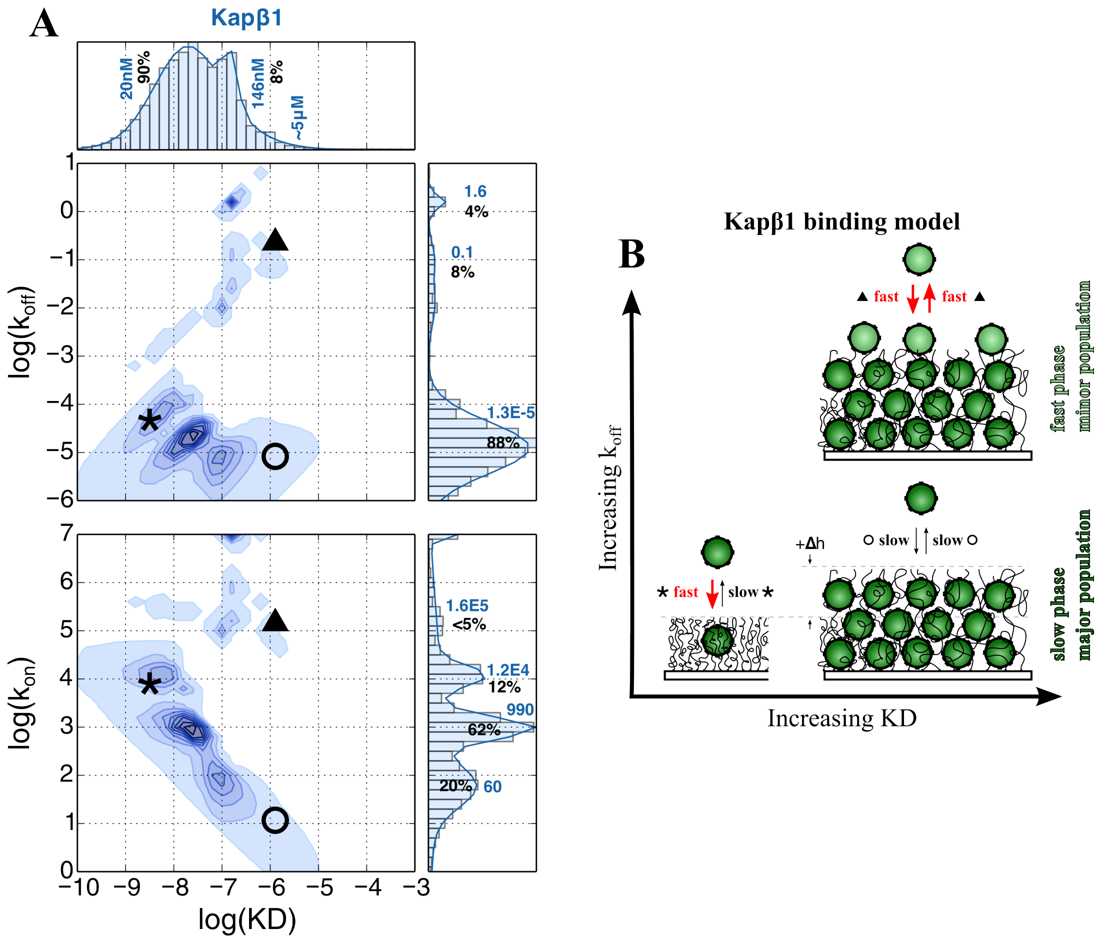

FIGURE 4.7: Kinetic analysis of Kapβ1 binding Nsp1p-12FF. **(A)** two-dimensional interaction maps of kinetic on- and off-rates (k_{on}, k_{off}) are shown in relation to equilibrium binding constant KD. The fractional abundance of different kinetic states is indicated by the color intensity and the sum over all values in a given axis is shown as accompanying histograms (top and right panels). Different kinetic species are labeled with $*$ ("high-affinity slow-phase"), ▲ ("mid-affinity fast-phase") and ∘ ("low-affinity fast-phase"). The fraction of each distribution in the histograms are given in percent of the total sum and their main values are depicted in bold, where values for k_{off} are s^{-1} and for k_{on} $M^{-1}s^{-1}$, respectively. **(B)** State diagrams separating slow (dark; low k_{off}) and fast (light; high k_{off}) kinetic phases of Kapβ1 binding. Moderate to fast k_{on} into a largely vacant FG-domain layer and slow k_{off} due to stable multivalent interactions results in high-affinity binding ($*$). Two low-affinity phases emerge due to FG-domain layer saturation, a fast phase, characterized by high (k_{off}, k_{on}) pairs due to limited binding at the layer periphery (▲), and a slow phase characterized by low (k_{off}, k_{on}) pairs due to slow penetration into a preoccupied layer (∘).

k_{off}) confined at the surface of the layer (high k_{on}). This leads to binding and unbinding with much higher attempt frequencies. The fraction of interactions that lead into the slow phase can be estimated from $k_{on}(slow)/k_{on}(fast)$ (i.e., $10/10^6$), which corresponds to 0.001% at high Kapβ1 concentrations. Nevertheless, this does not prevent the existence of a slow phase at highest Kapβ1 concentrations, nor that of a fast phase at low Kapβ1 concentrations. Simply, at high concentrations, the slow phase becomes less accessible due to hindered penetration into a saturated layer, which on the other hand enhances the fast phase. These findings are summarized in Figure 4.7B.

4.3.3.2 Multivalent NTF2 and NTF2-W7A Binding Kinetics

NTF2 and NTF2-W7A are multivalent entities with up to 6 putative FG repeat binding sites [79] (Figure 1.8). For the determination of binding kinetics, the same approach was used as described before for Kapβ1. With a Stokes radius of 2.5 nm [9], the average size of an NTF2 dimer is substantially lower than that of Kapβ1. Therefore, the NTF2-binding spot distribution was modeled by a 5 x 5 nm^2 lattice describing the FG repeat containing surface. NTF2 occupancy does not exceed ~1 layer at highest concentrations applied in this experiment (~10 x higher than physiologically relevant; Figure 4.3B). Therefore, the kinetic model is described by

$$L + D_s \underset{k_{off,i}}{\overset{k_{on,i}}{\rightleftharpoons}} LD_s \tag{4.2}$$

were L are the free binding sites, D_s is the NTF2 dimer concentration in solution and LD_s are binding sites occupied with dimeric NTF2 molecules.

Global multivalent kinetic analysis of NTF2 and NTF2-W7A binding Nsp1p-12FF is summarized in Figure 4.9 by a two-dimensional distribution of derived kinetic constants k_{on} and k_{off}. NTF2 binding is characterized by a broad spread of obtained KDs that spans over four orders of magnitude with distinct peaks at ~2 μM and ~100 μM and shoulders ranging into the nM and mM range, respectively.

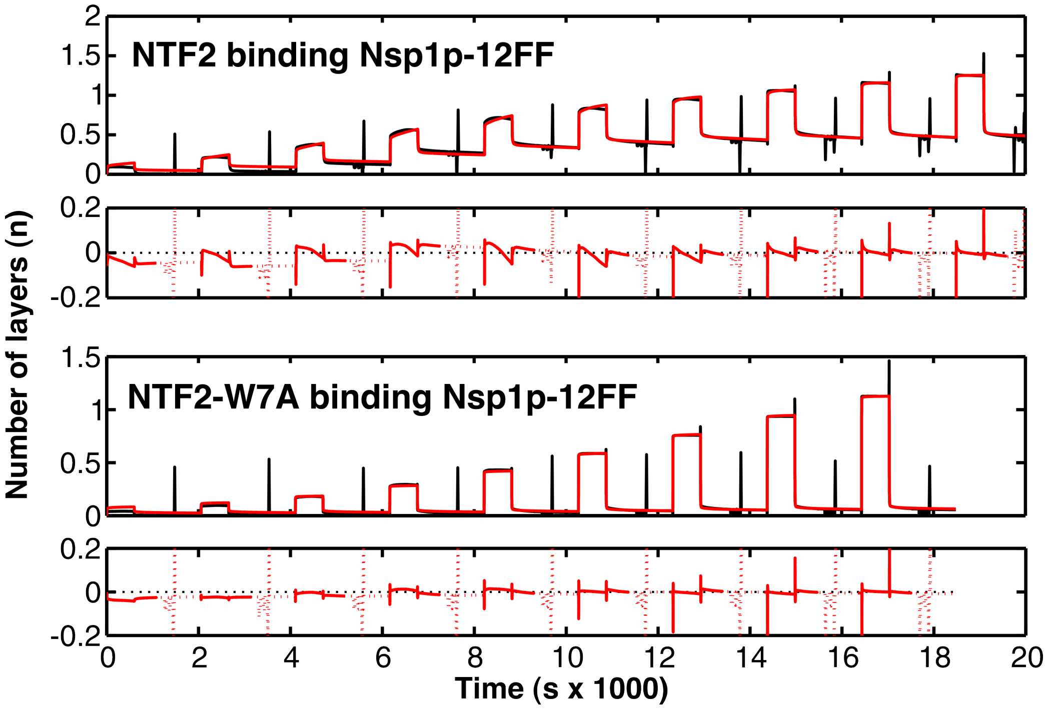

FIGURE 4.8: Kinetic analysis of NTF2/NTF2-W7A binding close-packed Nsp1p FG domains. Representative fits (red) to SPR sensograms (black) for NTF2/NTF2-W7A binding to close-packed Nsp1p-12FF. NTR binding is converted into respective number of layers, n. The residuals of the fits are included below the curves. Note that fitting errors may arise from structural changes that occur in the FG-domain layer as NTR binding progresses (e.g., layer collapse).

Overall, three distinctive kinetic species can be identified from the NTF2 binding data in Figure 4.9A: i) a "high-affinity slow-phase" (○) with low k_{on} (~500 $M^{-1}s^{-1}$) and low k_{off} ($\sim 3.5 \times 10^{-5}$ s^{-1}) resulting in a half-time of $t_{1/2} \approx 5.5$ h; ii) a "mid-affinity fast-phase" (▲) with high k_{on} ($\sim 10 \times 10^5$ $M^{-1}s^{-1}$) and high k_{off} (~ 1.7 s^{-1}) which equals a $t_{1/2}$ of 400 ms; and iii) a "low-affinity fast-phase" ($\ast$) consisting of a high but reduced k_{on} (~ 5100 $M^{-1}s^{-1}$) and a similar high k_{off} compared to the "mid-affinity fast-phase". Overall, these data indicate a bimodal distribution of k_{off} that is consistent with the presence of two major complexes with different stabilities (Figure 4.9B). Although high µM to mM affinities are rare for typical protein-protein interactions this has been proposed for Kaps binding individual FG cores [160]. Except for the low KD range around 100 – 200 nM, the obtained distribution of KD from multivalent binding kinetic analysis is in good agreement with the KDs obtained from equilibrium binding analysis (Figure 4.4B). The control experiment using NTF2-W7A showed a significant reduction of binding to Nsp1p FG domains. The mutation of Trp7 clearly results in the formation of only a single complex with fast k_{off} and substantially reduced binding that is underscored by the absence of a high-affinity slow-phase. Nevertheless, NTF2-W7A may still bind to FG domains via a number of other putative sites [79, 80] that give rise to binding affinities of around 16 µM and 300 µM, which are in good agreement with Langmuir isotherm analysis (Figure 4.4B). Overall, the NTF2-W7A data validates that the primary FG repeat binding site located around Trp7 is required to form a high-affinity slow-phase for wild-type NTF2 when binding close-packed Nsp1p FG domains and that this is accompanied with a reduction in layer height (Figure 4.3).

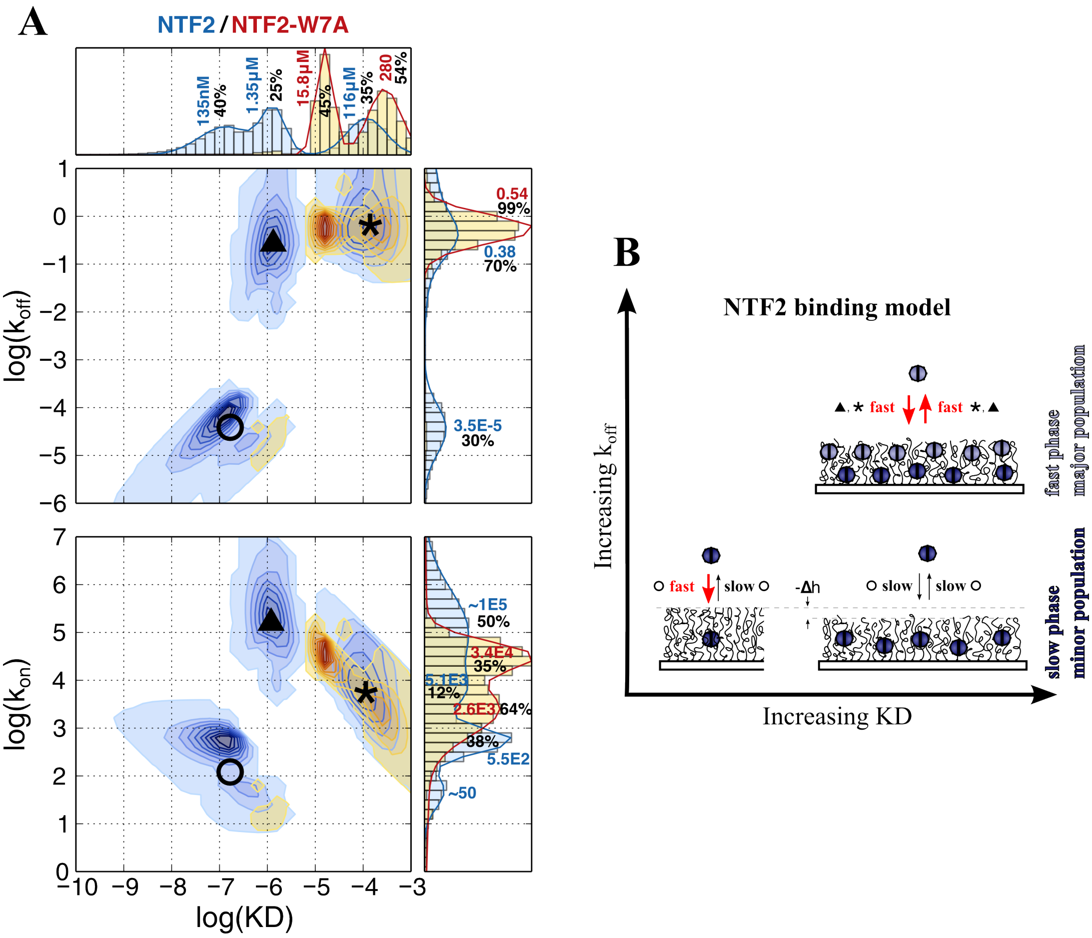

FIGURE 4.9: Kinetic analysis of NTF2/NTF2-W7A binding close-packed Nsp1p FG domains. **(A)** Two-dimensional interaction maps of kinetic on- and off-rates (k_{on}, k_{off}) for NTF2 (blue) and mutant (red) are shown with their derived equilibrium binding constant, KD. The fractional abundance of different kinetic states is indicated by the color intensity and the sum over all values in a given axis is shown as accompanying histograms (top and right panels). The fraction of each distribution in the histograms are given in percent of the total sum and their main values are depicted in bold. Values for k_{off} are s^{-1} and for k_{on} $M^{-1}s^{-1}$, respectively. Different kinetic species are labeled with ∘ ("high-avidity slow-phase"), ∗ ("mid-avidity fast-phase") and ▲ ("low-avidity fast-phase"). **(B)** State diagrams separating slow (dark; low k_{off}) and fast (light; high k_{off}) kinetic phases of NTF2 binding. Moderate to fast k_{on} into a largely vacant FG-domain layer and slow k_{off} due to stable multivalent interactions results in high-affinity binding (∘). At higher NTF2 concentrations, the binding is dominated by a fast-phase (∗, ▲) while the minor, slow-phase population (∘) remains constant.

4.4 Discussion

4.4.1 Close-packed FG domain response upon NTR binding

The results obtained on Nsp1p demonstrate that NTF2 and Kapβ1 bind FG domains very differently, although both transport factors seem to pass through NPCs simultaneously and with similar passage dwell times [96, 154]. The Nsp1p brush undergoes a collapse transition that correlates to an increase in the occupancy of bound NTF2. At physiological relevant concentrations (~20 μM), the relative change in the remaining layer height after 480 s of dissociation is about ~10% (2 nm) for NTF2 binding Nsp1p-12FF. At maximum injected concentration of ~250 μM NTF2, the extent of collapse is ~15% of the initial layer height with a bound content corresponding to effectively one monolayer of NTF2. Binding of NTF2-W7A did not induce a layer height change, even at high concentrations up to ~350 μM. This confirms, that the measured collapse for wild-type NTF2 and Kapβ1 binding is related to protein-FG domain interaction, whereas other effects such as osmotic pressure do not influence the measurement in the given sensitivity of the method. Opposite to the constant NTF2 dependend layer collapse, Kapβ1-binding induces a non-monotonic response in FxFG domains that is characterized by a collapse at low nM concentrations and subsequent layer extension at higher, more physiological Kapβ1 concentrations. The layer height of close-packed Nsp1p FG domains increases substantially with increasing occupancy up to ~3 and more Kapβ1 layers. In agreement with the results obtained here, densely grafted full-length FG domains of Nsp1p exhibit a layer height increase for increasing Kapβ1 occupancy [150]. Further, when incubated with low nM-range concentrations of Kapβ1, Lim, *et al.* observed a reversible collapse of densely grafted FxFG domains of Nup153 forming a molecular brush [36]. This trend was also observed for Nup62 when Kapβ1 is injected at low concentrations in the range of 10 – 100 nM [111].

In general, grafted polymers and the properties of polymer brushes are well-established. In physical terms, the polymer brush height is determined by the balance between the stretching entropy of the polymers (favors compaction) and excluded volume interaction between the polymers (favors extension) [161]. Transport factor binding disturbs the entropy-enthalpy balance and the brush responds by altering the arrangement of the FG domain chains that generates a change in brush height.

Whereas Kapβ1 promotes a substantial extension, NTF2 binding results in a decrease in brush height. This phenomenon has been explored theoretically by Opferman, *et al.* [161, 162], who predict that nanoparticle binding to polymer brushes induces conformational changes that depend largely on the size of the nanoparticle and the interaction energy with the polymer. Then, brush height originates from competition between the binding energy of nanoparticles to the polymer, favoring compaction, and the confinement entropy of the polymers, promoting extension. Kapβ1 has a higher affinity for FG repeats than NTF2, and its binding may favor layer extension because of its relatively large volume, which impacts on the entropy of the FG chains. Conversely, NTF2 binding favors collapse over extension because of its smaller size, although extension may be possible at higher (but non-physiological) concentrations. By contrast, NTF2-W7A did not collapse the brush because it only binds very weakly to Nsp1p. Overall, the obtained data provides strong experimental validation of the mechanism proposed by Opferman, *et al.* (Figure 4.10).

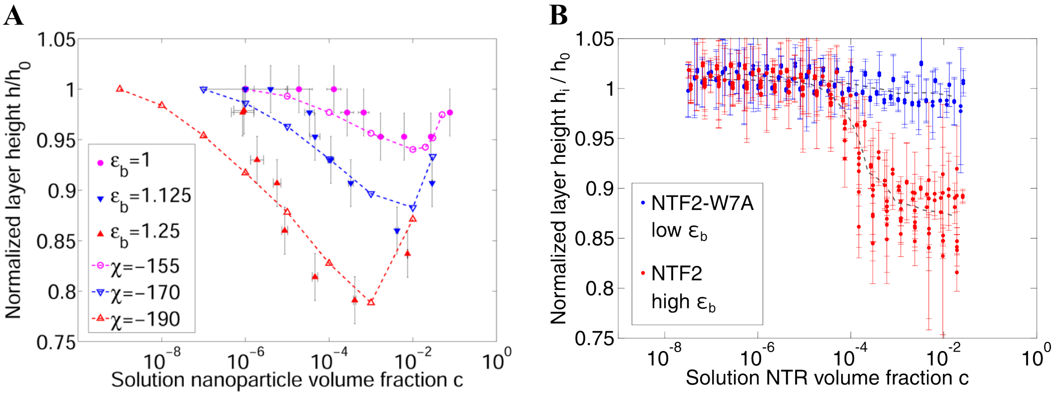

FIGURE 4.10: Experimental data of Nsp1p-12FF layer height change compared with theoretical and simulation data on polymer-nanoparticle interaction obtained by Opferman, *et al.* [161]. **(A)** Simulated polymer layer height, h/h_0, as a function of volume fraction of nanoparticles in solution, c, for different binding strengths. $\chi < 0$ and $\varepsilon_b > 0$ correspond to attractive polymer-nanoparticle interactions in context of theory (unfilled symbols, dashed line) and simulation (filled symbols), respectively. The volume of each nanoparticle is 96 nm^3. Increasing c leads to a decrease in h/h_0 followed by an onset of re-extension. The magnitude of layer collapse correlates with binding strength, i.e, more pronounced collapse is obtained for higher affinity. **(B)** Nsp1p-12FF relative layer height as a function of NTR (i.e., NTF2 or NTF2-W7A) volume fraction in solution. The volume of a single wild-type and mutant NTF2 is assumed to be $d_h^3 = 125$ nm^3, where d_h is the hydrodynamic diameter [9]. For high affinity binding (i.e., wild-type binding; high ε_b) the layer collapses with increasing NTF2 volume fraction, whereas for low affinity NTF2-W7A binding (low ε_b) no significant layer collapse could be measured. This is in good agreement with theory and simulation. **(A)** reproduced from Opferman, *et al.* [161].

4.4.2 Relevance of FG Domain Kapβ1 Occupancy for the NPC

The results obtained here show that more than 2 layers of long-lived Kapβ1 occupy the FG domain brush at physiological concentrations. Indeed, high Kapβ1 occupancy has been observed in cells where ∼100 Kapβ1 molecules populate the NPC at steady state [115, 155]. The obtained binding data shows that a major fraction of Kapβ1 is penetrating the FG domain layer and forms stable, long-lived complexes at steady state. This is reflected in the low KD values (i.e., ∼100 nM) in combination with slow dissociation (i.e., $k_{off} \sim 10^{-5}\ s^{-1}$). Although such strong binding might ensure biochemical selectivity, it cannot account for the rapid ∼6 ms NPC translocation times *in vivo* [154]. This implies that only slow transport would exist if the entire transport channel volume would be filled with close-packed FG domains forming a homogeneous distribution of accessible FG repeats (e.g., meshwork).

More importantly, the results presented here reveal that at physiological concentrations, a low-affinity fraction of Kapβ1 (KD >1 μM) coexists with high-affinity Kapβ1 occupying the layer. Low-affinity species experience hindered penetration into the fully-occupied FG domain layer and thus are limited to interact with the surface of the layer. The limited access to FG repeats at the surface promotes a fast phase of Kapβ1 at physiological concentration. Indeed, kinetic analysis reveals that over time, only 0.001% of the total Kapβ1-FG domain interactions contribute to the slow-phase.

In a scenario of NPCs pre-occupied with Kapβ1, newly entering Kapβ1 molecules only find a few available FG repeats and therefore interact only transiently with the FG domains. This implies that these Kapβ1 molecules would remain in the fast phase. A similar situation can be expected if non-specific proteins from cell lysate are able to bind and occupy the FG domains [152]. In accordance with theory [163], the results show that optimal Kap-FG domain interaction strength can be tuned by saturating the FG domains with Kapβ1. With their fast off rates (k_{off}

$\sim$1 s^{-1}) and short half-lives (<100 ms), these species would dominate fast transport through the NPC at physiological Kap concentrations. Nevertheless, this would require an unobstructed path to support transport by the fast phase, such as a single central channel that would be surrounded by the peripheries of Kap-occupied FG domain layers, as recently shown by single-molecule fluorescence detection [109, 164].

4.4.3 Kapβ1 as an Integral Component of the NPC Barrier

FG-centric barrier models (e.g., brush, meshwork) explain the NPC function based on FG domains alone. However, the findings presented here demonstrate that at physiological concentrations, a high affinity fraction of bound Kapβ1 molecules exhibits long-lived interactions with close-packed FG domains and thus, likely form an essential component of the NPC barrier. This represents a shift in paradigm with respect to FG-centric barrier models because it highlights the role of interacting FG domains and Kaps rather than FG domains alone. Here, FG domains appear to act as a flexible velcro-like scaffold with its conformation modulated by Kap occupancy, as illustrated by attractive nanoparticles that penetrate the molecular brush and provoke a morphological response [161, 162]. In addition, Kap occupancy could play a key role in regulating NPC barrier conformation, transport selectivity, and efficiency.

A Kap-centric model based on the obtained results is depicted in Figure 4.11. It describes the spatiotemporal organization of Kapβ1 within the FG domains in the NPC transport channel. At physiological Kapβ1 concentrations, NPC function is defined by a majority of slow-phase Kapβ1 molecules that exhibit persistent interactions with close-packed FxFG domains that extend into the central channel and towards the NPC periphery. Together, Kaps and engorged FG domains form a flexible inner layer which surrounds a narrow aqueous channel along the NPC axis. This defines the passive size limit while remaining selective towards fast-phase Kapβ1 molecules that bind weakly enough to diffuse along the periphery of the FG domains, e.g., by a reduction of dimensionality [95, 113, 118]. This dynamic and reversible system provides a feedback mechanism that reinstates slow Kap species if local vacancies occur. This guarantees a self-healing mechanism for FG domain conformation [111], and normalizes transport selectivity and speed control. The proposed molecular view agrees with high Kapβ1 density detected along the NPC walls due to FG domain binding and further highlights the interactions that describe NPC transport pathways as "self-regulated viscous channels" [109, 164]. Dependent on Kap-Kap competition, numerous translocation times were observed at high Kap concentrations inside NPCs exposing limited FG repeats, and further, translocation was only efficient at sufficiently high enough concentrations of Kapβ1 [165]. Indeed, the results obtained in this work predict that a continuum of different transport rates can exist depending on local NPC Kap concentrations.

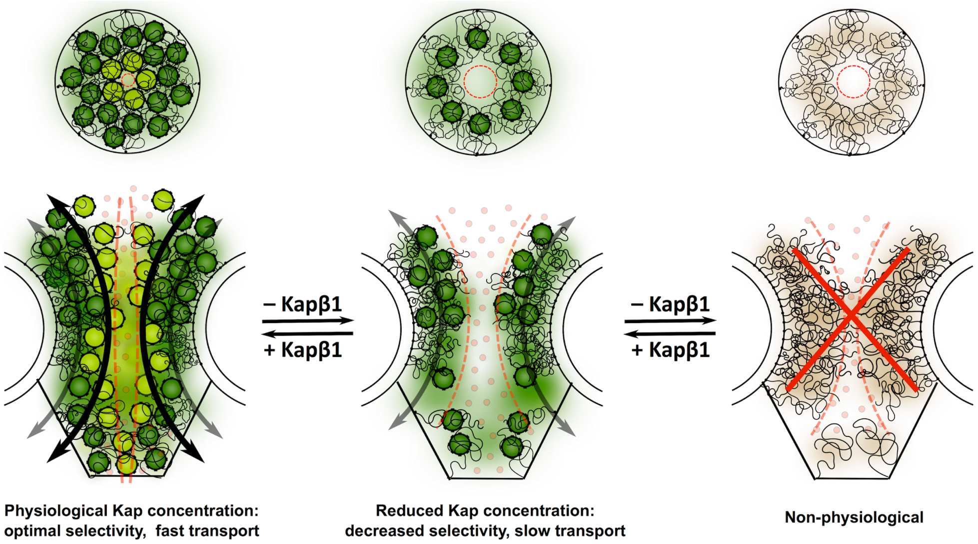

FIGURE 4.11: Kap-centric control in NPCs. Kapβ1 is an integral constituent of the NPC at physiological steady-state conditions. Selective barrier functionality against nonspecific cargoes is provided by slow-phase Kapβ1 molecules (dark green) that saturate and engorge peripheral FG domains. Fast-phase Kapβ1 molecules (light green) promote fast transport through a narrow central channel due to the limited availability of FG repeats. Kapβ1 reduction leads to barrier contraction and a decrease in selectivity because of a widening of the aqueous channel. The availability of free FG repeats slows down the transport of Kapβ1 molecules, which eventually repopulate the FG domains to reinstate normal Kap occupancy and, thereafter, selectivity and speed control. NPCs devoid of Kapβ1 are likely nonphysiological.

Chapter 5

Promiscuous Binding of FG Domains to NTRs

5.1 Introduction

The properties of NTF2 and Kapβ1 binding to pristine FG domain layers separately were investigated in Chapter 4. Based on the obtained results, the main conclusion states that Kapβ1 constitutes an integral constituent of the NPC barrier, a functionality which is often assigned only to the FG domains. Additionally, Kapβ1 was hypothesized to play a key role in regulating both mechanistic and kinetic aspects of NPC barrier functionality. Indeed, up to 100 immobile Kapβ1 molecules were identified per NPC [115, 155]. In contrast, only ∼6 tightly bound NTF2 molecules were found per NPC. Such steady-state NPCs likely harbor a high number of different transport factors (e.g., Kapβ1 and NTF2) which are simultaneously crossing the nuclear envelope [50, 115]. How such promiscuous interactions of many different multivalent NTRs binding FG domains influence each other is not known.

To address this question, NTF2 binding was investigated in the presence of Kapβ1 on close-packed FxFG domains of Nsp1p. Generally, as SPR is sensitive to any change in refractive index, it is not feasible to distinguish between different types of molecules interacting simultaneously with the ligand. This describes an inherent problem of SPR: "the good news is that everything has an SPR signal, and the bad news is that everything has an SPR signal" [166]. Therefore it is a major challenge to decouple the binding response of two analytes binding the same ligand simultaneously. In the case of NTF2 and Kapβ1 binding, this restriction could be overcome using the additional information from the BSA height measurements and the fact that slow-phase Kapβ1 exhibits a $t_{1/2}$ of several hours (see Chapter 4).

5.2 Materials and Methods

5.2.1 Kapβ1-FG Domain Binding in Constant NTF2 Background

SPR sensor functionalization with Nsp1p-12FF was done as described in Chapter 3. Kapβ1 was dialysed against PBS using 3500 MWCO dialysis bags for 3 h at RT while stirring. NTF2 was already stored in PBS, and therefore, was directly used after thawing. Absorbance at 280 nm was measured to determine protein concentration. After dialysis, Kapβ1 was concentrated at 2800 x g (10k, Amicron ultra-4, Merck Millipore, Inc.) to a concentration of ∼ 30 µM. Concentrated Kapβ1 was diluted 1:1 with 40 µM NTF2 in PBS. This mixture was the starting point of a dilution series with 20 µM NTF2 in PBS. Therefore, the resulting series of different Kapβ1 concentrations was in a constant background of 20 µM NTF2. 1% (w/v) BSA was prepared by dissolving lyophilized BSA in 20 µM NTF2 in PBS. To have a constant NTF2 background, ∼300 ml running buffer of 20 µM NTF2 in PBS was prepared by diluting concentrated NTF2 with previously filtered and degased PBS. Simultaneously, Kapβ1 and BSA were prepared using only PBS as described in Chapter 4. Subsequent binding of Kapβ1 on Nsp1p-12FF with and without NTF2 in the background and the resulting FG domain layer height changes were measured using BSA injections as described in Chapter 2 and 4.

5.2.2 Decoupling NTF2 and Kapβ1 SPR response

In this experiment, the proteins (i.e., NTF2, Kapβ1, Nsp1p-12FF and BSA) and PBS as running buffer were prepared as described in Chapter 4. The SPRs microfluidic system is restricted to three modes of flow-cell (FC) addressing: i) injection in a single FC (i.e., 1,2,3 or 4), ii) simultaneous injections in all four FCs 1 – 4, and iii) simultaneous injection in FCs 1 and 2, and FCs 3 and 4. Here, FG domains were sequentially immobilized in FCs 2 and 4 at high concentrations to achieve close-packing (i.e., Nsp1p-12FF forms a molecular brush). The gold surface in FCs 1 and 3 was passivated using PUT (Figure 5.1A).

After sensor surface preparation and functionalization, the experiment consisted of two main cycles.

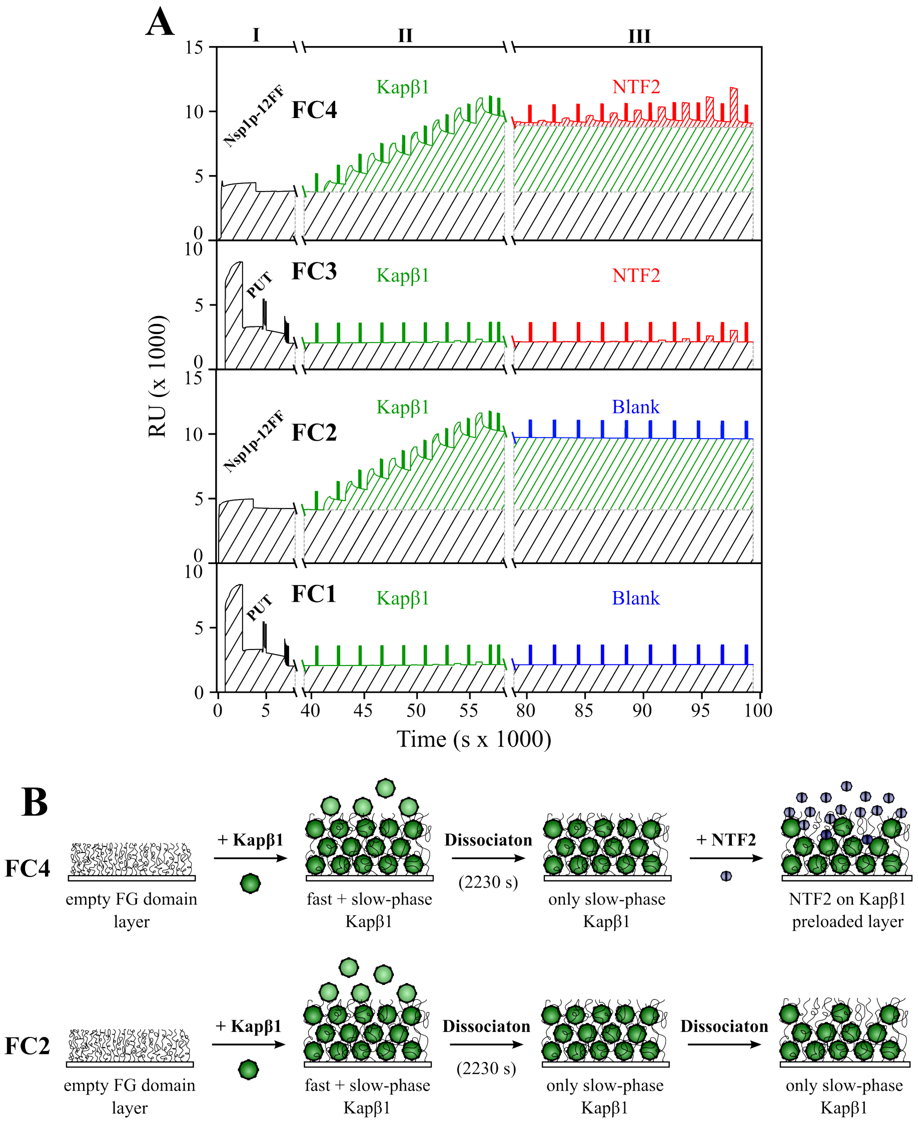

FIGURE 5.1: SPR procedure of promiscuous binding experiments. **(A)** FG domains were sequentially immobilized in FCs 2 and 4, whereas FCs 1 and 3 underwent PUT passivation (I). Kapβ1 was injected in all four FCs with increasing concentrations up to ~15 μM (II). BSA injections in all flow-cells following Kapβ1 injections was used to measure the layer height. After the last injection of Kapβ1, a dissociation phase of 2230 s was applied to remove all weakly bound (i.e., fast-phase) Kapβ1. NTF2 was injected with increasing concentration in FCs 3 and 4 up to ~270 μM, while FCs 1 and 2 were washed with PBS (running buffer; blank). The SPR response was continuously monitored in all four FCs. **(B)** Model based on the previous results describing NTR occupancy and layer characteristics during the experimental procedure.

First, Kapβ1 was injected in all four FCs with increasing concentrations up to ∼15 μM. This resulted in Kapβ1-FG domain binding in FCs 2 and 4. BSA injections in all FCs following Kapβ1 injections was used to measure the layer height change of Nsp1p-12FF. After the last injection of Kapβ1 (i.e., the highest concentration of Kapβ1), a dissociation phase of 2230 s was applied to remove all fast-phase (i.e., weakly bound) Kapβ1 (Figure 5.1A).

Second, NTF2 was injected with increasing concentration in FCs 3 and 4, while FCs 1 and 2 were washed with buffer.

The SPR response was continuously monitored in all four FCs (Figure 5.1A). Figure 5.1B shows the procedure of NTF2 binding on Kapβ1 preloaded Nsp1p-12FF layers in FC 4 while only buffer is injected in FC 2. Here, PUT passivated reference FCs 1 and 3 were used to correct for bulk refractive index changes in FCs 2 and 4, respectively. To decouple the signal of NTF2 from Kapβ1, the slow dissociation phase of Kapβ1 (see Figure 5.1A) was fitted using a sum of exponential functions describing the dissociation of $n = 3$ different kinetic species (see Chapter 4) forming binary complexes on the surface, modeled by

$$s(t) = \sum_{n} A_n e^{-k_{d,n} \cdot t} \tag{5.1}$$

where $s(t)$ is the total experimental SPR signal of Kapβ1, t is time, A_n the individual binding response at $t = 0$ of each species and $k_{d,n}$ is the apparent kinetic dissociation rate of species n (Figure 5.2A). BSA injections were not included in the fit by using a mask in the fitting procedure. In a next step, the dissociation of Kapβ1 was fitted while NTF2 was injected with increasing concentration. The fit was applied only until NTF2 injections showed a significant change in the SPR response (Figure 5.2B) and the apparent dissociation rates resulting from the first fit were fixed and only the individual magnitudes A_n were fitted. Finally, the obtained fit for the dissociation of Kapβ1 was subtracted from the total SPR binding signal leaving only the decoupled sensogram for NTF2 binding (Figure 5.2C).

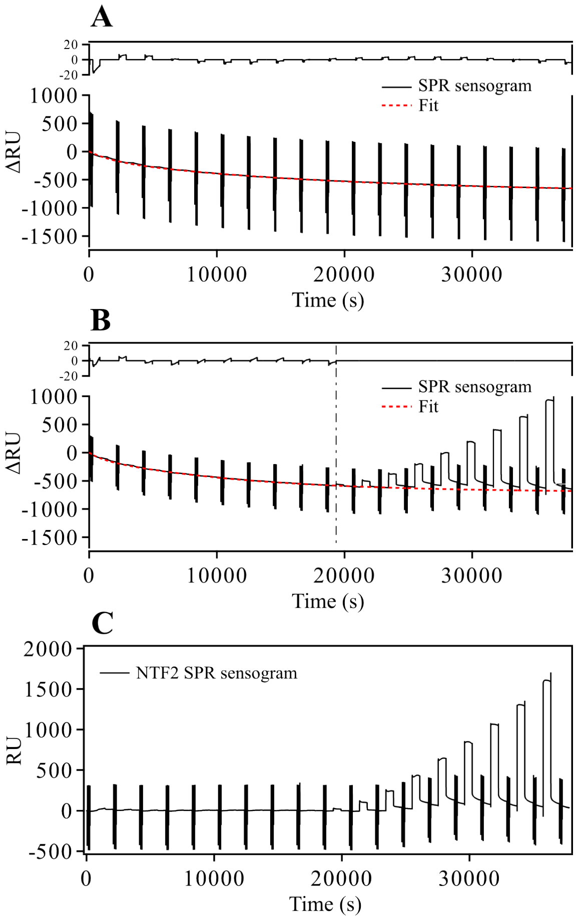

FIGURE 5.2: **(A)** Dissociation of Kapβ1 and fit. **(B)** The dissociation of Kapβ1 was fitted for the first few injections (up to the dashed vertical line) where no significant change in SPR response was measured due to the low concentration of injected NTF2. **(C)** NTF2 binding was isolated by subtracting the fit in **(B)** from the SPR sensogram of **(B)**.

The resulting sensogram was used for further analysis (e.g., equilibrium binding or kinetic analysis) analog to the uncorrected sensograms for NTF2/NTF2-W7A and Kapβ1 binding pristine FG-domain layers. Final injections of 0.2 M NaOH was used on a Kapβ1 filled FG domain layer in order to remove all non-covalently bound material. Indeed, in Figure 5.3 it is shown that this washing step removed all bound Kapβ1 and restored the initial layer height. This indicates that Kapβ1 does not bind the gold surface of the SPR sensor chip and the measured long-lived species are therefore based on non-covalent interactions with FG domains (i.e., no thiol-gold bonds).

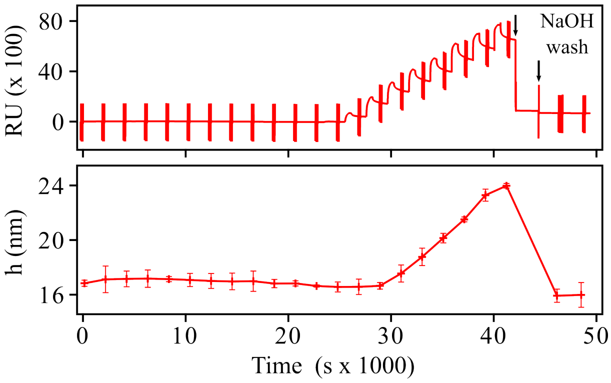

FIGURE 5.3: Bound Kapβ1 in an Nsp1p-12FF layer could be removed by washing twice with short injections (30 s) of 0.2 M NaOH in PBS (pH ~13). This shows that Kapβ1 is not covalently attached to the gold layer. Top: SPR response reaching baseline after regeneration. Bottom: After regeneration, the layer height is restored to its initial value.

5.3 Promiscuous Binding of Close-Packed FG Domains to NTF2 and Kapβ1

5.3.1 Kapβ1-FG Domain Binding in a Physiological Background of NTF2

The layer height change was measured using the BSA method while Kapβ1 was sequentially injected with increasing concentration on Nsp1p-12FF layers. As reported before in Chapter 4, the Nsp1p-12FF layer extends by up to 50% of its initial height as a function of Kapβ1 occupancy. In a second experiment, Kapβ1 was again injected with increasing concentration on a pristine Nsp1p-12FF layer. Although in this case, the Kapβ1 binding was measured in a background of 20 μM NTF2 (i.e., physiological concentration [157]). This experiment was designed to investigate the layer height change upon binding NTF2 and Kapβ1 simultaneously. Figure 5.4 shows the layer height change due to Kapβ1 binding Nsp1p-12FF in absence of NTF2 or in a constant background of 20 μM NTF2. The obtained data indicates that there is no detectable difference in the Kapβ1 dependent layer height change when measured alone or in a constant background of physiological NTF2 concentrations.

Previous experiments on pristine Nsp1p-12FF layers showed that Kapβ1 binding leads to extension, while NTF2 drives layer collapse (see Chapter 4). To this end, Figure 5.4 shows that the effect of NTF2 binding is dominated by Kapβ1 as the layer expands even in the presence of NTF2.This dominance is well reflected by the different affinities of the two proteins.

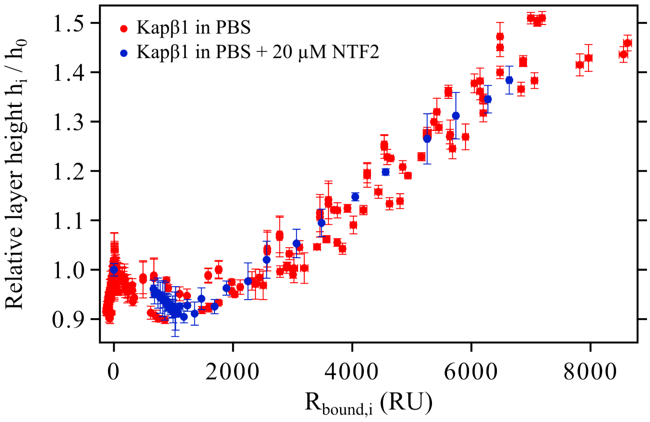

FIGURE 5.4: Kapβ1-FG domain binding in physiological NTF2 background. The Nsp1p-12FF layer expansion upon binding Kapβ1 in an NTF2 background of 20 μM does not significantly differ from binding Kapβ1 in buffer only. It seems likely that the effect of NTF2 induced layer collapse is dominated by Kapβ1 extension. Error bars are ±SD.

5.3.2 NTF2 Binding to Kapβ1 preloaded FG Domains

Several different types of Kaps are thought to simultaneously bind the FG Nups within individual NPCs [50]. To examine the effect of high Kapβ1 occupancy on NTF2-FG domain binding, Nsp1p-12FF layers were preloaded with Kapβ1 prior to sequential NTF2 injections combined with measuring the total change of mass on the surface (Figure 5.1A). In general, decoupling of the SPR signal for two different analytes simultaneously interacting with the surface is not feasible. However, I reasoned that decoupling under the current these circumstances could be possible given that the majority of Nsp1p-bound Kapβ1 was far longer-lived (~90% with $k_{off} < 10^{-3}$ s^{-1}; Figure 4.7A) than NTF2 (~30% $k_{off} < 10^{-3}$ s^{-1}; Figure 4.9A). Initially, Kapβ1 was sequentially injected with increasing concentration up to ~15 μM (i.e., physiological) in all four SPR FCs (FCs 1 – 4) where two of the surfaces (FCs 2 and 4) were exposing close-packed Nsp1p-12FF and two reference cells underwent PUT passivation (FCs 1 and 3). A subsequent dissociation phase of 2230 s was applied to ensure that all fast species ($k_{off} > 0.01$ s^{-1}) would be removed. Remarkably, 80% of Kapβ1 ($k_{off} < 0.0001$ s^{-1}) exhibited long-lived binding, which corresponds to about 2.5 layers of slow-phase Kapβ1 remaining in complex with the Nsp1p-12FF. As shown in Chapter 5, this resulted in an extension of the layer of up to 50% of its initial height (Figure 5.5A).

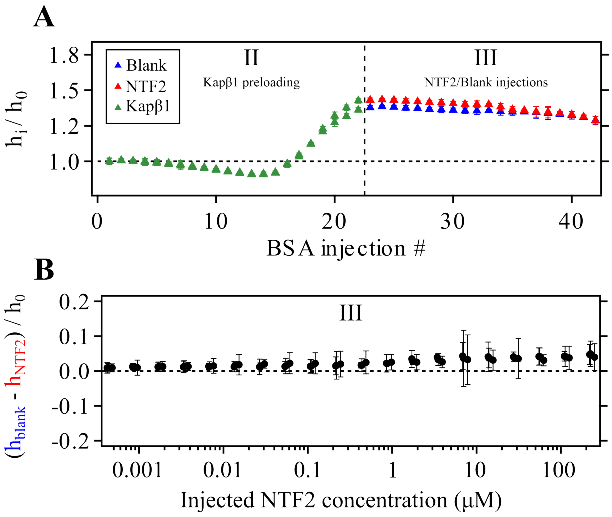

FIGURE 5.5: Layer height change upon NTF2 binding Kapβ1 preloaded Nsp1p-12FF. **(A)** The relative layer height is plotted for every BSA injection after Kapβ1 injections (green) (II), NTF2 (red) or blank (blue) (III) injections, as described in Figure 5.1 and main text. **(B)** The difference in layer height between NTF2 and blank injections on Kapβ1 preloaded Nsp1p-12FF layer (normalized by the initial layer height h_0) is shown as a function of NTF2 concentration for three experiments. Error bars are ±SD.

In a third step, NTF2 was sequentially injected into one Kapβ1 preloaded SPR flow-cell (i.e., FC 4) at the same concentrations used for previous experiments (Figure 5.1A) while the change of mass was continuously monitored in all cells. Unexpectedly, no significant differences were detected when comparing between changes in total layer height owing to the intrinsic dissociation of Kapβ1 (FC3, in the absence of NTF2) and in the presence of promiscuous binding to NTF2 (Figure 5.5B; see also Figure 5.4). Assuming that NTF2 binding did facilitate Kapβ1 dissociation (i.e. "washing-out" of bound Kapβ1), one would anticipate a marked reduction in layer height given that NTF2 drives layer collapse (see Figure 4.3). These results therefore show that NTF2 binding does not significantly impact the structural integrity of Nsp1p FG domain layers preloaded with Kapβ1, consistent with there being no significant competition between already bound Kapβ1 and the NTF2 added. This observation allows NTF2 binding to be decoupled from the total SPR signal by subtracting the intrinsic slow-phase dissociation of Kapβ1 from FC3 (Figure 5.2). The ensuing multivalent binding of NTF2 was subsequently analyzed from the resulting sensogram in the same manner as described for the binding to a pristine Nsp1p layer in Chapter 4. Equilibrium binding analysis revealed a shift in affinity of NTF2 towards weaker binding to Nsp1p-12FF layers. As seen for NTF2 binding pristine FG domain layers, the equilibrium binding response could only be fitted satisfyingly using a two-component Langmuir isotherm (Figure 5.6). With a KD1 = 4.68 ± 0.55 μM, the strong binding population of NTF2 binding Kapβ1 preloaded Nsp1p-12FF layers has a more than two times weaker affinity than that of NTF2 binding empty layers with a KD1 = 2.1 ± 0.5 μM (Figure 4.4B). A similar trend could be observed for NTF2 binding to sparse Nsp1p-12FF and NTF-W7A binding close-packed Nsp1p-12FF. This trends of decreasing avidity can be correlated with the multivalent nature of the interaction which is either reduced by mutation of a major binding site (i.e., NTF2-W7A) or by the number of available free binding sites on the surface (i.e., high Kapβ1 occupancy or "mushroom" conformation).

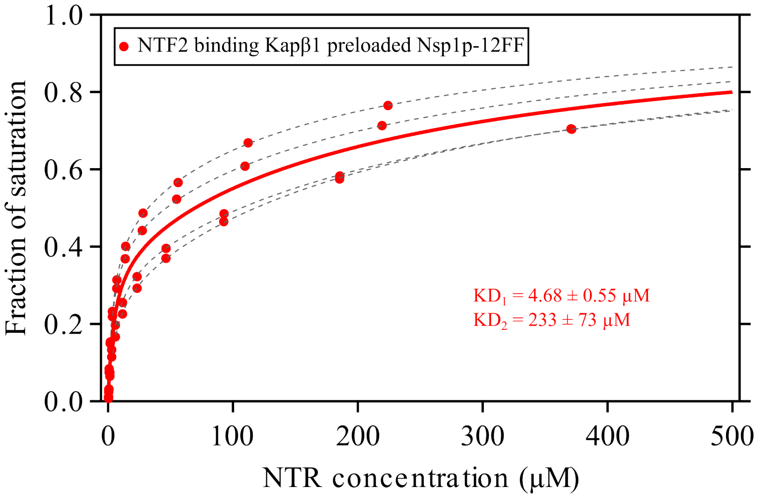

FIGURE 5.6: Equilibrium binding analysis of NTF2 binding Kapβ1 preloaded Nsp1p-12FF layers. The SPR equilibrium response as a function of injected bulk concentration was normalized by the maximum binding capacity (fraction of saturation). Grey dashed lines are individual two-component Langmuir isotherm fits. The isotherm recalculated from the average KD_1 and KD_2 is shown as solid line.

Global analysis of NTF2 binding to promiscuous Nsp1p-12FF layers in the presence of Kapβ1 (Figure 5.7A) indicates that its kinetic properties are significantly different compared to NTF2 binding pristine Nsp1p FG-domain layers alone. When Kapβ1 is absent, NTF2 binding exhibits a high-affinity slow-phase species with low k_{off} and $KD_1 < 1$ μM. In marked contrast, the presence of preloaded Kapβ1 in Nsp1p FG-domain layers shifts NTF2 binding towards weaker binding that is dominated by species with high k_{off} (Figure 5.7A). This result indicates that there is an overall trend towards faster and more transient interactions of NTF2 when Kapβ1 is present in the Nsp1p FG-domain layer (Figure 5.7B).

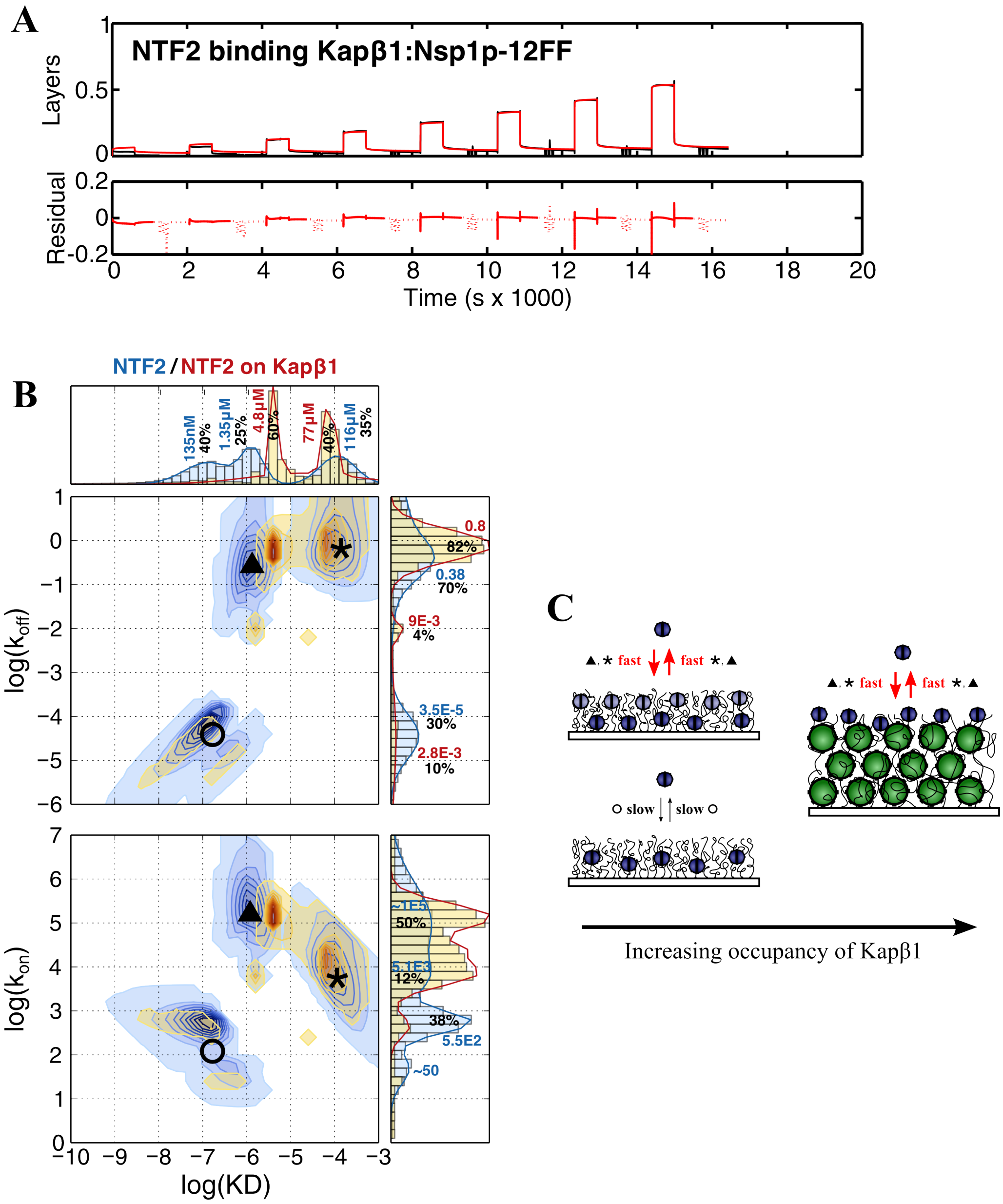

FIGURE 5.7: Kinetic analysis of NTF2 binding Kapβ1 preloaded Nsp1p-12FF and mechanistic model. **(A)** Representative fits (red) to SPR sensograms (black) for NTF2 binding to Kapβ1-preloaded Nsp1p-12FF. NTR binding is converted into respective number of layers, n. The residuals of the fits are included below the curves. **(B)** Two-dimensional interaction maps of kinetic on- and off-rates (k_{on}, k_{off}) for NTF2 (blue) and NTF2 on Kapβ1-preloaded FG domain layer (red) are shown with their derived equilibrium binding constant, KD. The fractional abundance of different kinetic states is indicated by the color intensity and the sum over all values in a given axis is shown as accompanying histograms (top and right panels). The fraction of each distribution in the histograms are given in percent of the total sum and their main values are depicted in bold. Values for k_{off} are s^{-1} and for k_{on} $M^{-1}s^{-1}$, respectively. Different kinetic species are labeled with ○ ("high-avidity slow-phase"), ▲ ("mid-avidity fast- phase") and ∗ ("low-avidity fast-phase"). **(C)** State diagrams separating slow (dark; low k_{off}) and fast (light; high k_{off}) kinetic phases of NTF2 binding. At physiological Kapβ1 concentrations and resulting layer occupancy, NTF2 interactions are shifted towards more transient, fast-phase interactions.

5.4 Discussion

Preloading Nsp1p brushes with Kapβ1 had a dramatic influence on the binding of NTF2. Binding Kapβ1 to Nsp1p will reduce its flexibility (so Nsp1p becomes increasingly rigid [36, 150]) and also reduce the availability of free FG repeats. Consequently, the avidity of NTF2 will be weakened by the extent to which Kapβ1 is bound. Because Kapβ1 binds more strongly to Nsp1p than NTF2, its occupancy is higher, forcing the layer to extend and resulting in NTF2 molecules finding it harder to penetrate the Kapβ1-dominated volume (Figure 5.7C). Under these conditions, kinetic analysis indicates that the two stronger, specific, interaction modes identified with NTF2 alone are altered in a similar way as observed with the W7A mutant. The strongest mode is essentially eliminated, whereas the affinity of the weaker mode is reduced and the weakest, probably non-specific, binding was not altered greatly. The reduced Nsp1p chain flexibility may increase the entropic cost of binding two Nsp1p chains to a single NTF2 dimer and so inhibit formation of the strongest binding mode. Similarly, the entropic penalty associated with binding a single chain would also increase, resulting in decreased affinity and so an increase in the bound NTF2 population having high off-rates (80%; Figure 5.7B). In terms of mechanics, promiscuous binding to Kapβ1 may be essential to maintain NPC barrier functionality to counterbalance against FG domain collapse caused by NTF2.

The results presented in Chapter 4 suggest that Kapβ1 forms an integral constituent of the NPC barrier, which is often assigned to the FG domains alone, and that Kapβ1 contributes to modulating both mechanistic and kinetic aspects of NPC barrier functionality. Here, the stronger and longer-lived FG domain-binding interactions exhibited by Kapβ1 compared to those of NTF2 provides further support for such a Kap-centric barrier mechanism [111]. Promiscuous binding to Kapβ1 may be essential to maintain NPC barrier function by increasing the rigidity of the FG domain layer [36, 150] and to strengthen the barrier against molecules that bind non-specifically [118, 152]. As illustrated in Figure 5.8, the presence of slow-phase Kapβ1 would hinder and limit how far NTF2 penetrates into the FG layer thereby counterbalancing NTF2-mediated FG domain collapse. Consequently, decreasing the effective concentration or occupancy of Kapβ1 at the NPC would generate a less effective barrier (i.e., more open, less selective) due to the conformational response of the FG chains [111] facilitated by NTF2-binding inducing brush collapse. In terms of transport kinetics, the presence of pre-bound Kapβ1 molecules implies that facilitated diffusion of NTF2 would proceed along the peripheral regions of the engorged FG domains due to faster interaction kinetics (high k_{off}) with the reduced number of FG repeats i.e., such as by reduction of dimensionality [113, 118]. Overlapping with the NPC size-exclusion limit of ∼5 nm [6], the hydrodynamic diameter of ∼5 nm [9] potentially allows NTF2 dimers to diffuse across the barrier without binding FG repeats. Although this is possible, kinetic measurements performed in *Xenopus laevis* show that NTF2 traverses about 50 times more efficient than a similar sized GFP molecule (29 kDa), indicating the importance of NTF2-FG repeat interactions [12, 167].

In the cell, the rate at which RanGDP is returned to the nucleus must match the rate of Kap-based nucleocytoplasmic transport because each transport cycle consumes RanGTP. If NTF2 translocation rates were slower than karyopherin transport, there would eventually be insufficient nuclear RanGTP to maintain the transport pathways. The Kap-centric model predicts the rapid NTF2-mediated Ran import needed to maintain the Ran cycle is promoted by binding promiscuity in the NPCs. Indeed, studies show that the immobile fraction of Kapβ1 (∼100 molecules/pore) is substantially larger than that of NTF2 (∼6 molecules/pore) [115]. This argues for a relatively unobstructed central channel surrounded by Kapβ1-filled FG domains through which NTF2 would traverse in a manner spatially and temporally contiguous with the fast Kapβ1 phase, consistent with single molecule fluorescence localization data for Kapβ1 and NTF2 [109]. Consistent with the Kap-centric hypothesis, *in vitro* nuclear protein import assays show increased transport rates with increasing Kapβ1 concentrations [165], albeit precisely how Kapβ1 influences the promiscuous binding of FG domains to other Kaps or transport factors *in vivo* remains unexplored.

As the main nucleocytoplasmic transport hub, a formidable challenge lies in decoupling the synchrony of diverse signaling pathways that converge on the NPCs [50]. Clearly the pore channel is crowded [115], and knowing the effective local concentrations of each transport factor in and around the NPC is essential [168], but it is crucial to establish whether different transport factors bind preferentially to the FG Nups. In terms of binding promiscuity, this would essentially demarcate not only spatial pathways [169], but also temporal ones. Regardless, promiscuous binding and the likely influence of Kapβ1 binding on the off-rate of other transport factors make important contributions that need to be included when formulating precise biophysical models of nucleocytoplasmic transport.

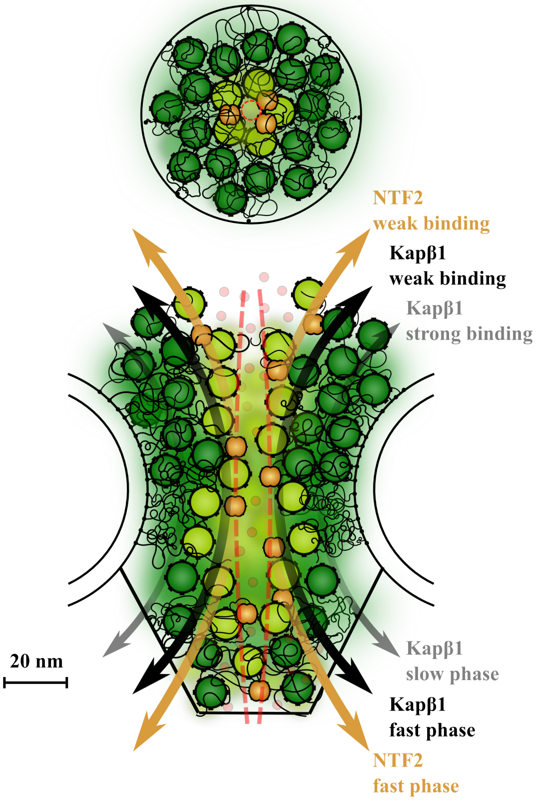

FIGURE 5.8: Kap-centric barrier model showing how different transport factors may share contiguous spatial and temporal routes through the NPC central channel. Strong binding Kapβ1 molecules (dark green) occupy the FG Nups and form integral constituents of the barrier mechanism. This crowding restricts NTF2 (orange) and a smaller fraction of Kapβ1 (light green) to bind a limited number of FG repeats at the FG Nup periphery that promotes facilitated diffusion through a largely unobstructed narrow central channel. This ∼5 nm wide central channel is also used by passively diffusing molecules (light red) that are crossing the pore.

Chapter 6

Conclusion

In this thesis, I studied the interaction of two NTRs, Kapβ1 and NTF2, with surface-grafted Nsp1p FG domains of the yeast NPC. Surface grafted Nsp1p represents a minimal model system to study the FG Nup barrier functionality of the NPC *in vitro*.

In addition to well established SPR experiments, I used a novel technique developed by Schoch, *et al.* [123] that allows measurements of surface-grafted protein layer heights (e.g., molecular brushes) using non-interacting BSA molecules. To account for the NTR-FG domain binding and stimuli-responsive brush behavior, the kinetic analysis was extended to describe multivalency and the surface heterogeneity of the FG domain layer [158]. Finally, I investigated the effect of promiscuous binding of FG domains to Kapβ1 and NTF2 by taking advantage of the long-lived property of Kapβ1.

To conclude my thesis, the obtained results show that

1.) Surface tethering of FG domains is essential in the context of the NPC, as it defines the pore boundary, establishes FG domain orientation, and enforces a limit on Kap occupancy (and how far FG domains can extend). In the close-packed regime, Nsp1p exhibits molecular brush behavior and can incorporate up to three or more layers of Kapβ1 molecules at physiological Kapβ1 concentrations, albeit with varying degrees of extensibility.

2.) Multivalent Kaps may serve as integral, regulatory constituents of the NPC by balancing mechanistic with kinetic control over the NPC barrier mechanism. Here, the role of multivalency is twofold: first, it allows for a slow phase of Kapβ1 to penetrate and drive the extension of FG domains (i.e., the barrier) due to high binding avidity; and second, it promotes a fast transient phase of Kapβ1 that proceeds with reduced avidity along the peripheral regions of the FG domains.

3.) In contrast to Kapβ1, NTF2 binding induced collapse instead of extension, which experimentally validates theory and simulations predicting that binding-induced conformational changes in polymer brushes depend on nanoparticle size and interaction energy [161, 162]. Further, the results suggest a dominating role of Kaps in modulating the barrier mechanism which is reflected in the unaltered layer response when binding Kapβ1 in a physiological background of NTF2.

4.) Promiscuous binding of FG Nups to NTRs ought to influence nucleocytoplasmic transport. This depends on the concentration, size and binding strength of each NTR. Indeed, some form of hierarchy may exist between different NTRs such that their relative concentrations may impact NPC barrier function. Here, NTF2 kinetics was significantly influenced by the presence of Kapβ1 which was indicated by an increase of transiently interacting NTF2.

This interpretation departs from the conventional view that the FG domains alone form the NPC permeability barrier. Rather the results suggest that these domains contribute to a crowding-based barrier function by concentrating transport receptors in the pore. As the main nucleocytoplasmic transport hub, a formidable challenge lies in decoupling the diverse pathways that converge on NPCs [50]. Clearly the pore channel is crowded [115], and knowing the effective local concentrations of each transport receptor in and around the NPC is essential [168]. Irrespective of the precise mechanisms involved, promiscuous binding and the influence of Kapβ1 binding on the off-rate of other NTRs clearly make contributions that need to be included when formulating more precise models of nucleocytoplasmic transport.

Bibliography

[1] M. P. Rout and G. Blobel. 'Isolation of the yeast nuclear pore complex.' In: *The Journal of cell biology* 123.4 (1993), pp. 771–83.

[2] R. Reichelt, A. Holzenburg, E. L. Buhle, M. Jarnik, A. Engel and U. Aebi. 'Correlation between structure and mass distribution of the nuclear pore complex and of distinct pore complex components.' In: *The Journal of cell biology* 110.4 (1990), pp. 883–94.

[3] G. G. Maul and L. Deaven. 'Quantitative determination of nuclear pore complexes in cycling cells with differing DNA content.' In: *The Journal of cell biology* 73.3 (1977), pp. 748–60.

[4] V. C. Cordes, S. Reidenbach and W. W. Franke. 'High content of a nuclear pore complex protein in cytoplasmic annulate lamellae of Xenopus oocytes.' In: *European journal of cell biology* 68.3 (1995), pp. 240–55.

[5] M. Winey, D. Yarar, T. H. Giddings and D. N. Mastronarde. 'Nuclear pore complex number and distribution throughout the Saccharomyces cerevisiae cell cycle by three-dimensional reconstruction from electron micrographs of nuclear envelopes.' In: *Molecular biology of the cell* 8.11 (1997), pp. 2119–32.

[6] P. L. Paine, L. C. Moore and S. B. Horowitz. 'Nuclear envelope permeability'. In: *Nature* 254.5496 (1975), pp. 109–114.

[7] N. Panté and M. Kann. 'Nuclear pore complex is able to transport macromolecules with diameters of about 39 nm.' In: *Molecular biology of the cell* 13.2 (2002), pp. 425–34.

[8] D. Grünwald, R. H. Singer and M. Rout. 'Nuclear export dynamics of RNA-protein complexes.' In: *Nature* 475.7356 (2011), pp. 333–41.

[9] K. Ribbeck and D. Görlich. 'Kinetic analysis of translocation through nuclear pore complexes.' In: *The EMBO journal* 20.6 (2001), pp. 1320–30.

[10] G. Riddick and I. G. Macara. 'A systems analysis of importin-{alpha}-{beta} mediated nuclear protein import.' In: *The Journal of cell biology* 168.7 (2005), pp. 1027–38.

[11] W. Yang, J. Gelles and S. M. Musser. 'Imaging of single-molecule translocation through nuclear pore complexes.' In: *Proceedings of the National Academy of Sciences of the United States of America* 101.35 (2004), pp. 12887–92.

[12] J. P. Siebrasse and R. Peters. 'Rapid translocation of NTF2 through the nuclear pore of isolated nuclei and nuclear envelopes'. In: *EMBO reports* 3.9 (2002), pp. 887–892.

[13] M. P. Rout, J. D. Aitchison, A. Suprapto, K. Hjertaas, Y. Zhao and B. T. Chait. 'The yeast nuclear pore complex: composition, architecture, and transport mechanism'. In: *The Journal of cell biology* 148.4 (2000), pp. 635–651.

[14] J. M. Cronshaw, A. N. Krutchinsky, W. Zhang, B. T. Chait and M. J. Matunis. 'Proteomic analysis of the mammalian nuclear pore complex.' In: *The Journal of cell biology* 158.5 (2002), pp. 915–27.

[15] L. I. Davis and G. Blobel. 'Identification and characterization of a nuclear pore complex protein.' In: *Cell* 45.5 (1986), pp. 699–709.

[16] J. A. DeGrasse, K. N. DuBois, D. Devos, T. N. Siegel, A. Sali, M. C. Field, M. P. Rout and B. T. Chait. 'Evidence for a shared nuclear pore complex architecture that is conserved from the last common eukaryotic ancestor'. In: *Mol Cell Proteomics* 8.9 (2009), pp. 2119–2130.

[17] D. Stoffler, B. Feja, B. Fahrenkrog, J. Walz, D. Typke and U. Aebi. 'Cryo-electron tomography provides novel insights into nuclear pore architecture: implications for nucleocytoplasmic transport'. In: *Journal of molecular biology* 328.1 (2003), pp. 119–130.

[18] T. Maimon, N. Elad, I. Dahan and O. Medalia. 'The Human Nuclear Pore Complex as Revealed by Cryo-Electron Tomography'. In: *Structure* 20.6 (2012), pp. 998–1006.

[19] M. Beck, F. Förster, M. Ecke, J. M. Plitzko, F. Melchior, G. Gerisch, W. Baumeister and O. Medalia. 'Nuclear Pore Complex Structure and Dynamics Revealed by Cryoelectron Tomography'. In: *Science* 306.5700 (2004), pp. 1387–1390.

[20] M. Beck, V. Lucić, F. Förster, W. Baumeister and O. Medalia. 'Snapshots of nuclear pore complexes in action captured by cryo-electron tomography.' In: *Nature* 449.7162 (2007), pp. 611–5.

[21] F. Alber, S. Dokudovskaya, L. M. Veenhoff, W. Zhang, J. Kipper, D. Devos, A. Suprapto, O. Karni-Schmidt, R. Williams, B. T. Chait et al. 'The molecular architecture of the nuclear pore complex'. In: *Nature* 450.7170 (2007), pp. 695–701.

[22] D. Devos, S. Dokudovskaya, R. Williams, F. Alber, N. Eswar, B. T. Chait, M. P. Rout and A. Sali. 'Simple fold composition and modular architecture of the nuclear pore complex.' In: *Proceedings of the National Academy of Sciences of the United States of America* 103.7 (2006), pp. 2172–7.

[23] E. Onischenko, L. H. Stanton, A. S. Madrid, T. Kieselbach and K. Weis. 'Role of the Ndc1 interaction network in yeast nuclear pore complex assembly and maintenance.' In: *The Journal of cell biology* 185.3 (2009), pp. 475–91.

[24] B. Fahrenkrog, E. C. Hurt, U. Aebi and N. Panté. 'Molecular architecture of the yeast nuclear pore complex: localization of Nsp1p subcomplexes.' In: *The Journal of cell biology* 143.3 (1998), pp. 577–88.

[25] D. M. Kraemer, C. Strambio-de-Castillia, G. Blobel and M. P. Rout. 'The essential yeast nucleoporin NUP159 is located on the cytoplasmic side of the nuclear pore complex and serves in karyopherin-mediated binding of transport substrate.' In: *The Journal of biological chemistry* 270.32 (1995), pp. 19017–21.

[26] P. Stelter, R. Kunze, D. Flemming, D. Höpfner, M. Diepholz, P. Philippsen, B. Böttcher and E. Hurt. 'Molecular basis for the functional interaction of dynein light chain with the nuclear-pore complex.' In: *Nature cell biology* 9.7 (2007), pp. 788–96.

[27] T. C. Walther, H. S. Pickersgill, V. C. Cordes, M. W. Goldberg, T. D. Allen, I. W. Mattaj and M. Fornerod. 'The cytoplasmic filaments of the nuclear pore complex are dispensable for selective nuclear protein import.' In: *The Journal of cell biology* 158.1 (2002), pp. 63–77.

[28] H. Zhang, H. Saitoh and M. J. Matunis. 'Enzymes of the SUMO modification pathway localize to filaments of the nuclear pore complex.' In: *Molecular and cellular biology* 22.18 (2002), pp. 6498–508.

[29] K. Ben-Harush, T. Maimon, I. Patla, E. Villa and O. Medalia. 'Visualizing cellular processes at the molecular level by cryo-electron tomography'. In: *Journal of Cell Science* 123.1 (2009), pp. 7–12.

[30] B. Fahrenkrog, B. Maco, A. M. Fager, J. Koser, U. Sauder, K. S. Ullman and U. Aebi. 'Domain-specific antibodies reveal multiple-site topology of Nup153 within the nuclear pore complex'. In: *Journal of structural biology* 140.1-3 (2002), pp. 254–267.

[31] Y. Matsuura, A. Lange, M. T. Harreman, A. H. Corbett and M. Stewart. 'Structural basis for Nup2p function in cargo release and karyopherin recycling in nuclear import.' In: *The EMBO journal* 22.20 (2003), pp. 5358–69.

[32] C. Smythe, H. E. Jenkins and C. J. Hutchison. 'Incorporation of the nuclear pore basket protein nup153 into nuclear pore structures is dependent upon lamina assembly: evidence from cell-free extracts of Xenopus eggs.' In: *The EMBO journal* 19.15 (2000), pp. 3918–31.

[33] N. Sabri, P. Roth, N. Xylourgidis, F. Sadeghifar, J. Adler and C. Samakovlis. 'Distinct functions of the Drosophila Nup153 and Nup214 FG domains in nuclear protein transport.' In: *The Journal of cell biology* 178.4 (2007), pp. 557–65.

[34] D. P. Denning, S. S. Patel, V. Uversky, A. L. Fink and M. Rexach. ‘Disorder in the nuclear pore complex: the FG repeat regions of nucleoporins are natively unfolded’. In: *Proceedings of the National Academy of Sciences of the United States of America* 100.5 (2003), pp. 2450–2455.

[35] R. Y. H. Lim, J. Köser, N.-p. Huang, K. Schwarz-Herion and U. Aebi. ‘Nanomechanical interactions of phenylalanine–glycine nucleoporins studied by single molecule force–volume spectroscopy’. In: *Journal of structural biology* 159.2 (2007), pp. 277–289.

[36] R. Y. H. Lim, B. Fahrenkrog, J. Köser, K. Schwarz-Herion, J. Deng and U. Aebi. ‘Nanomechanical basis of selective gating by the nuclear pore complex.’ In: *Science (New York, N.Y.)* 318.5850 (2007), pp. 640–3.

[37] R. Y. H. Lim, U. Aebi and D. Stoffler. ‘From the trap to the basket: getting to the bottom of the nuclear pore complex.’ In: *Chromosoma* 115.1 (2006), pp. 15–26.

[38] S. S. Patel, B. J. Belmont, J. M. Sante and M. F. Rexach. ‘Natively unfolded nucleoporins gate protein diffusion across the nuclear pore complex’. In: *Cell* 129.1 (2007), pp. 83–96.

[39] E. Grossman, O. Medalia and M. Zwerger. ‘Functional Architecture of the Nuclear Pore Complex’. In: *Annual Review of Biophysics* 41.1 (2012), pp. 557–584.

[40] E. J. Tran, T. a. Bolger and S. R. Wente. ‘SnapShot: nuclear transport.’ In: *Cell* 131.2 (2007), p. 420.

[41] G. Cingolani, C. Petosa, K. Weis and C. W. Müller. ‘Structure of importin-beta bound to the IBB domain of importin-alpha.’ In: *Nature* 399.6733 (1999), pp. 221–9.

[42] R. Bayliss, T. Littlewood and M. Stewart. ‘Structural basis for the interaction between FxFG nucleoporin repeats and importin-beta in nuclear trafficking.’ In: *Cell* 102.1 (2000), pp. 99–108.

[43] M. T. Harreman, P. E. Cohen, M. R. Hodel, G. J. Truscott, A. H. Corbett and A. E. Hodel. ‘Characterization of the auto-inhibitory sequence within the N-terminal domain of importin alpha.’ In: *The Journal of biological chemistry* 278.24 (2003), pp. 21361–9.

[44] B. Kobe. ‘Autoinhibition by an internal nuclear localization signal revealed by the crystal structure of mammalian importin alpha.’ In: *Nature structural biology* 6.4 (1999), pp. 388–97.

[45] U. Kutay, F. R. Bischoff, S. Kostka, R. Kraft and D. Görlich. ‘Export of importin alpha from the nucleus is mediated by a specific nuclear transport factor.’ In: *Cell* 90.6 (1997), pp. 1061–71.

[46] E. Coutavas, M. Ren, J. D. Oppenheim, P. D'Eustachio and M. G. Rush. 'Characterization of proteins that interact with the cell-cycle regulatory protein Ran/TC4.' In: *Nature* 366.6455 (1993), pp. 585–7.

[47] T. Monecke, T. Güttler, P. Neumann, A. Dickmanns, D. Görlich and R. Ficner. 'Crystal structure of the nuclear export receptor CRM1 in complex with Snurportin1 and RanGTP'. In: *Science* 324.5930 (2009), pp. 1087–1091.

[48] K. Ribbeck, U. Kutay, E. Paraskeva and D. Gorlich. 'The translocation of transportin-cargo complexes through nuclear pores is independent of both Ran and energy'. In: *Current biology : CB* 9.1 (1999), pp. 47–50.

[49] D. Görlich, N. Panté, U. Kutay, U. Aebi and F. R. Bischoff. 'Identification of different roles for RanGDP and RanGTP in nuclear protein import.' In: *The EMBO journal* 15.20 (1996), pp. 5584–94.

[50] I. G. Macara. 'Transport into and out of the nucleus.' In: *Microbiology and molecular biology reviews* 65.4 (2001), pp. 570–94.

[51] K. Ribbeck, G. Lipowsky, H. M. Kent, M. Stewart and D. Görlich. 'NTF2 mediates nuclear import of Ran.' In: *The EMBO journal* 17.22 (1998), pp. 6587–98.

[52] C. Klebe, F. R. Bischoff, H. Ponstingl and a. Wittinghofer. 'Interaction of the nuclear GTP-binding protein Ran with its regulatory proteins RCC1 and RanGAP1.' In: *Biochemistry* 34.2 (1995), pp. 639–47.

[53] P. Tompa. 'Intrinsically unstructured proteins'. In: *Trends in Biochemical Sciences* 27.10 (2002), pp. 527–533.

[54] A. Dunker et al. 'Intrinsically disordered protein'. In: *Journal of Molecular Graphics and Modelling* 19.1 (2001), pp. 26–59.

[55] V. N. Uversky and a. K. Dunker. 'Multiparametric analysis of intrinsically disordered proteins: looking at intrinsic disorder through compound eyes.' In: *Analytical chemistry* 84.5 (2012), pp. 2096–104.

[56] Z. Liu and Y. Huang. 'Advantages of proteins being disordered.' In: *Protein science : a publication of the Protein Society* 23.5 (2014), pp. 539–50.

[57] V. N. Uversky and A. K. Dunker. 'Understanding protein non-folding.' In: *Biochimica et biophysica acta* 1804.6 (2010), pp. 1231–64.

[58] Y. Huang and Z. Liu. 'Kinetic advantage of intrinsically disordered proteins in coupled folding-binding process: a critical assessment of the "fly-casting" mechanism.' In: *Journal of molecular biology* 393.5 (2009), pp. 1143–59.

[59] H.-X. Zhou. 'Intrinsic disorder: signaling via highly specific but short-lived association.' In: *Trends in biochemical sciences* 37.2 (2012), pp. 43–8.

[60] R. A. Mariuzza. 'Multiple paths to multispecificity.' In: *Immunity* 24.4 (2006), pp. 359–61.

[61] A. K. Dunker, M. S. Cortese, P. Romero, L. M. Iakoucheva and V. N. Uversky. ‘Flexible nets. The roles of intrinsic disorder in protein interaction networks.’ In: *The FEBS journal* 272.20 (2005), pp. 5129–48.

[62] L. J. Terry and S. R. Wente. ‘Flexible gates: dynamic topologies and functions for FG nucleoporins in nucleocytoplasmic transport.’ In: *Eukaryotic cell* 8.12 (2009), pp. 1814–27.

[63] O. Peleg and R. Y. H. Lim. ‘Converging on the function of intrinsically disordered nucleoporins in the nuclear pore complex.’ In: *Biological chemistry* 391.7 (2010), pp. 719–30.

[64] L. I. Davis and G. R. Fink. ‘The NUP1 gene encodes an essential component of the yeast nuclear pore complex’. In: *Cell* 61.6 (1990), pp. 965–978.

[65] E. C. Hurt. ‘A novel nucleoskeletal-like protein located at the nuclear periphery is required for the life cycle of Saccharomyces cerevisiae.’ In: *The EMBO journal* 7.13 (1988), pp. 4323–34.

[66] S. R. Wente, M. P. Rout and G. Blobel. ‘A new family of yeast nuclear pore complex proteins.’ In: *The Journal of cell biology* 119.4 (1992), pp. 705–23.

[67] J. D. Aitchison and M. P. Rout. ‘The yeast nuclear pore complex and transport through it’. In: *Genetics* 190.3 (2012), pp. 855–883.

[68] R. Bayliss, K. Ribbeck, D. Akin, H. M. Kent, C. M. Feldherr, D. Görlich and M. Stewart. ‘Interaction between NTF2 and xFxFG-containing nucleoporins is required to mediate nuclear import of RanGDP.’ In: *Journal of molecular biology* 293.3 (1999), pp. 579–93.

[69] R. Bayliss, T. Littlewood, L. A. Strawn, S. R. Wente and M. Stewart. ‘GLFG and FxFG nucleoporins bind to overlapping sites on importin-beta.’ In: *The Journal of biological chemistry* 277.52 (2002), pp. 50597–606.

[70] R. Bayliss, S. W. Leung, R. P. Baker, B. B. Quimby, A. H. Corbett and M. Stewart. ‘Structural basis for the interaction between NTF2 and nucleoporin FxFG repeats.’ In: *The EMBO journal* 21.12 (2002), pp. 2843–53.

[71] R. Y. H. Lim, N.-P. Huang, J. Köser, J. Deng, K. H. A. Lau, K. Schwarz-Herion, B. Fahrenkrog and U. Aebi. ‘Flexible phenylalanine-glycine nucleoporins as entropic barriers to nucleocytoplasmic transport.’ In: *Proceedings of the National Academy of Sciences of the United States of America* 103.25 (2006), pp. 9512–7.

[72] L. A. Strawn, T. Shen, N. Shulga, D. S. Goldfarb and S. R. Wente. ‘Minimal nuclear pore complexes define FG repeat domains essential for transport.’ In: *Nature cell biology* 6.3 (2004), pp. 197–206.

[73] N. P. C. Allen. ‘Deciphering Networks of Protein Interactions at the Nuclear Pore Complex’. In: *Molecular & Cellular Proteomics* 1.12 (2002), pp. 930–946.

[74] F. Alber et al. 'Determining the architectures of macromolecular assemblies.' In: *Nature* 450.7170 (2007), pp. 683–94.

[75] Y. M. Chook and K. E. Süel. 'Nuclear import by karyopherin-βs: recognition and inhibition.' In: *Biochimica et biophysica acta* 1813.9 (2011), pp. 1593–606.

[76] E. Conti, C. W. Müller and M. Stewart. 'Karyopherin flexibility in nucleocytoplasmic transport.' In: *Current opinion in structural biology* 16.2 (2006), pp. 237–44.

[77] T. A. Isgro and K. Schulten. 'Binding dynamics of isolated nucleoporin repeat regions to importin-beta.' In: *Structure* 13.12 (2005), pp. 1869–79.

[78] I. Cushman, B. R. Bowman, M. E. Sowa, O. Lichtarge, F. a. Quiocho and M. S. Moore. 'Computational and biochemical identification of a nuclear pore complex binding site on the nuclear transport carrier NTF2.' In: *Journal of molecular biology* 344.2 (2004), pp. 303–10.

[79] T. a. Isgro and K. Schulten. 'Association of nuclear pore FG-repeat domains to NTF2 import and export complexes.' In: *Journal of molecular biology* 366.1 (2007), pp. 330–45.

[80] J. Morrison, J.-C. Yang, M. Stewart and D. Neuhaus. 'Solution NMR study of the interaction between NTF2 and nucleoporin FxFG repeats.' In: *Journal of molecular biology* 333.3 (2003), pp. 587–603.

[81] C. Fasting, C. a. Schalley, M. Weber, O. Seitz, S. Hecht, B. Koksch, J. Dernedde, C. Graf, E.-W. Knapp and R. Haag. 'Multivalency as a chemical organization and action principle.' In: *Angewandte Chemie (International ed. in English)* 51.42 (2012), pp. 10472–98.

[82] M. Mammen, S.-K. Choi and G. M. Whitesides. 'Polyvalent Interactions in Biological Systems: Implications for Design and Use of Multivalent Ligands and Inhibitors'. In: *Angewandte Chemie (International ed. in English)* 37.20 (1998), pp. 2754–2794.

[83] J. Bednenko, G. Cingolani and L. Gerace. 'Importin beta contains a COOH-terminal nucleoporin binding region important for nuclear transport.' In: *The Journal of cell biology* 162.3 (2003), pp. 391–401.

[84] N. C. Chi and S. A. Adam. 'Functional domains in nuclear import factor p97 for binding the nuclear localization sequence receptor and the nuclear pore.' In: *Molecular biology of the cell* 8.6 (1997), pp. 945–56.

[85] S. M. Liu and M. Stewart. 'Structural basis for the high-affinity binding of nucleoporin Nup1p to the Saccharomyces cerevisiae importin-beta homologue, Kap95p.' In: *Journal of molecular biology* 349.3 (2005), pp. 515–25.

[86] I. Ben-Efraim and L. Gerace. 'Gradient of Increasing Affinity of Importin for Nucleoporins along the Pathway of Nuclear Import'. In: *The Journal of Cell Biology* 152.2 (2001), pp. 411–418.

[87] C. Chaillan-Huntington, P. J. Butler, J. a. Huntington, D. Akin, C. Feldherr and M. Stewart. 'NTF2 monomer-dimer equilibrium.' In: *Journal of molecular biology* 314.3 (2001), pp. 465–77.

[88] U. Grundmann, C. Nerlich, T. Rein, F. Lottspeich and H. A. Küpper. 'Isolation of cDNA coding for the placental protein 15 (PP15).' In: *Nucleic acids research* 16.10 (1988), p. 4721.

[89] M. S. Moore and G. Blobel. 'Purification of a Ran-interacting protein that is required for protein import into the nucleus.' In: *Proceedings of the National Academy of Sciences of the United States of America* 91.21 (1994), pp. 10212–6.

[90] B. M. Paschal and L. Gerace. 'Identification of NTF2, a cytosolic factor for nuclear import that interacts with nuclear pore complex protein p62.' In: *The Journal of cell biology* 129.4 (1995), pp. 925–37.

[91] H. M. Kent, W. D. Clarkson, T. L. Bullock and M. Stewart. 'Crystallization and preliminary X-ray diffraction analysis of nuclear transport factor 2.' In: *Journal of structural biology* 116.2 (1996), pp. 326–9.

[92] M. Stewart, H. M. Kent and a. J. McCoy. 'Structural basis for molecular recognition between nuclear transport factor 2 (NTF2) and the GDP-bound form of the Ras-family GTPase Ran.' In: *Journal of molecular biology* 277.3 (1998), pp. 635–46.

[93] T. L. Bullock, W. D. Clarkson, H. M. Kent and M. Stewart. 'The 1.6 angstroms resolution crystal structure of nuclear transport factor 2 (NTF2).' In: *Journal of molecular biology* 260.3 (1996), pp. 422–31.

[94] B. B. Quimby, S. W. Leung, R. Bayliss, M. T. Harreman, G. Thirumala, M. Stewart and a. H. Corbett. 'Functional analysis of the hydrophobic patch on nuclear transport factor 2 involved in interactions with the nuclear pore in vivo.' In: *The Journal of biological chemistry* 276.42 (2001), pp. 38820–9.

[95] R. Peters. 'Translocation through the nuclear pore: Kaps pave the way'. In: *Bioessays* 31.4 (2009), pp. 466–477.

[96] U. Kubitscheck, D. Grünwald, A. Hoekstra, D. Rohleder, T. Kues, J. P. Siebrasse and R. Peters. 'Nuclear transport of single molecules: dwell times at the nuclear pore complex.' In: *The Journal of cell biology* 168.2 (2005), pp. 233–43.

[97] K. Ribbeck and D. Gorlich. 'The permeability barrier of nuclear pore complexes appears to operate via hydrophobic exclusion'. In: *The EMBO journal* 21.11 (2002), pp. 2664–2671.

[98] S. Frey, R. P. Richter and D. Görlich. 'FG-rich repeats of nuclear pore proteins form a three-dimensional meshwork with hydrogel-like properties.' In: *Science* 314.5800 (2006), pp. 815–7.

[99] S. Frey and D. Görlich. ‘FG/FxFG as well as GLFG repeats form a selective permeability barrier with self-healing properties.’ In: *The EMBO journal* 28.17 (2009), pp. 2554–67.

[100] S. Frey and D. Gorlich. ‘A saturated FG-repeat hydrogel can reproduce the permeability properties of nuclear pore complexes’. In: *Cell* 130.3 (2007), pp. 512–523.

[101] S. Milles, K. Huy Bui, C. Koehler, M. Eltsov, M. Beck and E. a. Lemke. ‘Facilitated aggregation of FG nucleoporins under molecular crowding conditions.’ In: *EMBO reports* 14.2 (2013), pp. 178–83.

[102] A. a. Labokha, S. Gradmann, S. Frey, B. B. Hülsmann, H. Urlaub, M. Baldus and D. Görlich. ‘Systematic analysis of barrier-forming FG hydrogels from Xenopus nuclear pore complexes.’ In: *The EMBO journal* 32.2 (2013), pp. 204–18.

[103] S. S. Patel and M. F. Rexach. ‘Discovering novel interactions at the nuclear pore complex using bead halo: a rapid method for detecting molecular interactions of high and low affinity at equilibrium.’ In: *Molecular & cellular proteomics : MCP* 7.1 (2008), pp. 121–31.

[104] P. Li et al. ‘Phase transitions in the assembly of multivalent signalling proteins.’ In: *Nature* 483.7389 (2012), pp. 336–40.

[105] M. Rout. ‘Virtual gating and nuclear transport: the hole picture’. In: *Trends in Cell Biology* 13.12 (2003), pp. 622–628.

[106] J. H. Hoh. ‘Functional protein domains from the thermally driven motion of polypeptide chains: a proposal.’ In: *Proteins* 32.2 (1998), pp. 223–8.

[107] P. de Gennes. ‘Polymers at an interface; a simplified view’. In: *Advances in Colloid and Interface Science* 27.3-4 (1987), pp. 189–209.

[108] K. Chattopadhyay, E. L. Elson and C. Frieden. ‘The kinetics of conformational fluctuations in an unfolded protein measured by fluorescence methods.’ In: *Proceedings of the National Academy of Sciences of the United States of America* 102.7 (2005), pp. 2385–9.

[109] J. Ma, A. Goryaynov, A. Sarma and W. Yang. ‘Self-regulated viscous channel in the nuclear pore complex.’ In: *Proceedings of the National Academy of Sciences of the United States of America* 109.19 (2012), pp. 7326–31.

[110] L. E. Kapinos, R. L. Schoch, R. S. Wagner, K. D. Schleicher and R. Y. H. Lim. ‘Karyopherin-centric control of nuclear pores based on molecular occupancy and kinetic analysis of multivalent binding with FG nucleoporins.’ In: *Biophysical journal* 106.8 (2014), pp. 1751–62.

[111] R. L. Schoch, L. E. Kapinos and R. Y. H. Lim. ‘Nuclear transport receptor binding avidity triggers a self-healing collapse transition in FG-nucleoporin molecular brushes.’ In: *Proceedings of the National Academy of Sciences of the United States of America* 109.42 (2012), pp. 16911–6.

[112] G. Adam and M. Delbruck. ‘Reduction of dimensionality in biological diffusion processes’. In: *Structural chemistry and molecular biology.* Ed. by A. Rich and N. Davidson. 1968, pp. 198–215.

[113] R. Peters. ‘Translocation through the nuclear pore complex: selectivity and speed by reduction-of-dimensionality.’ In: *Traffic* 6.5 (2005), pp. 421–7.

[114] R. Peters. ‘Functionalization of a nanopore: the nuclear pore complex paradigm.’ In: *Biochimica et biophysica acta* 1793.10 (2009), pp. 1533–9.

[115] A. Paradise, M. K. Levin, G. Korza and J. H. Carson. ‘Significant proportions of nuclear transport proteins with reduced intracellular mobilities resolved by fluorescence correlation spectroscopy.’ In: *Journal of molecular biology* 365.1 (2007), pp. 50–65.

[116] O. G. Berg and P. H. von Hippel. ‘Diffusion-controlled macromolecular interactions.’ In: *Annual review of biophysics and biophysical chemistry* 14 (1985), pp. 131–60.

[117] N. Shimamoto. ‘One-dimensional Diffusion of Proteins along DNA: Its Biological and Chemical Significance Revealed by Single-molecule Measurements’. In: *Journal of Biological Chemistry* 274.22 (1999), pp. 15293–15296.

[118] K. D. Schleicher, S. L. Dettmer, L. E. Kapinos, S. Pagliara, U. F. Keyser, S. Jeney and R. Y. H. Lim. ‘Selective transport control on molecular velcro made from intrinsically disordered proteins.’ In: *Nature nanotechnology* 9.7 (2014), pp. 525–30.

[119] J. Yamada et al. ‘A bimodal distribution of two distinct categories of intrinsically disordered structures with separate functions in FG nucleoporins’. In: *Molecular & cellular proteomics : MCP* 9.10 (2010), pp. 2205–2224.

[120] R. Gamini, W. Han, J. E. Stone and K. Schulten. ‘Assembly of nsp1 nucleoporins provides insight into nuclear pore complex gating.’ In: *PLoS computational biology* 10.3 (2014), e1003488.

[121] J. Fiserova, S. a. Richards, S. R. Wente and M. W. Goldberg. ‘Facilitated transport and diffusion take distinct spatial routes through the nuclear pore complex.’ In: *Journal of cell science* 123.Pt 16 (2010), pp. 2773–80.

[122] J. Dogan, S. Gianni and P. Jemth. ‘The binding mechanisms of intrinsically disordered proteins.’ In: *Physical chemistry chemical physics : PCCP* 16.14 (2014), pp. 6323–31.

[123] R. L. Schoch and R. Y. H. Lim. ‘Non-interacting molecules as innate structural probes in surface plasmon resonance.’ In: *Langmuir : the ACS journal of surfaces and colloids* 29.12 (2013), pp. 4068–76.

[124] S. W. Kowalczyk, L. Kapinos, T. R. Blosser, T. Magalhães, P. van Nies, R. Y. H. Lim and C. Dekker. ‘Single-molecule transport across an individual biomimetic nuclear pore complex.’ In: *Nature nanotechnology* 6.7 (2011), pp. 433–8.

[125] W. D. Clarkson, a. H. Corbett, B. M. Paschal, H. M. Kent, a. J. McCoy, L. Gerace, P. a. Silver and M. Stewart. ‘Nuclear protein import is decreased by engineered mutants of nuclear transport factor 2 (NTF2) that do not bind GDP-Ran.’ In: *Journal of molecular biology* 272.5 (1997), pp. 716–30.

[126] M. Stewart, H. M. Kent and a. J. McCoy. ‘The structure of the Q69L mutant of GDP-Ran shows a major conformational change in the switch II loop that accounts for its failure to bind nuclear transport factor 2 (NTF2).’ In: *Journal of molecular biology* 284.5 (1998), pp. 1517–27.

[127] W. D. Clarkson, H. M. Kent and M. Stewart. ‘Separate binding sites on nuclear transport factor 2 (NTF2) for GDP-Ran and the phenylalanine-rich repeat regions of nucleoporins p62 and Nsp1p.’ In: *Journal of molecular biology* 263.4 (1996), pp. 517–24.

[128] R. Wood. ‘XLII. On a remarkable case of uneven distribution of light in a diffraction grating spectrum’. In: *Philosophical Magazine Series 6* 4.21 (1902), pp. 396–402.

[129] T. Turbadar. ‘Complete Absorption of Light by Thin Metal Films’. In: *Proceedings of the Physical Society* 73.1 (1959), pp. 40–44.

[130] A. Otto. ‘Excitation of nonradiative surface plasma waves in silver by the method of frustrated total reflection’. In: *Zeitschrift für Physik* 216.4 (1968), pp. 398–410.

[131] E. Kretschmann and H. Raether. ‘Radiative decay of non-radiative surface plasmons excited by light’. In: *Z. Naturforsch.* 23 (1968), pp. 2135–2136.

[132] S. Zeng, D. Baillargeat, H.-P. Ho and K.-T. Yong. ‘Nanomaterials enhanced surface plasmon resonance for biological and chemical sensing applications.’ In: *Chemical Society reviews* 43.10 (2014), pp. 3426–52.

[133] P. B. Johnson and R. W. Christy. ‘Optical Constants of the Noble Metals’. In: *Physical Review B* 6.12 (1972), pp. 4370–4379.

[134] A. Yariv and P. Yeh. *Photonics: optical electronics in modern communications.* Oxford University Press, 2007, p. 849.

[135] S. A. Maier. *Plasmonics: Fundamentals and Applications.* Boston, MA: Springer US, 2007, pp. 1–223.

[136] W. L. Barnes, A. Dereux and T. W. Ebbesen. ‘Surface plasmon subwavelength optics.’ In: *Nature* 424.6950 (2003), pp. 824–30.

[137] J. Homola and M. Piliarik. ‘Surface plasmon resonance (SPR) sensors’. In: *Surface plasmon resonance based sensors* (2006), pp. 3–44.

[138] S. Löfås, M. Malmqvist, I. Rönnberg, E. Stenberg, B. Liedberg and I. Lundström. ‘Bioanalysis with surface plasmon resonance’. In: *Sensors and Actuators B: Chemical* 5.1-4 (1991), pp. 79–84.

[139] E. Stenberg, B. Persson, H. Roos and C. Urbaniczky. 'Quantitative determination of surface concentration of protein with surface plasmon resonance using radiolabeled proteins'. In: *Journal of Colloid and Interface Science* 143.2 (1991), pp. 513–526.

[140] P. Waage and C. M. Gulberg. 'Studies concerning affinity'. In: *Journal of Chemical Education* 63.12 (1986), p. 1044.

[141] J. Svitel, A. Balbo, R. a. Mariuzza, N. R. Gonzales and P. Schuck. 'Combined affinity and rate constant distributions of ligand populations from experimental surface binding kinetics and equilibria.' In: *Biophysical journal* 84.6 (2003), pp. 4062–77.

[142] P. C. Hansen. 'Regularization Tools version 4.0 for Matlab 7.3'. In: *Numerical Algorithms* 46.2 (2007), pp. 189–194.

[143] G. Landi and F. Zama. 'The active-set method for nonnegative regularization of linear ill-posed problems'. In: *Applied Mathematics and Computation* 175.1 (2006), pp. 715–729.

[144] D. G. Myszka, X. He, M. Dembo, T. A. Morton and B. Goldstein. 'Extending the range of rate constants available from BIACORE: interpreting mass transport-influenced binding data.' In: *Biophysical journal* 75.2 (1998), pp. 583–94.

[145] L. L. Christensen. 'Theoretical analysis of protein concentration determination using biosensor technology under conditions of partial mass transport limitation.' In: *Analytical biochemistry* 249.2 (1997), pp. 153–64.

[146] C. Pale-Grosdemange, E. S. Simon, K. L. Prime and G. M. Whitesides. 'Formation of self-assembled monolayers by chemisorption of derivatives of oligo(ethylene glycol) of structure HS(CH2)11(OCH2CH2)mOH on gold'. In: *Journal of the American Chemical Society* 113.1 (1991), pp. 12–20.

[147] H. Häkkinen. 'The gold-sulfur interface at the nanoscale.' In: *Nature chemistry* 4.6 (2012), pp. 443–55.

[148] J. N. Bright, T. B. Woolf and J. H. Hoh. 'Predicting properties of intrinsically unstructured proteins.' In: *Progress in biophysics and molecular biology* 76.3 (2001), pp. 131–73.

[149] L. Miao and K. Schulten. 'Transport-related structures and processes of the nuclear pore complex studied through molecular dynamics'. In: *Structure* 17.3 (2009), pp. 449–459.

[150] N. B. Eisele, S. Frey, J. Piehler, D. Görlich and R. P. Richter. 'Ultrathin nucleoporin phenylalanine-glycine repeat films and their interaction with nuclear transport receptors.' In: *EMBO reports* 11.5 (2010), pp. 366–72.

[151] C. E. Atkinson, A. L. Mattheyses, M. Kampmann and S. M. Simon. 'Conserved spatial organization of FG domains in the nuclear pore complex.' In: *Biophysical journal* 104.1 (2013), pp. 37–50.

[152] J. Tetenbaum-Novatt, L. E. Hough, R. Mironska, A. S. McKenney and M. P. Rout. ‘Nucleocytoplasmic transport: a role for nonspecific competition in karyopherin-nucleoporin interactions.’ In: *Molecular & cellular proteomics : MCP* 11.5 (2012), pp. 31–46.

[153] K. Lott, A. Bhardwaj, G. Mitrousis, N. Pante and G. Cingolani. ‘The importin beta binding domain modulates the avidity of importin beta for the nuclear pore complex’. In: *The Journal of biological chemistry* 285.18 (2010), pp. 13769–13780.

[154] T. Dange, D. Grünwald, A. Grünwald, R. Peters and U. Kubitscheck. ‘Autonomy and robustness of translocation through the nuclear pore complex: a single-molecule study.’ In: *The Journal of cell biology* 183.1 (2008), pp. 77–86.

[155] M. Tokunaga, N. Imamoto and K. Sakata-Sogawa. ‘Highly inclined thin illumination enables clear single-molecule imaging in cells.’ In: *Nature methods* 5.2 (2008), pp. 159–61.

[156] V. N. Uversky. ‘Intrinsically disordered proteins may escape unwanted interactions via functional misfolding.’ In: *Biochimica et biophysica acta* 1814.5 (2011), pp. 693–712.

[157] C. Chaillan-Huntington. ‘Dissecting the Interactions between NTF2, RanGDP, and the Nucleoporin XFXFG Repeats’. In: *Journal of Biological Chemistry* 275.8 (2000), pp. 5874–5879.

[158] J. Svitel, H. Boukari, D. Van Ryk, R. C. Willson and P. Schuck. ‘Probing the functional heterogeneity of surface binding sites by analysis of experimental binding traces and the effect of mass transport limitation.’ In: *Biophysical journal* 92.5 (2007), pp. 1742–58.

[159] E. M. Munoz, J. Correa, R. Riguera and E. Fernandez-Megia. ‘Real-time evaluation of binding mechanisms in multivalent interactions: a surface plasmon resonance kinetic approach.’ In: *Journal of the American Chemical Society* 135.16 (2013), pp. 5966–9.

[160] L.-c. Tu, G. Fu, A. Zilman and S. M. Musser. ‘Large cargo transport by nuclear pores: implications for the spatial organization of FG-nucleoporins.’ In: *The EMBO journal* 32.24 (2013), pp. 3220–30.

[161] M. G. Opferman, R. D. Coalson, D. Jasnow and A. Zilman. ‘Morphology of polymer brushes infiltrated by attractive nanoinclusions of various sizes.’ In: *Langmuir : the ACS journal of surfaces and colloids* 29.27 (2013), pp. 8584–91.

[162] M. G. Opferman, R. D. Coalson, D. Jasnow and A. Zilman. ‘Morphological control of grafted polymer films via attraction to small nanoparticle inclusions’. In: *Physical Review E* 86.3 (2012), p. 031806.

[163] A. Zilman, S. Di Talia, B. T. Chait, M. P. Rout and M. O. Magnasco. 'Efficiency, selectivity, and robustness of nucleocytoplasmic transport'. In: *PLoS Comput Biol* 3.7 (2007), e125.

[164] J. Ma and W. Yang. 'Three-dimensional distribution of transient interactions in the nuclear pore complex obtained from single-molecule snapshots.' In: *Proceedings of the National Academy of Sciences of the United States of America* 107.16 (2010), pp. 7305–10.

[165] W. Yang and S. M. Musser. 'Nuclear import time and transport efficiency depend on importin beta concentration.' In: *The Journal of cell biology* 174.7 (2006), pp. 951–61.

[166] R. Mukhopadhyay. 'Surface plasmon resonance instruments diversify'. In: *Analytical Chemistry* 77.15 (2005), pages.

[167] N. I. Kiskin, J. P. Siebrasse and R. Peters. 'Optical microwell assay of membrane transport kinetics.' In: *Biophysical journal* 85.4 (2003), pp. 2311–22.

[168] G. Schreiber and A. E. Keating. 'Protein binding specificity versus promiscuity.' In: *Current opinion in structural biology* 21.1 (2011), pp. 50–61.

[169] L. J. Terry and S. R. Wente. 'Nuclear mRNA export requires specific FG nucleoporins for translocation through the nuclear pore complex.' In: *The Journal of cell biology* 178.7 (2007), pp. 1121–32.

Acknowledgements

First and foremost I want to thank my PhD supervisor Prof. Roderick Lim for giving me the opportunity to work in his lab. I really enjoyed the freedom I was given that allowed me to explore science on my own. I want to thank for his motivation, guidance and the scientific input on my work. I am especially grateful for his help and empathy during the first three months in the early life of my son.
I also want to thank Prof. Birthe Fahrenkrog for supporting my beginnings on the work with Xenopus laevis oocytes and for being on my committee.
For material and intellectual support of my work I want to thank Prof. Murray Stewart and Neil Marshall. Without their contributions, my work would not have been possible in its present form.
A big "thank you" go to my office mates during this years: Teba, Larisa, Unai, Janne, Kai, Marko, Marija, Lajko, Rafael and Philipp. I always had (and hopefully continue to have) a lot of fun with you all. Especially I want to thank Kai and Lajko for critically reading parts of my manuscript, Janne for his support in AFM, IgorPro and TIRF related matters. Thanks go to Marko and Marija for their scientific inputs and lively discussions, and not to forget, their culinary treats in solid and liquid form.
Acknowledgements go to Timothy Sharpe for his excellent experimental support and for introducing me into DLS, ITC, AUC and CD techniques. My gratitude goes to Larisa Kapinos and Rafael Schoch for their theoretical and experimental contributions to the SPR part of my work. Many thanks go to Chantal Rencurel for the expression and purification of tons of proteins for my project.

List of Publications

- R.S. Wagner, L.E. Kapinos, N.J. Marshall, M. Stewart, and R.Y.H. Lim. 2014. “Promiscuous Binding of Karyopherinβ1 Modulates FG Nucleoporin Barrier Function and Expedites NTF2 Transport Kinetics.”
  Biophysical Journal. 108: 918-27.
- Kapinos, L.E., R.L. Schoch, R.S. Wagner, K.D. Schleicher, and R.Y.H. Lim. 2014. “Karyopherin-centric control of nuclear pores based on molecular occupancy and kinetic analysis of multivalent binding with FG nucleoporins.”
  Biophysical Journal. 106: 1751–62.
- Marot, L., G. De Temmerman, R.P. Doerner, K. Umstadter, R.S. Wagner, D. Mathys, M. Duggelin, and E. Meyer. 2013. “Synergistic effects of hydrogen plasma exposure, pulsed laser heating and temperature on rhodium surfaces.”
  Journal of Nuclear Materials. 432: 388–94